A THERMO-MECHANICAL FORCE MODEL FOR MACHINING HARDENED STEEL

By:

CHARLES EDWARD BECZE, B. ENG., M. ENG.

A Thesis

Submitted to the School of Graduate Studies

in Partial Fulfilment of the Requirements

for the Degree of

Doctor of Philosophy

McMaster University

A THERMO-MECHANICAL FORCE MODEL FOR MACHINING HARDENED STEEL

DOCTOR OF PHILOSOPHY (2002)
(Mechanical Engineering)

McMaster University
Hamilton, Ontario

TITLE: A Thermo-Mechanical Force Model For Machining Hardened Steel

AUTHOR: Charles Edward Becze, B.Eng., M.Eng.

SUPERVISOR: Professor M. A. Elbestawi

NUMBER OF PAGES: xxii, 236

Abstract

The machining of hardened steels is becoming a viable technology. At the inception of the present research, this technology for milling processes was in its infancy. Advancements in cutting tool materials such as poly-crystalline cubic boron nitride (PCBN) have enhanced the ability to machine these difficult to cut alloys. The machining of hardened tool steels have been explored in the recent literature to a great extent because of the possible gains and benefits this technology has to offer. Near net shape manufacturing can become a viable technology and save the die and mold industry considerable investment by reducing the lead time for production of dies and molds.

In this thesis, an experimental investigation is presented regarding the optimal process parameters that make high speed hard machining a viable technology. The experimental investigation shows that hard machining of AISI H13 (55 HRc) is possible, and is an extremely effective technology if the proper conditions are used. Because of the nature of hard machining, the fundamental aspects of chip formation, tool wear and life is explored through a detailed investigation. It was confirmed that the ball milling of hard materials produce segmented saw toothed chips even at low chip loads for specific cutting conditions. It was noticed that the chip morphology was very repeatable and consistent and therefore formed a preliminary basis for the modelling strategy. Tests were also performed on hardened AISI D2 tool steel (62 HRc), which showed that this material in its hardened state challenges the ability to machine this material in the fully hardened state. The primary tool failure modes are outlined and a detailed analysis of the chip formation mechanisms is reviewed.

Owing to the difficulty associated when machining hardened AISI D2 tool steel, the development of an analytic force model was attempted. The modelling methodology required a correlation of the flow stress (the mechanical response of the material) with the cutting conditions in the form of kinematic parameters derived from chip morphology. The hardened material was characterised using high strain rate ballistic impact tests (using the compressive split Hopkinson pressure bar) in a punching shear configuration. This configuration was chosen as it represented the shearing process in metal cutting more accurately in terms of strain and strain rate. The tests were modified and performed on the fully hardened tool steel. The ultimate result was a precise representation of the flow stress of the hardened material in shear as a function of strain, strain rate and temperature where the fitted correlations represented the experimental data with an accuracy of approximately 10%. The temperatures in this part of the investigation exceeded 600 ^{o}C with strains in excess of unity and strain rates approaching 50000 s^{-1}.

Having a correlation of the flow stress of the fully hardened material, the force model was derived using the chip morphology and chip formation kinematics to represent the governing strain and strain rate conditions during machining. The resulting formulations

allowed for a time domain orthogonal machining simulation represented by specific inputs such as cutting speed and feed rate. The orthogonal formulation was verified against experimental data and showed good correlation with observation.

The orthogonal formulation was extended to the ball milling process (an oblique cutting configuration) to test the validity of the force model. Good correlation was realized between the experimental and predicted results. The ball milling process challenged the validity of the force model by applying the modelling strategy to small chip loads and low cutting speeds. The predicted results also rationalized the tool failure mode that was observed in the ball milling investigation.

Acknowledgments

A long time ago, it was once stated by Professor Tom Wiley that universities are a place for spawning revolutionary thinking. Although the context of this statement was taken as a socio-political revolution, I believe that this statement may be extended into the natural sciences. This of course is only possible when researchers are encouraged to explore those revolutionary ideas. This is not to claim that this dissertation is revolutionary, but fundamentally it is a testament to the supervisory style of Dr. Elbestawi. In his office, there is a plain sheet of paper which states: "for one year of prosperity grow grain, for one hundred years grow trees, and for one thousand years grow people". This says it all about his leadership and commitment to his students, who by the way, he makes feel like family. I am indebted to him in more ways than I can state in such a short space, and therefore I thank him for allowing me to realize my potential and capability.

I am also indebted to my supervisory committee, Dr. G.R. Purdy and Dr. M.P. Sklad for their helpful discussions and providing a star to shoot for throughout my academic career. It is an honour to have known them.

I still get nostalgic about the former IMMRC, as this was the place where friends were made, hardships were fought and a sense of cohesion was built between the special people I had the privilege to know. Special thanks go out to Miky Dumitrescu, Dr. Tahany El-Wardany, Dr. Hossam Kishawy, Dr. Farid Abrari, Dr. Richard Teltz, Dr. Doug Renton, Dr. Trevor Bailey, Ibrahim Deiab, Jim Maclaren, and all the rest who have slowly dissolved away.

My stay at McMaster was made bearable by several friends that whom without, I would not be where I am today. I am indebted to Brian Reeves, John D'Alessio, Joey Kish, and the rest of the gang that supported me when I made the "big jump" in 1996.

Lastly, I would like to express my sincere appreciation to all the faculty, secretaries and staff in the Department of Mechanical Engineering for their friendship throughout my academic career.

I have Just Begun…

Dedicated to my parents András and Sara, my wife Ida, and my precious daughter Allana Sarah, because without her beautiful smile and her cheerful presence, my world would be much less enjoyable.

TABLE OF CONTENTS

CHAPTER 1 INTRODUCTION

CHAPTER 2 LITERATURE REVIEW

CHAPTER 3 BALL MILLING OF HARDENED STEELS

CHAPTER 4 FLOW STRESS CHARACTERIZATION OF AISI D2

CHAPTER 5 OROTHOGONAL FORCE MODEL

CHAPTER 6 OBLIQUE FORCE MODEL FOR BALL MILLING

CHAPTER 7 CONCLUSIONS AND RECOMMENDATIONS

LIST OF FIGURES

LIST OF TABLES

Chapter 1

Introduction

1.1 Rationale and Motivation

The machining of hardened steels is becoming an economical method of metal removal to produce net shape components. This has become possible with the wide use of ultra-hard cutting tool materials such as Cubic Boron Nitride (CBN). Although ultra hard cutting tool materials are available, the physical effects of cutting conditions are not well understood during the cutting process. Thus the objective of the present research is to provide a methodology for an analytical force model used when machining hardened tool steels (in particular AISI D2 in its maximum hardened state). Research conducted on high hardness tool steels (AISI H13 at 55 HRc, and AISI D2 at 62 HRc) provided process optimisation for the ball milling process. The research illustrated that D2 was a particularly difficult to machine alloy, to say the least. The formulation of the force model utilizes material mechanical properties in the form of strain, strain rate and temperature dependence of a constitutive law to represent the shear stresses encountered during metal cutting deformation process. The model was developed to characterize machining process of high hardness tool steels (AISI D2) where saw toothed segmented chips form. The force model provides a unique approach, which does not rely on experimental force model calibration to predict the cutting forces in machining. Based on the present approach, stresses, and to a certain degree, deformation temperatures may be obtained for the chip formation process by means of a time domain simulation developed herein. A force model, which provides insight to stress distributions as well as temperature distributions, can provide a basis for predicting residual stress distributions on the machined surface. Few models to date reach this goal.

Generally, most force models use a mechanistic approach where the model is only inherently valid for the cutting conditions for which it has been calibrated. Further, mechanistic models provide little, if any, insight to critical aspects of machining such as surface integrity, chip formation and temperature distributions. Thus, the motivation of the present research is to address this issue.

Finite element modelling of the machining process generally produces much more accurate results, however the processing costs in terms of speed are generally a disadvantage. Finite element methods also are extremely dependent on the boundary conditions, constitutive equations, and general capabilities of the software. The methods are generally recursive in nature, where "trial and error" implementations are used to produce the desired results. Further, numerical issues regarding numerical stability for small control volumes provide further limitations when using FEA. Analytical simulations are implemented with basic physics and rely on a fundamental understanding of the process. By nature, analytical models are much faster, yield closed form solutions where possible, and are far easier to implement into control strategies.

1.2 Thesis Outline

The thesis is comprised of seven chapters. Chapter two presents the relevant background theory and research conducted in the field of machining. It presents the concepts necessary for an understanding of the research performed in the thesis. In areas where more knowledge is required, additions were placed throughout the manuscript to provide a clearer understanding of the relevant theory.

Chapter three presents the experimental data base acquired for machining hardened tool steels. The focus was placed on optimal cutting conditions, chip formation mechanisms, as well as tool life and tool wear during the ball milling process. Two materials were characterized; AISI H13 at varying hardness and AISI D2 tool steel in its maximum hardened state. The optimal cutting conditions for each material is reported with the a justification of the results. As a supplement, multi-axis machining of the hardened AISI D2 is reported with the optimal cutting conditions obtained from linear cutting test data. Chapter three illustrated the difficulty of machining AISI D2 effectively and introduces the need for a comprehensive force model.

Chapter four presents the high strain rate tests conducted on hardened AISI D2 tool steel. The high strain rate tests performed using the Compressive Split Hopkinson Bar (CSHB) in a punching shear configuration at various temperature provided data to determine explicitly the shear flow stress of hardened AISI D2 tool steel. The experimental difficulties are reported. The shear flow stress is represented using a Johnson-Cook constitutive law that provides the flows stress for hardened D2 tool steel as a function of strain, strain rate, and temperature during deformation. The failure mechanism of the hardened tool steel is reported.

Chapter five provides the explicit formulation of the orthogonal model developed in the present research. Chip formation and morphology was used to provide the kinematic data necessary for the force modelling that was derived from orthogonal turning tests. The orthogonal formulation uses the thermo-mechanical response of the material (developed in chapter 4) to determine the shear tractions on the primary and secondary shear zones. The model is unique in that it computes the deformation temperature dynamically and recursively calculates the flow stress during the deformation. Since the chip morphology is used, compatible strains are determined through empirical representations of the chip morphology obtained from the turning tests and subsequently is represented in terms of feed and cutting speed. Verifying the predicted force levels with experimental data validated the model. Further, the predicted stress levels were compared to finite element results using the constitutive formulation developed in chapter 4. The predicted results of the force model show good agreement between the experimental data and the finite element simulations.

Chapter six is an extension of the orthogonal model to an oblique configuration that represents the ball end milling process. Since the ball milling process provides variations in both cutting speed and undeformed chip thickness for a single cutting condition, it provided a challenging platform for further validating the orthogonal model. Good correlation resulted between the oblique model of the ball milling simulation and the experimental data for larger uncut chip thicknesses. Further, the poor tool life obtained in chapter three was rationalized using the predicted results of the simulation and an explanation of the tool failure mode is presented.

Chapter seven presents a summary of the present research as well as provides suggestions for possible areas of research.

Chapter 2

Literature Review

2.1 Introduction

The present chapter will introduce the basic theory of metal cutting science. The chapter will outline the some theories regarding the kinematics of the machining process, the chip formation process when machining hardened materials and illustrate modelling methodologies currently used in the literature. The chapter will demonstrate the difficulty associated with modelling high strain rate processes such as machining and attempt to rationalize the modelling methodology used in this investigation.

2.2 The Metal Cutting Process

The removal of material in the form of a chip from a workpiece to produce a final shape using a geometrically defined cutting edge can be defined as a metal cutting (or machining) process. Metal cutting is not a cutting process per say, it is in fact a shearing process where the workpiece material is sheared by the edge of the cutting tool to form a chip (Shaw, 1984). The process consists of a cutting tool, the workpiece including a holding fixture, and the machine tool. The interaction of all three combines to form the metal cutting process.

The basic process can be described by following the illustration in figure 2.1. The simplest machining process of shaping (or broaching) can be used to illustrate the concept of machining. The process consists of the workpiece moving with a relative velocity of V with respect to the tool. The tool is considered to be a geometrically defined cutting edge. This means that the tool has a unique geometry that defines the cutting process. The importance of this statement will become apparent as the process is described in more depth. The tool possesses two important features necessary for the cutting process. The rake face of the tool is defined as the face which the chip contacts the cutter. The rake angle designated as α is defined as the angle at which the rake face is oriented to the work-plane and cutting edge. The flank face of the cutter is the face where the new workpiece surface flows past the tool. The flank face of the cutter must have a positive clearance so that the cutting tool will not interfere with the newly generated surface. This is called the relief angle and can be designated as α_r. It should be noted that as the cutting tool wears, a land (or flat) forms on the flank face of the cutter making α_r equal to 0°, which causes interference between the cutting tool and the workpiece surface causing poor surface quality.

Clearly, in order to remove material, the cutting edge must be immersed in the workpiece at a certain depth, f. This is designated as the feed in turning and milling, or as the depth of cut in shaping or broaching. The term 'depth of cut' becomes more appropriate when considering the orthogonal cutting process of machining because the cutting geometry becomes very difficult to visualize in oblique processes. The cutting tool has a defined width (into or out of the page) and is designated commonly as b. It can be seen from figure 2.1 that in order to form a chip (and hence a new surface) the material ahead of the cutting tool at a depth of f, must undergo a change in direction to proceed along the rake face of the cutter. This change in direction occurs in the primary shear zone.

The primary shear zone is of significant importance in the science of machining, as this is one of the areas where considerable energy is expended to form the chip. Thus, the bulk of the chip formation process occurs as a result of the mechanics governed by the primary shear zone. The shape of the shear zone carries considerable importance for the machining process. For the present case, the shear zone is assumed to be a thin plane where the flow changes instantaneously causing the shear to instantaneously occur. The angle at which the plane is oriented with respect to the tool and the workpiece is called the shear angle, ϕ. The shear angel ϕ controls the chip geometry (*i.e.* the deformed chip thickness. f_d), the resolution of the forces, the shear plane area, and determines the strain in continuous chips.

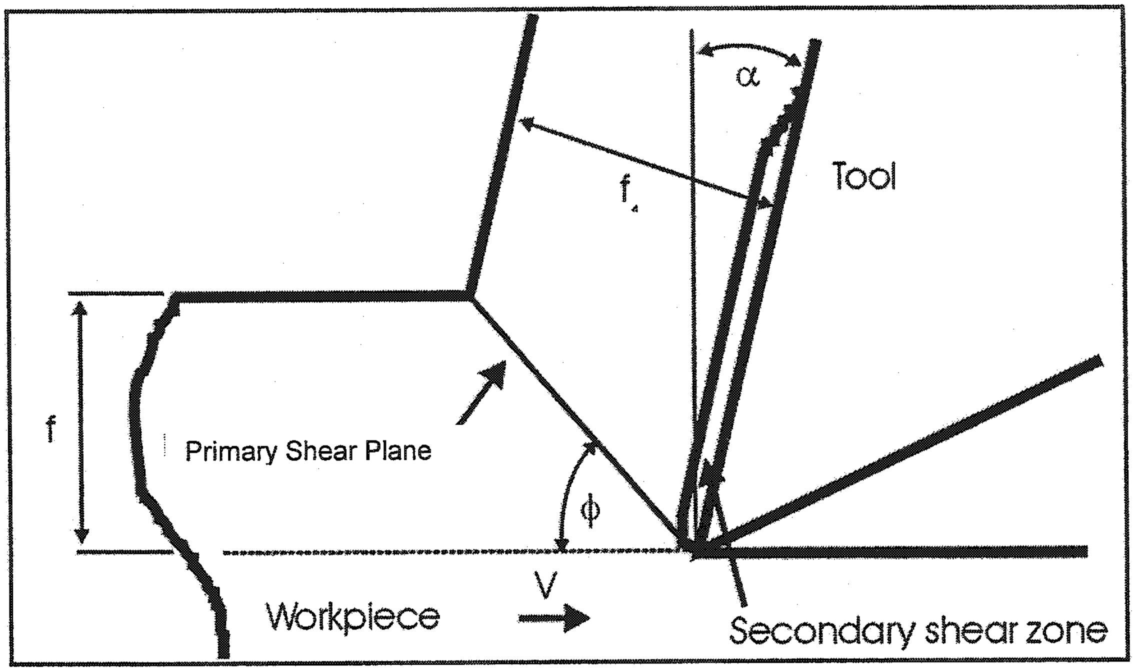

Figure 2.1. The process of metal cutting at the tool/workpiece/chip interface.

The first comprehensive approach to analytically model the metal cutting process was presented by Merchant (1945). He illustrated the kinematic relationship between the shear angle and cutting force. One of Merchant's prime objectives was to predict the value of the shear angle during cutting. He reasoned that the shear angle (ϕ) would possess a value such that the shear stress on the shear plane is a maximum. The shear stress on the primary shear plane is defined as the shear force acting on the shear plane area. Therefore, the expression for the shear stress can be represented by equation 2.1 for continuous chips as:

$$\tau = \frac{Fs}{As} = \frac{R'\cos(\phi - \alpha + \beta)\sin(\phi)}{bf} \qquad (2.1)$$

Equation 2.1 represents the resultant force (R') acting on the primary shear plane area (As) and the geometric relation between the cutting tool, the workpiece and the shear plane angle. It should be noted that in equation 2.1, the friction angle, β, is introduced. β is defined as the angle subtended between the resultant force, R, and the perpendicular component (the normal force, Nc) acting on the rake face of the tool (refer to figure 2.2 for clarification). (The origin of β arises from the effect of friction on the rake face of the cutter and the chip.) When Merchant made the shear stress τ a maximum (by differentiating equation 2.1 with respect to ϕ), the common solution for the lower bound of the shear angle (equation 2.2) is arrived at:

$$\phi = \frac{\pi}{4} + \frac{\alpha}{2} - \frac{\beta}{2} \qquad (2.2)$$

Piispanen (1937) arrived at a similar solution using graphical methods.

Experimentation revealed that the results obtained by Ernst and Merchant provided marginal accuracy (Shaw, 1984, Dautzenburg et al, 1981, Jaspers, 1999). Lee and Scheaffer approached the problem of solving for the shear angle from a different approach (Lee and Sheaffer, 1951). They assumed that the material behaved as a perfectly plastic body and proceeded to solve the slip line field in the vicinity of the shear zone (they also assumed a finite thickness for the primary shear zone of course). The solution obtained from slip line field theory possessed a similar form as equation 2.2 with the exception that the contribution of the friction angle β, and the rake angle α, is enhanced (represented by equation 2.3).

$$\phi = \frac{\pi}{4} + \alpha - \beta \tag{2.3}$$

The two solutions provide an upper and lower bound for the analytic determination of the shear angle.

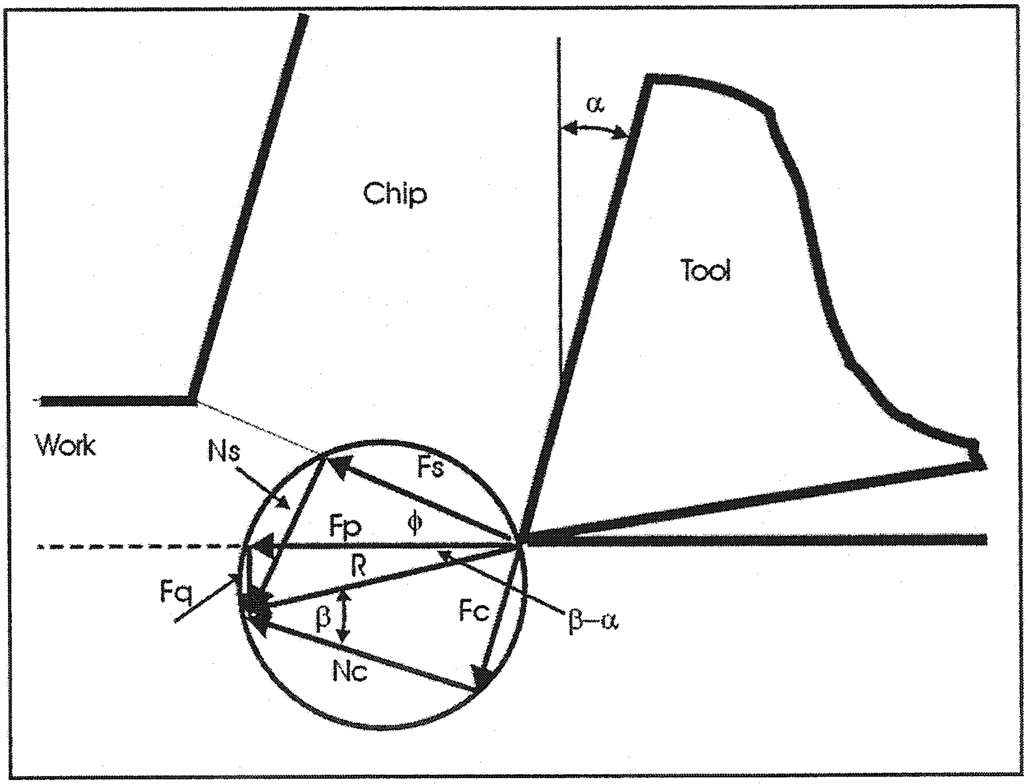

Figure 2.2. Composite cutting force circle. (Merchant, 1945)

Thus, the two solutions given provide a method of determining the shear angle in metal cutting. Reviewing equation 2.1 reveals that if the shear angle, the shear stress and the friction conditions are understood on the rake face of the cutter, a solution for the cutting force during machining presents itself relatively easily. However, the previous attempts have idealized the metal cutting process to such an extent, that precise determination of the cutting force during machining proves to be a problem. An excellent review of modern slip line field formulations can be found outlined in (Fang, et.al., 2001, Fang and Jawahir, 2001).

Mathematically, to solve the complex problem of determining the cutting force, knowledge of several fundamental aspects of the machining process must converge for a complete solution. The flow or shear stress of the material must be known as a function of the cutting conditions (Jawahir et.al, 1998). It is well known that the flow stress of materials are dependant on several key factors during deformation; the strain, the strain rate, and the temperature. Knowledge of these key factors is of the utmost significance to determine the flow stress in metal cutting. Thus, relations for each parameter, which defines the flow stress, must be known *a-priori* to estimate the flow stress. The friction condition on the rake face of the cutting tool must also be known to provide a value for β. Further, the shear angle relationship must also be understood to provide unique value for ϕ. The problem lies in the fact that all unknowns in the formulation are highly coupled. Hence, the determination of the cutting force during machining results in solving for several variable parameters simultaneously with fewer correlations available then is necessarily required. What this means is that to analytically model the metal cutting process, clever simplifications must be assumed to uniquely determine the initial and boundary conditions on the shear plane.

Just as the primary shear zone is important in the chip formation process, a second zone of interest occurs adjacent to the rake face of the cutting tool, which provides the justification of the friction angle β. The region of large deformation adjacent to the rake face on the tool side of the chip is defined as the secondary shear zone and is a direct result of the effect of the friction angle β. Several attempts have been made to determine analytically the value of β. Wright attempted to explain the effect of the stress condition in the secondary shear zone by a direct analysis of the strain rates encountered during cutting (Wright, 1973). He showed that seizure on the rake face of the cutter is responsible for strain rates as high as 10^4 using a high-speed steel cutting tool. Wright presented evidence that temperatures in the secondary shear zone can reach as high as 1000°C. Further, the friction condition on the rake face of the cutting edge is responsible for the crater wear that is observed on the rake face. Gekonde presented evidence that chemical wear is predominant in segmented chip formation by showing that the tool material is slightly dissolved in the chip (Gekonde, 1998). Thus, it can be concluded that secondary shear zone contributes significantly to the machining and chip formation process in general (Jawahir and Zhang, 1995).

As the understanding of metal cutting science has evolved, more sophisticated analytic models have been presented to solve for the shear plane angle solution (Oxley et al., 1977; Oxley, 1989; Zhang et.al, 1991; Ren and Altintas, 2000; Shamoto and Altintas, 1999). Dautzenburg and co-workers (Dautzenburg et al., 1981) have presented a solution to determine the shear plane angle with a work hardening formulation which takes into account the energy expended on the primary shear zone, and the energy expended due to friction on the secondary shear zone. Since the flow law that was used was based on Ludwik's formulation, the solution provided a more reasonable correlation with the experimental they presented. Jaspers (Jaspers, 1999) used a similar correlation to model several issues during the machining of aluminium. The primary difference being that a solution for the temperature in the shear plane was achieved with very good results. Jaspers (Jaspers, 1999) attempted to model the cutting force using a Johnson-Cook and Constitutive law derived from moderate strain rate compression tests for aluminium. His fundamental conclusion was that a constitutive law for shear must be determined to improve the correlation with the experimental evidence (i.e. using the Torsional Split Hopkinson Bar). However, Jaspers correctly points out that the problem with the data correlation does not arise with the constitutive formulation; it results from the models themselves.

Fundamental investigations of the metal cutting process have focussed on attempting to understand the deviations between theory and experimental observation. Several investigators recognized the importance of the material mechanical properties and their relation to the machining process. A fundamental approach taken by Von Turkovich attempted to rationalize the deformation condition of the material as it experiences the intensive shear in the primary shear zone by computing the density of line defects (in terms of generation and annihilation) (Von Turkovich, 1967). He showed that there is a correlation between the shear stress and the effect of line defects. Von Turkovich and Calvo have extended this theory and attempted to rationalize the heat generation in the metal cutting process in terms of physical metallurgy (Von Turkovich and Calvo, 1968). Von Turkovich also showed that shear strains in metal cutting can reach values of 1.5 to 8, and in a subsequent investigation (Von Turkovich, 1970) actually calculated the flow stress and the shear strain (a claimed value of 2) by analysing the effect of line defects in the primary shear zone. Von Turkovich claimed that a shear strain value of 2 (from a calculated strain rate on the order of 10^6-10^7) is a reasonable estimate, although this figure seems rather conservative. Jaspers (Jaspers, 1999) has performed analyses on chips from various materials at moderately high feed rates and has shown that *effective* strains of 3 (shear strains of approximately 6) are obtained in the metal cutting process. Nevertheless, it is remarkable that Von Turkovich obtained somewhat reasonable values of strain and flow stress from such fundamental reasoning. It should be noted here however, that Von Turkovich's approach relies heavily on conjecture and has not incorporated the effect of temperature in the model.

An analysis of the physics of the machining process provides a clear understanding that analytical modelling must incorporate the mechanics and dynamics of the material deformation process, the mechanics of the chip formation process (Jawahir et al., 1998). Thus, considerable focus has been placed on the mechanism and mechanics of the chip formation process.

2.3 Chip Formation

Experimentation has shown that several chip morphologies occur during machining. From a fundamental perspective, the chip formation process is extremely difficult to model. This is because of the deformation conditions, which arise ahead of the cutting tool. Although attempts have been made to analytically model the machining process, the determination of the exact mechanism or combination of mechanisms for generalized chip formation theory has eluded researches. This is because the chip formation mechanism depends upon the metallurgical aspects of the tool-workpiece system and the cutting process parameters. At the turn of the century, the importance of chip formation was recognized. As a result, three main types of chips were classified, namely, continuous, continuous with built up edges, and discontinuous chips.

Some early investigations of metal cutting have been focussed on continuous chip formation as the kinematics are reasonably well understood (from section 2.2). Mallock (1882) presented the first simple model (Lajczok, 1980) for continuous chip formation in orthogonal machining. In this model, it was assumed that the chip formed by a shearing process along a narrow zone that led Merchant to his fundamental theory of the cutting process. Prior to 1926, carbide cutting tool materials did not exist. The only tool material available was high-speed steel. Thus, very low cutting speeds were used in machining. At the very low cutting speeds (less than 23 m/min) associated with high speed steel cutting tools, analysis of chips produced showed that a built up edge occurred on the rake face of the cutting tool. Experimentalists attempted to explain this phenomenon of continuous chips with a built-up edge (Nakayama, 1974). It was hypothesized that the built up edge was a result of periodic adherence of the workpiece material to the cutting edge at low temperatures. This type of chip formation significantly deviates from the classical orthogonal formed continuous chip.

Discontinuous chips are observed during machining of materials that contain points of stress concentration such as the graphite flakes in cast iron at low cutting speeds or when certain materials such as beta brass is machined at extremely low cutting speeds. Field and Merchant (1949) presented a model for discontinuous chip formation. They assumed that the discontinuous chip formation occurs in two stages. However, they did not clarify in their model when the chip segmentation takes place. Cook et al. (1954) observed the process of discontinuous chip formation using a video camera. They concluded that the chips form by a process that resembles an extrusion process ahead of the cutting tool.

The development of advanced cutting tool materials, such as tungsten carbide, introduced higher cutting speeds. As a result, the effective strain rates increased, the temperatures during cutting increased, and the ability to machine much more difficult to cut alloys was realized. With the increase in machining capability came a new type of chip morphology; the serrated chip. Serrated chips are normally formed during machining at high feed rates, high cutting speeds and materials of high hardness or very poor thermal properties. It is mainly attributed to the instability of the cutting process within certain ranges of process variables. Komanduri and Brown (1981) classified the mechanisms of serrated chips as:

a) The Wavy Chip. The wavy chip is symmetrical and resembles a harmonic wave. This type of chip is formed as a result of cyclic variations in the undeformed chip thickness due to regenerative chatter under self-excited vibration. This is attributed to the limited rigidity and low damping of the machine tool system.

b) Catastrophic shear chip. This type of chip occurs during the machining of a certain type of materials whose ability to deform plastically varies with the temperature due to phase transformation and consequent changes in their crystal structure. For example, catastrophic chips are normally formed during the machining of titanium alloys that have poor thermal properties. In other materials, catastrophic chips are formed at very high cutting speeds due to plastic instability in the shear zone, leading to a collapse of the shear front to a localized shear band coincident with the shear plane.

c) Segmented chip. A segmented chip is a continuous chip with periodic variations in thickness. This type of chip is normally formed in a certain range of speeds and cutting conditions and it depends on the composition and microstructure of the workpiece material. The variation of chip thickness due to regenerative effects cannot effectively account for the variation in segmentation thickness. Although the waviness of this type of chip is symmetrical, the deformation within the chip cross-section is not homogeneous.

d) Discontinuous chip. A discontinuous chip is considered a special type of catastrophic shear chip. It is formed due to the periodic rupture along the shear plane. Hence, a complete separation of the chip segments occurs. Details of the nature and mechanism of discontinuous chip formation have been described by Field and Merchant (1949), Cook et al. (1954), and Palmer (1967).

The mechanism of chip formation in hard, or difficult to cut materials has been studied by several authors (Cook et al., 1954; Recht, 1964; Nakayama, 1974; Komanduri and Brown, 1981; Komanduri et al., 1982; Semiatin and Rao, 1983; Nakayama et al., 1988; Sowerby and Chandrasekaran, 1989; König et al., 1990; Shaw and Vyas, 1993; König et al., 1993). It has been stated (Bai and Dodd, 1992) that the pioneering work presented by Recht in 1964 that attempted to explain the mechanism of cyclical chip formation based on the catastrophic shear instability provided a consistent (yet simplistic) description of this type of chip. According to Recht (1964), catastrophic shear instability occurs when the thermal softening effect of the local temperature gradients offset the strengthening effect of strain hardening. Significant work has been done to characterize shear instability in chip formation based on a physical approach (Gekonde, 1998; Subramanian et al, 1999). Gekonde (1998) showed thermal softening is necessary, but not the only factor that governs catastrophic shear instability during chip formation. He showed that geometrical softening has a significant influence on the physics of the deformation process. He also showed that chip the chip morphology correlates well with the variation of the Zener-Hollomon parameter (Bai and Dodd, 1992; Zener and Hollomon, 1944).

Several theories exist for the formation of the segmented chip. Based on the similarity between the morphology of the chips generated during machining of 4340 Steel and Titanium alloy, catastrophic shear instability was proposed as the cause for cyclical chip formation during the machining hardened AISI 4340 steel at high cutting speed (Komanduri et al., 1982; Semiatin and Rao, 1983). Sowerby and Chandrasekaran (1989) suggested that chip segmentation occurs when steel accumulates a certain amount of damage during the machining operation. Thus, the lower the critical accumulated damage factor, the easier it is for steel to exhibit chip segmentation. Using a different concept for chip formation, Nakayama (1974) attributed the nature of cyclical chip formation in hardened steel to the lack of ductility of the workpiece material. Nakayama (1974) proposed that saw toothed chips formed due to shear cracks initiating on the free surface of the workpiece. The formation of cracks is governed by the ductility or the ultimate shear strain of the workpiece material. König et al. (1993) used the same concept to explain the chip formation during hard machining. Recently, Elbestawi et al. (1996) used the concept of surface energy and strain energy density to predict the initiation and propagation angle of surface cracks during hard turning. In their approach, the problem was considered to be a mixed mode crack problem of mode I and II. According to the work presented in their paper, the chip formation in hard turning cannot be fully explained based on the shear deformation process only. Kishawy (1999) spent considerable effort in characterizing the chip microstructure and its relation to process parameters. Several key issues were explored. It was shown that there is a close correlation between the cutting conditions and the chip morphology.

Considerable debate has been presented with regards to the segmented or "saw toothed" type chip. One school of thought considers adiabatic shear instability as the cause of the saw toothed chip formation (Komanduri and Brown, 1981; Recht, 1964) where as others such as Shaw and Vyas (1993), Nakayama (1974), and Elbestawi et.al. (1996) believe that the cause of chip segmentation is a result of crack formation at the free surface ahead of the cutting tool. The most decisive research to date which shows that the crack based approach is valid was recently presented by Poulachon and Moisan for turning hardened AISI 52100 bearing steel (Poulachon and Moisan, 2000). They showed that shear instability may be the cause for chip segmentation for softer material, yet a more global phenomenon is apparent. They observed that for very hard steels, (~750 Hv) crack formation at the free surface does indeed occur due to the brittle nature of the material. In fact, they captured quick stop evidence to show the transformation between shear based and crack based chip morphologies.

It can be seen in the literature that the chip formation mechanisms are important for a fundamental understanding of the cutting process. Several investigators have used chip morphology to ascertain the deformation conditions during cutting (Wang and Liu, 2000, Jaspers, 1999, Komanduri and Brown, 1981, Shaw and Vyas, 2000). This is because of two reasons:

a) Knowledge of the deformation conditions during cutting is not known; it must be observed. This is due to the complexity of the cutting process.

b) The chip morphology contains the entire history of the formation of the chip. The post mortem morphology illustrates the strain conditions experienced during deformation. In some cases, determination of the temperature may be ascertained provided an understanding of the phase transformation temperatures are known.

Thus, due to the uncertain nature of the cutting process, the use of the chip morphology is necessary in understanding the cutting process from a fundamental level. Consistent models of the cutting process must also possess representative data consistent with the chip morphology.

2.4 Force Modelling in Machining

Force modelling in machining provides a significant challenge due to the complex mechanics and mechanisms that are experienced in the metal removal process. Two basic strategies are used when modelling the cutting process. The first and perhaps the most viable for predictive purposes is the mechanistic approach. The second method uses primarily a continuum mechanics approach to solve for the cutting forces, shear angle and the like.

In the most general case, the easiest cutting operation to model is the orthogonal cutting process. The mechanics of orthogonal cutting has been outlined in the previous section to illustrate the physics of the process. When the cutting process deviates from the orthogonal case, that is to say oblique cutting conditions arise, then the mechanics of the process becomes significantly more difficult. In this case, researchers adopt mechanistic type approaches to model the cutting process. The general formulation can be written as:

$$[F] = [K] \bullet [A] \tag{2.5}$$

where [F] is the three-dimensional cutting force vector, and [K] and [A] are matrices which define the cutting process. In 3 dimensional processes, the force vector [F] assigns force values which correlates with the experimental values. The matrix [A] corresponds to the area of cut on the cutting edge. This represents the chip load area. In orthogonal machining, it is generally adopted to use the width of cut (b) and the feed level (f) to calculate the chip load area. There is fundamental logic associated with this. Recall that the cutting force arises from the combined effects of the shear traction (τ) along the shear plane as well as the effect of friction and pressure on the rake face of the cutter. Thus, it seems reasonable to define the matrix [A] to represent the actual area on which deformation occurs i.e. represented by the shear plane area. However, since the shear angle (ϕ) is unknown and is known to vary as a function of cutting conditions, the chip load area is used instead, as these quantities are known and are easily calculated. The formulation of [A] merely reduces the complexity of the modelling.

Since complex machining process requires sophisticated formulations. The simple form of equation 2.5 must somehow represent the cutting process with adequate complexity to model the machining process. The ability to model complex machining processes comes from the formulation of the [K] matrix. This matrix may be thought of as the pressure or stress matrix arising from machining. The matrix [K] may be further reduced to represent the necessary features in the cutting of the cutting process:

$$[\mathrm{K}] = \mathrm{f}(\text{Geometry}, \text{Cutting Conditions}, \text{Tool Geometry}, \text{Friction}\ldots) \tag{2.6}$$

Equation 2.6 shows that [K] is a function of geometry, which is used to represent the geometric effects that arise when cutting with oblique geometries (Yucesan and Altintas, 1994; Tlusty and MacNeil, 1975; Spence and Altintas, 1994; Abrari and Elbestawi, 1998; Clayton et al., 2000, Bailey et al., 2000;). Thus, [K] can be used to represent a correlation of all necessary variables arising from the cutting process to effectively define the cutting process. The interpretation of [K] may be thought of cutting pressure components. However, this interpretation of [K] is misleading due to the mechanistic formulation. The [K] matrix takes into account all mechanical effects, such as rake and lead angle effects (from tool geometry), shear angle variations (due to the response of the material), friction variations (due to the tribilogical effects of the cutting tool material), cutting speed and feed effects (due to process parameter variations which affect the shear stress of the material) *etc.* Virtually all process effects may be accounted for by grouping the combined variation into more sophisticated matrix representations of [K]. This mechanistic type formulation provides good correlation with the experimental data presented in the literature because of the relative ease of simplifying the cutting process to manageable levels within the formulations. The ease and speed of computation makes mechanistic modelling very attractive for implementation into Internet based simulations (as was used by Bailey et al., 2000).

The good correlation of mechanistic models with experimental data not only arises from sophisticated kinematic formulations, but also arises from proper calibration techniques. Various researchers use several calibration strategies. Clayton et al. (2000) used a back propagating neural network algorithm to fit experimental data to provide the coefficients required by his formulation of [K] and was thus able to predict cutting forces in 5 axes. Bailey et al, 2000, used a regression technique by analysing different specific cutting conditions to determine the specific operational coefficients in his model for ball end milling to enable feed scheduling when milling complex geometries. The validity of the results of mechanistic type formulations can thus be attributed to the thoroughness of the calibration strategy. This means that if the formulation is to be valid over a large range of cutting conditions, a large range of cutting conditions must be tested to ensure robust predictions are achieved. More precisely, the sophistication of the correlation coefficients of the [K] matrix relies on the ability to extract the desired effects of each parameter variation modelled in [K]. This includes effects such as friction, tool material variations, speed variations and the like. If an inappropriate number of tests are done to uniquely study the effect of each variation, extrapolation of the model data may provide significant errors when compared to the experimental results. Thus, as the sophistication of the mechanistic formulation is increased, so does the number of tests (or cutting data base) to validate any extrapolation.

Clearly, oblique cutting, such as ball end milling provides a challenging platform to test the validity of any cutting force model. In ball milling, the geometric effects which govern the metal removal process constantly changes and therefore, mechanistic formulations require considerable variations in cutting tests to provide enough data to correlate all coefficients used in the modelling strategy. To avoid this, it was proposed that orthogonal turning data could be used to represent the cutting action for oblique cutting by using an orthogonal to oblique transformation. Yang and Park (1991) showed that by using orthogonal cutting data to determine the parametric variations of the shear stress, the shear angle and friction coefficient, reasonable accuracy can be expected from their simulations. Budak et al. (1996) proposed a "unified mechanics approach" pioneered by Armarego (Armarego et al., 1983, 1985, 1990, 1993) to predict the milling force coefficients from orthogonal turning data. The very important contribution of this work (although still mechanistic in nature) comes from the fact that during orthogonal turning, specific variations of the rake angle, the shear angle, friction and the like can be uniquely studied and determined. From this, extremely accurate formulations into oblique cutting can be used provided the orthogonal to oblique transformation is valid. Thus, by performing orthogonal turning tests, the variation of fundamental parameters such as the shear angle, friction coefficient etc., may be determined with relative ease, greatly enhancing the predicted results from their formulation.

Virtually most force models used for predictive purposes use mechanistic type approaches. However, from a fundamental perspective, mechanistic formulations provide very little insight into the deformation mechanics of the cutting process. With the aim of understanding the physics of metal removal processes, several investigators have used continuum mechanics type of approaches to define the cutting process. Several strategies have been proposed to model the cutting process. Von Turkovich used a dislocation mechanics based formulation to provide shear strains, strain rates and stresses during machining. Although, Von Turkovich avoided any explicit correlation with temperature, it was built into the dislocation regeneration rate, and obtained reasonable results (Von Turkovich, 1970) from his modelling strategy.

As outlined in section 2.2, several investigators used slip line field theory to determine the shear angle during cutting (e.g., Lee and Scheaffer, 1951). The aim in this type of continuum mechanics formulation is to obtain consistent solutions for the shear angle. Once a solution for the shear angle is obtained, determination of the shear stress in the primary shear zone is readily obtained. However, closed form slip line field solutions do not contain the effect of temperature and therefore the force modelling accuracy is questionable.

In continuum mechanics based approaches, as with mechanistic type approaches, the accuracy of the solution depends on the number of variables accounted for in the model. The importance of material properties at high strain rates becomes paramount. This also includes the failure mechanisms that the material experiences under high strain rate deformations. The fundamental parameters that are classically used to define the flow stress of a material are functions of the strain, the strain rate and the temperature response of the material. The relations used for thermo-mechanical modelling of deformation processes are called constitutive laws. Constitutive laws are developed to enable the determination of the flow stress of materials on the complex loading paths that deformation processes take. Using constitutive laws, more sophisticated cutting models can be formulated by incorporating the effect of strain (Lee and Sheaffer, 1951; Oxley 1961), the effect of strain and strain rate (Von Turkovich, 1970) and very recently the incorporation of temperature (Moufki et al., 1997) to predict cutting forces for low carbon (0.2 wt%) steel.

As the modelling methodologies become more sophisticated, analytical/numerical formulations have been developed to determine important characteristics of the machining process such as chip formation (Jawahir and Zhang, 1995, Jawahir et.al., 1998, Fang and Jawahir, 2001, Fang, et.al, 2001, Poulachon et.al, 2001). These publications illustrate the use of analytical methods in determining chip curl through an understanding of the flow characteristics of the material. A precise representation of the physics of the metal shearing process in conjunction with a phenomenological understanding of the flow stress of the material provided the authors with a powerful predictive method for predicting chip formation and forces during machining.

2.5 Constitutive Formulations

The constitutive formulations used to define the flow stress during deformation have several forms. The most basic formulation must represent the flow stress (σ) as a function of strain (ε), strain rate ($\dot{\varepsilon}$) and temperature (T). Thus the flow stress can be represented as:

$$\sigma = f(\varepsilon, \dot{\varepsilon}, T). \tag{2.7}$$

Several functional forms exist, and some are based on empirical formulations such as the Johnson-Cook formulation:

$$\sigma = (A + B\varepsilon^n)(1 + C\log(\frac{\dot{\varepsilon}}{\dot{\varepsilon}_o})(1 - \{\frac{T-293}{T_m - 293}\}^m) \tag{2.8}$$

where A, B, C, n, m, are material constants, σ is the flow stress of the material, ε is the strain, $\dot{\varepsilon}$ is the strain rate, T is the temperature, Tm is the melting temperature and $\dot{\varepsilon}_0$ is a reference strain rate. An assessment of the Johnson-Cook formulation can provide a rationalization of the fundamental meaning of any constitutive formulation. First, it is well known that materials become harder as the strain increases. Thus,

$$\left.\frac{\partial\sigma}{\partial\varepsilon}\right|_{\dot{\varepsilon},T} \geq 0 \tag{2.9}$$

which implies that stress must increase with strain assuming temperature and strain rate are constant. The first term in the parentheses in the Johnson-Cook formulation provides this dependence. Further, interpretation of the constants A and B provide the yield stress

(A) and a hardening modulus (B) for quasi-static, isothermal deformation. This arises from the fact that the Johnson-Cook constitutive law represents plastic behaviour. Thus, at a differentially small positive strain, A obtains the value of the effective yield strength of the material. Formulations representing the flow stress for hardened steels (implying a very large value of A) that possess very small values for A are clearly in error. This arises from merely fitting load displacement data without a comprehensive understanding of the meaning of the constitutive law. Consider for the moment that the effective yield stress of materials varies according to roughly 3 times the Vickers hardness:

$$\bar{\sigma}_{yield} \approx 3Hv \tag{2.10}$$

Thus hardened materials (>600 Hv) must possess effective yield strengths of approximately 1800 Mpa.

Second, it is also well known that most materials respond to increases in strain rate with an apparent increase in flow stress:

$$\left.\frac{\partial\sigma}{\partial\dot{\varepsilon}}\right|_{\varepsilon,T} \geq 0 \tag{2.11}$$

Thus, at constant strain levels and temperature, the flow stress increases. Bai and Dodd have illustrated that the flow stress varies linearly with strain rate for certain levels of strain rate. Figure 2.3 illustrates this behaviour. It should be noted that the changes in strain rate dependence varies from material to material. Figure 2.3 shows that the flow stress behaviour changes roughly 3 times. However, it is not necessary that materials depend on the strain rate according to figure 2. Regions II and III may be combined as in the case of high purity aluminium, or may behave linearly (as in region II) throughout the strain rate regime. Typically, relatively uniform strain rate dependence is observed for strain rates above 10^2 s^{-1} but the effect may become more pronounced at higher strain levels (such as Oxygen Free High Conductivity (OFHC) Copper). Thus, Johnson and Cook have derived their model to represent this logarithmic behaviour.

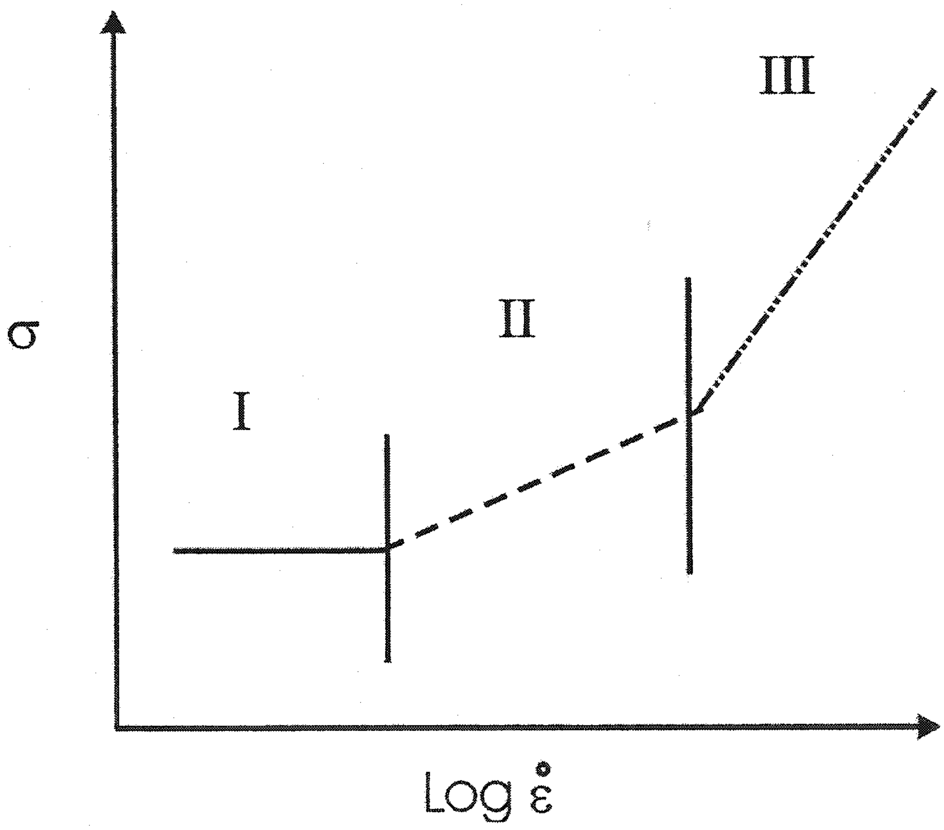

Figure 2.3. Typical flow stress- strain rate behaviour for a material showing at most 3 regions where the strain rate dependence changes.

The third relationship the constitutive law must account for is the flow stress dependence on temperature. It is know that in most cases (with the exception of some nickel based superalloys) that the flow stress of materials decreases with increasing temperature:

$$\left.\frac{\partial\sigma}{\partial T}\right|_{\varepsilon,\dot{\varepsilon}} \leq 0. \tag{2.12}$$

To determine this dependence experimentally, the initial temperature of the alloy is varied and the reduction in flow stress is observed. The last term in the parentheses in equation 2.8 represents the reduction of the flow stress as a function of the normalized (or homologous) temperature. Johnson and Cook used the homologous temperature as a matter of convenience, as it represents the true reduction in flow stress as a ratio of the actual temperature and the melting temperature (in absolute scale). The exponent m, in the formulation determines the sensitivity to thermal softening the alloy's flow stress has. Large values of m provide a small thermal dependence. Further, it should be noted that the Johnson Cook constitutive law does not allow temperatures to reach above the melting temperature of the alloy during deformation. This is because the functional dependence of the flow stress drops to zero (MPa) as the deformation temperature reaches the melting temperature. Thus, any constitutive law must describe the material behaviour (equations 2.9, 2.11, and 2.12) to be consistent.

Several other formulations of constitutive laws exists which claim non-empirical derivations, such as the Zerilli-Armstrong formulation (for BCC structured materials):

$$\sigma = C_0 + C_1 \exp(-C_2 T + C_3 T \ln \dot{\varepsilon}) + C_4 \varepsilon^n \qquad (2.13)$$

Where again, C_i (i=1..4) and n are constants determined from experimental methods. Close observation of equation 2.13 reveals that it meets the criteria outlined by equations 2.9, 2.11 and 2.12. This particular constitutive law was developed using a dislocation mechanics approach and is thus physically based. This means that the coefficients have significant meaning. However, since flow stress data is used to solve for the unknown coefficients, the interpretation of the constants, in terms of activation energies *etc.* may be in question. A physical understanding of the constitutive law is necessary to interpret the meaning of the coefficients.

Constitutive law formulations provide a means of relating flow stress data to the mechanics of the deformation process. However, the question arises, how are the coefficients obtained? Perhaps the most widely used method for determining high strain rate behaviour is derived from the Split Hopkinson Bar test. The details of the shear configuration and the theory behind the Compressive Split Hopkinson Bar test is outlined in chapter 4, section 4.2. The determination of high strain rate flow stress data is challenging to say the least. It was stated that machining is a very high strain rate deformation process. This fact has impeded the use of non-strain rate dependant flow stress models for machining simulations. In fact, some researchers have attempted to use the machining process itself, as a method for determining material high strain rate behaviour (Lei et al., 1997). However, due to the very nature of the machining process, the exact temperature must be known in both the primary and secondary shear zones (and as of yet can only be estimated), as well as the decoupled effects of strain and strain rate.

Thus, one has to be extremely careful when determining the flow stress from machining. The exact kinematics of the shear process is not well known to determine high strain rate flow stress data.

As the material flow stress database increases, and as our understanding of the metal cutting process also expands, the ability to model the cutting process with ever more accurate methods is becoming apparent. It seem appropriate that as the fundamental understanding of the deformation response of materials increases (with valid flow stress correlations (as pointed out by Childs, 1998, and van Luttervelt et.al, 1998)), finite element models are becoming much more accurate in the predictions (El-Wardany et.al., 2001).

Chapter 3

Ball End Milling of Hardened Steels

3.1 Introduction

The present chapter presents the experimental work conducted in high-speed ball end milling of hardened die and mold materials. Two materials (AISI H13 and AISI D2 tool steels) were investigated because of the difficulty associated in machining them in the hardened state. High-speed ball end milling of the first class of die material (AISI H13) proved to be a viable technology. High speed milling of D2 tool steel on the other hand, proved to be a much more formidable task. The chapter is broken into 2 parts; the first part outlines the research conducted on H13, where as the second part introduces the difficulty of machining D2.

3.2 High Speed Milling of AISI H13

Several critical issues involved with the high speed milling of AISI H13 tool steel of ranging in hardness from 45 to 55 HRc have been studied and explained from a detailed analysis of experimental observations. The experiments were performed using several grades of PCBN ball-nose end mills with various edge preparations as recommended by the manufacturer. The effect of different process parameters on the tool performance and the surface finish produced was also investigated. The cutting parameters involved were cutting speeds in the range of 220 to 1320 m/min, feed variation from 0.0254 to 0.1 mm/tooth, axial depth of cut from 0.625 to 2 mm, and a radial width of cut of 0.254 mm. During the experimental investigation, the tilt angle was kept constant at 10 degrees. Several tests were conducted to study the effect of the different tool path directions on the cutting tool performance. Dry and wet cutting conditions were used and the effect of coolant on the tool life was also determined. The optimum cutting conditions, which provide the longest tool life, have been specified based on the modes of tool failure, tool life and surface integrity produced.

3.2.1 Experimental Procedure

The workpiece material used for this investigation was AISI H13 tool steel. This material is typically used as a hot forge die steel because of its high hot hardness. The material was heat treated to 45 and 55 HRc (Rockwell hardness – C scale) to examine the effect of material hardness on the machinability and chip formation. The workpieces were prepared in the form of 50x100x300 mm blocks through hardened and verified by hardness testing. The surfaces of the material were ground to remove the scale left by heat treatment. All edge boundaries were chamfered to remove the effect of sharp loads on the tool life measurements.

The cutting tools were 12.7 mm diameter single tooth ball nose end mills to avoid the influence of tool run-out on wear measurements. Two different grades of PCBN cutting edges brazed on solid carbide shanks were used. Grade 1 was a high volume fraction CBN (90%) with metallic binder and grade 2 was a low volume fraction CBN (65%) with ceramic binder. Three different edge preparations (sharp, honed with a 0.025 mm radius, and chamfered with a 20° angle) were used. The rake angle was kept at –10°, according to (Ikeda et.al., 1992, konig et.al., 1990).

A 10° tilt angle was used as recommended by several investigators (Kruth and Klewais, 1994, Ikeda et al., 1990). The pick feed (fp) was kept constant for all cutting tests at 0.25 mm. The cutting speeds (V) were evaluated for the highest point of engagement on the ball end mill in the range of 220 to 1320 m/min. Table 1 lists the selected variables and their respective values.

Parameter	1	2	3
Spindle Speed (N) (rev/min)	10000	60000	-
Feed (f) (mm/tooth)	0.025	0.05	0.1016
Axial Depth of Cut (ADC) (mm)	0.625	1.125	2.0
Type of Cut	Dry	Flood Coolant	-
CBN Grade (Volume fraction)	High (metallic binder)	Low (ceramic Binder)	-
Edge Preparation	Sharp	Honed	Chamfered
Workpiece hardness (Rockwell C-Scale)	45	55	-
Cutting Path	Perpendicular to pick feed direction	Parallel to pick feed direction	-

Table 3.1 Cutting conditions used for high speed milling of H13.

The cutting force components (Fx, Fy, Fz) were measured using a Kistler 9255 force dynamometer. The length of each cutting path was approximately 300 mm and at the end of each 10th pass, the tool was examined for chipping, breakage, notch wear, or material sticking on the tool rake face. The tool wear was measured using a toolmaker's microscope. The parameters measured to represent the progress of the wear were average and maximum tool wear VB, and VBmax, respectively. The position of the maximum tool wear on the cutting edge was also recorded. The surface roughness of the workpiece was measured at several locations along the length of cut using a portable Mituttoyo stylus instrument. The deviation of the milled surface from the normal surface was measured for evaluating the effect of the tool wear on the geometry of the surface produced.

To study the chip geometry, chips were collected from each cutting test and mounted in an epoxy metallurgical mount, polished, etched, and examined by optical microscopy at magnifications 100X and 1600X. In addition, some of these polished and mounted samples were also examined by Scanning Electron Microscopy (SEM) using back scattered electrons analysis to determine the region of plastic deformation. Samples of the machined surface at the start of cutting and at the end of tool life were taken from the block for examination of surface integrity under the optical and scanning electron microscope.

3.2.2 Chip Formation During High Speed Milling of H13

It can be argued that the most fundamental aspect of metal removal is the understanding of the chip formation mechanics and mechanisms. It was prudent to observe the chip morphology to provide an understanding of the tool life and tool wear mechanisms as a function of material hardness and cutting conditions. It will become apparent in the following chapters how this knowledge may better our understanding of the cutting process.

The end milling process causes geometric effects, which makes the chips produced become thin in the radial direction. This thinning phenomenon becomes much more apparent when small immersion ratios are used as in finish milling. In ball end milling, the axial geometry imposes another axis of thinning, again due to the geometric effects caused by the ball geometry making the effective radius to diminish to zero at the tip of the ball. Thus, owing to the limited period of engagement of the cutting edge for finish milling, the chips produced were short, completely segmented, and of variable thickness caused by the ball end mill geometry. The thinning of the chip in both axial and radial directions is illustrated in Figure 3.1.

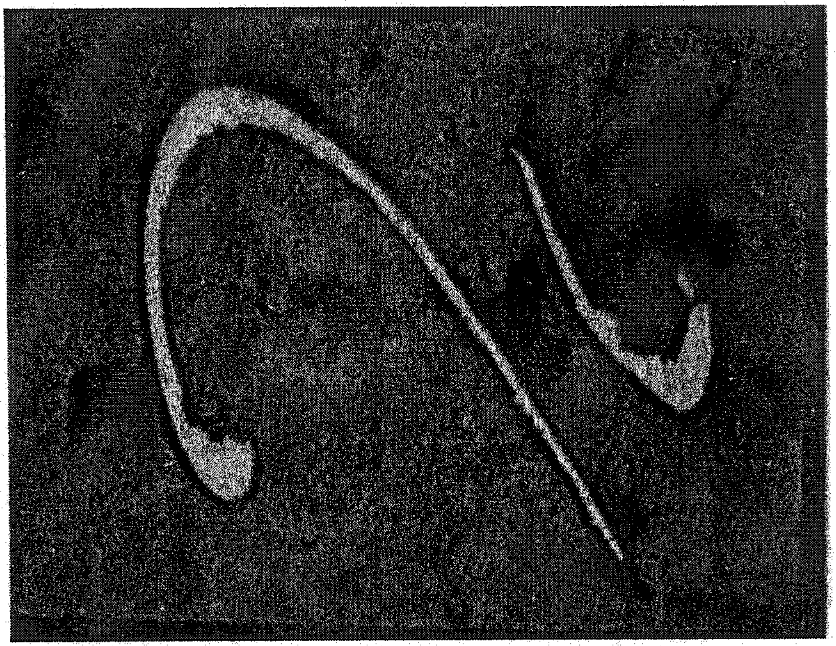

Figure 3.1 Cross section of chip showing radial chip thinning (at two axial positions). (N=10000 RPM, ADOC=0.625 mm, f=0.0254 mm/tooth)

It is well known that material characteristics such as hardness (an indication of the material flow strength) and metallurgy (the elemental composition which gives the alloy its favourable characteristics) affect the cutting and chip formation process. These factors combined with the cutting conditions (such as feed and effective cutting speed) yield the efficiency of the metal removal process. An important factor in any machining process is the temperature associated with the chip formation process.

The variation in hardness of H13 produced differences in temperatures, indicated by the colour of the chips. When milling the 'softer' alloy of hardness 45 HRc, golden coloured -chips were produced at a spindle speed of 10,000 rpm indicating mild temperature effects. On the other hand, dark blue chips were produced during the machining of the 55 HRc workpieces, which indicate much higher temperatures. For the cutting conditions of N =10,000 rpm, f = 0.025 mm/tooth, ADC = 0.625 mm and fp = 0.25 mm, the chips produced are shown in the SEM image of Figure 3.2. The optical microscope image shows that the chip deformed upon tool entrance. However, the chips remain undeformed at the tool exit, because of the thinning phenomenon. Examining the chip cross-section microstructure reveals an extensive shear zone with bulk plastic flow throughout the chip cross-section. The expected saw tooth chips (characteristic of hard machining) were not observed for the 10000 rpm cutting conditions. The effective maximum cutting speed for these cutting conditions was 220 m/min.

(Elbestawi et al., 1996) proposed that the saw toothed chip formation characteristic of hard machining, is a result of a crack propagating from the free surface of the material, and the segmented morphology arises from the termination of the crack in the plastic zone ahead of the tool adjacent to the rake face. The expected saw toothed morphology was not observed due to the extensive shear deformation band covering the entire chip cross section. This was also attributed to the fact that extremely small chip loads were used in the finish milling cutting conditions. Further, as will be shown, the cutting edge condition also attributed to the large plastic zone encompassing the entire cross-section of the chip.

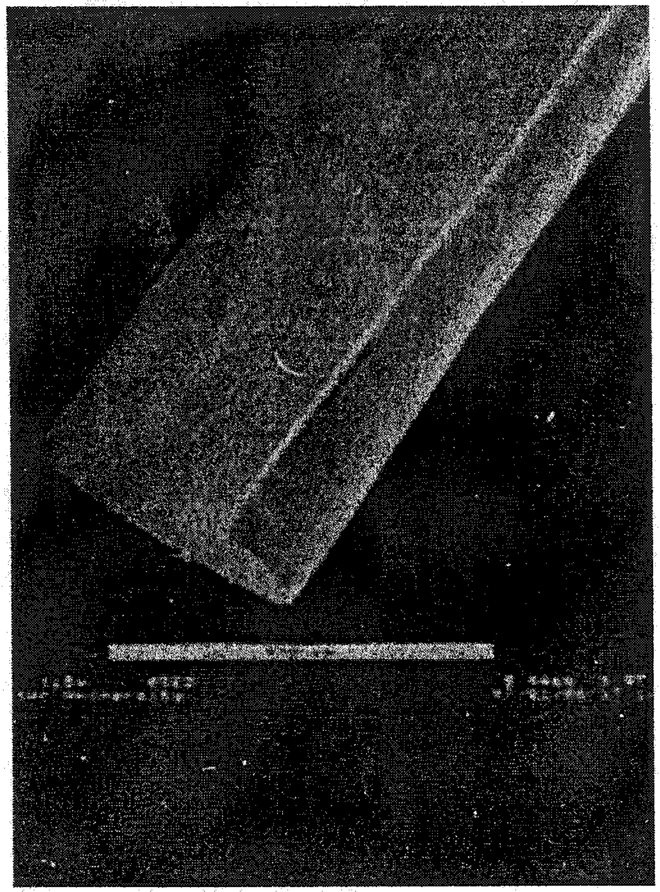

Figure 3.2 a). SEM Image of top of chip

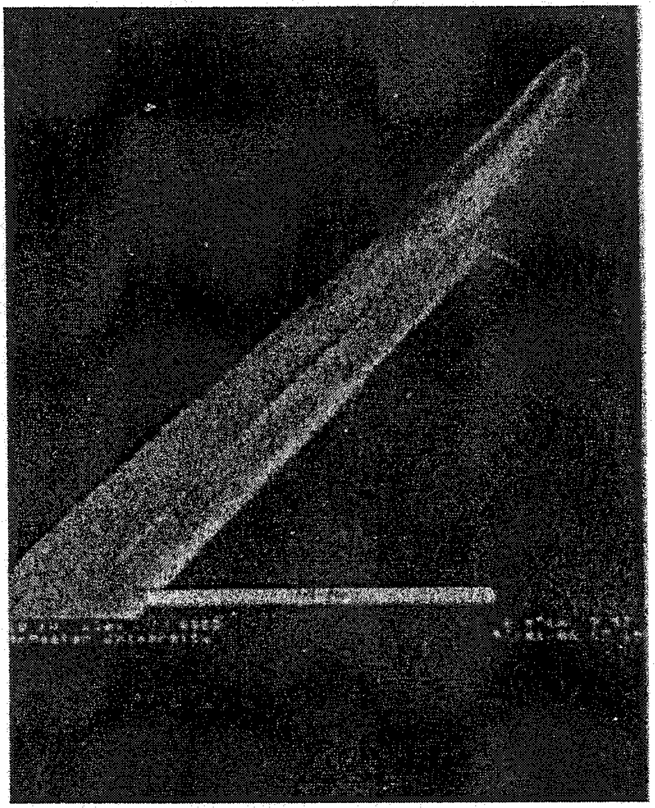

Figure 3.2 b) SEM image of bottom of chip

As the nominal cutting speed of the machining process increased to 60000 RPM, an unexpected morphology occurred. Figure 3.3-a shows an SEM image of the chips produced when a spindle speed of 60,000 rpm is used under the same cutting conditions. The high heat generated at these speeds caused the thinner part of the chip to melt and form small spheres (refer to Figure 3.3-a). Figure 3.3-b illustrates the re-crystallization of this melt upon quenching. The diameter of these spheres is some tenths of a millimeter. Increasing the feed may reduce the possibility of the generation of this morphology. However, with the progress of tool wear, the melting process of the chips was observed.

The cutting edge geometry was found to have a large influence on the production of the spheres.

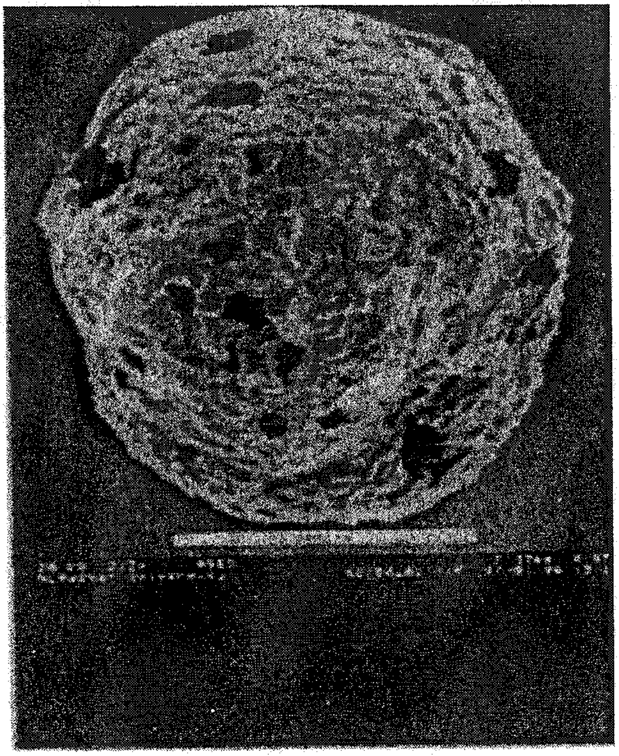

Figure 3.3 a) Spherical chip produced at a spindle speed of 60000 RPM.

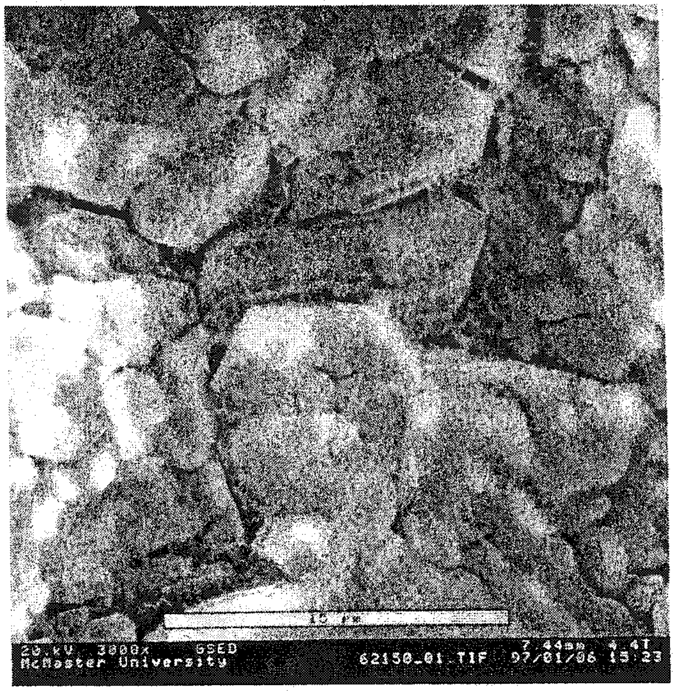

Figure 3.3 b) Microstructure of spherical chip produced at a spindle speed of 60000 RPM.

In general, serrated chips were produced at this high spindle speed. This is illustrated by the SEM image of the free surface of the chip. A cross section of the chip, under optical conditions was impossible to attain due to the very small size of the chips. Again this was due to the small chip loads necessary for finish milling using magnetic bearing spindles. If higher chip loads were used, larger lateral forces would result causing possible failure of the magnetic bearing. Segmentation is evident due to the discontinuous morphology of the free surface of the chip (the face not in contact with the rake face). Figure 3.4-a illustrates the morphology of the chip near the tip of the ball showing that segmentation occurs for the entire speed range. Figure 3.4-b shows an enhanced image of this region.

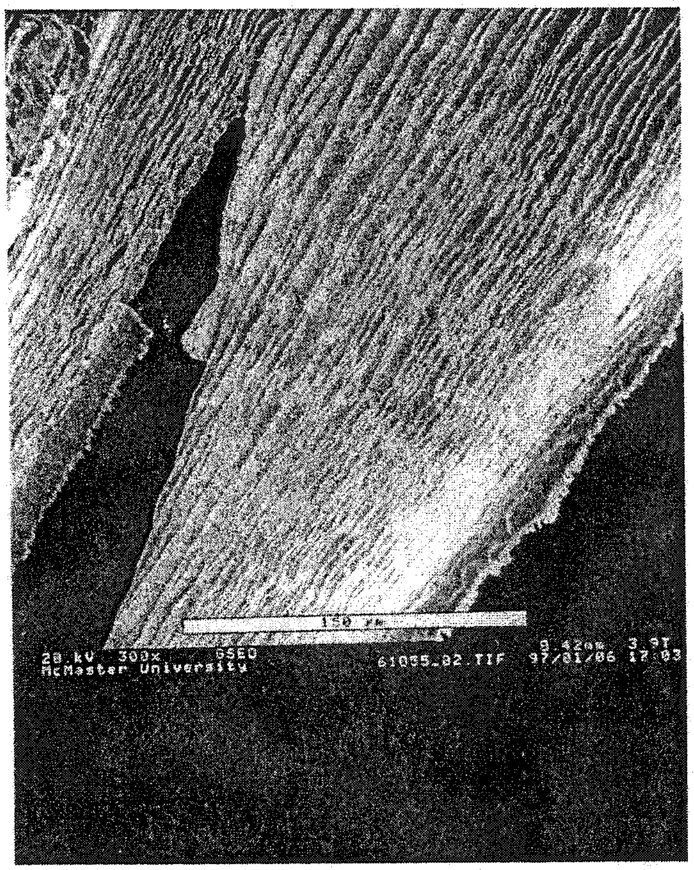

Figure 3.4 a) SEM image of the free surface for a typical chip produced at 60000 RPM showing segmentation over entire chip segment.

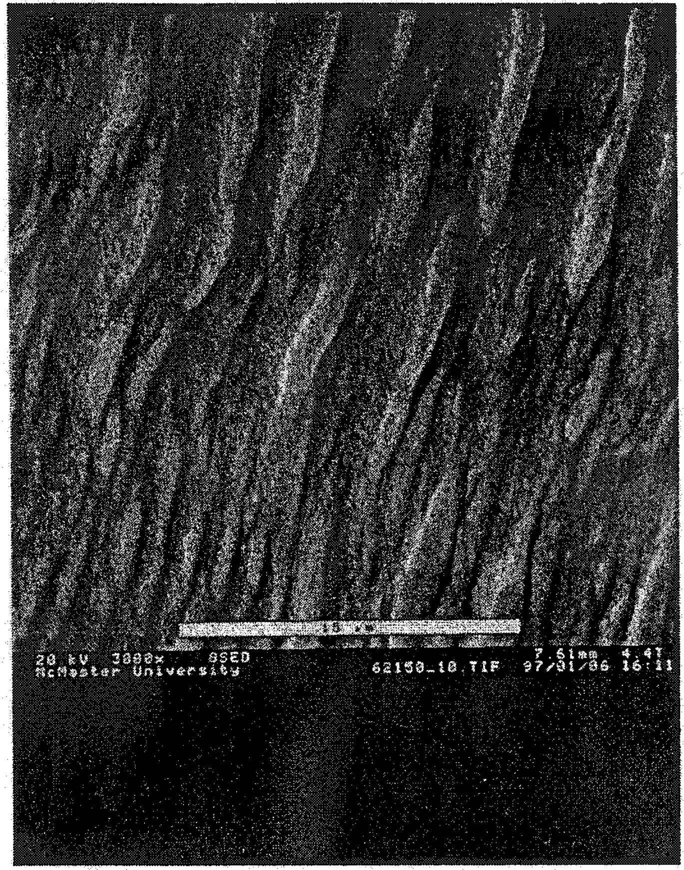

Figure 3.4 b) SEM image of segmented region of chip.

In general, high spindle speeds form the classical saw toothed chip morphology throughout the entire cross section of the chip. Also, the high spindle speeds caused the chip to melt under the given conditions, which was unexpected. This provides us with valuable insight into the cutting process by proving that very high cutting temperatures are encountered at these elevated cutting speeds and high hardness.

3.2.3 Modes of Tool Failure (H13)

In semi finish and finish machining of hardened steel, tool life is taken to be the time needed for the surface finish to deteriorate to a predetermined level. However, in finish machining of dies and molds, it would be misleading to rely solely on the surface roughness to evaluate the tool life of the PCBN tool (Altan et al., 1993). A worn tool may impart a better surface finish than a fresh one (fresh inserts cut well defined scallops resulting in a higher surface roughness). Since worn inserts also have an offset cutting edge, they leave stock on the surface that has to be removed manually (Kruth and Klewais, 1994). In die and mold manufacturing, this type of surface defect should not exceed 0.025 mm and it mainly occurs when the maximum flank wear on the tool exceeds 0.05 mm (Kruth and Klewais, 1994). Hence, the tool life was ended when the level of the maximum flank wear reached 0.075 mm. Different modes of tool failure were observed for the various cutting conditions and are outlined in the previous section.

3.2.3.1 Modes of Failure of High Volume Fraction CBN Tools

There were two grades of CBN tools available for use in this investigation. Grade 1 was a 'high' grade CBN tool material where the binder was a metallic cobalt based material. The volume fraction of the CBN abrasive particles in the binder was approximately 90%. The second grade tool used was a 'low' grade CBN with a ceramic binder. The 'low' grade material had a volume fraction of approximately 65% CBN abrasive and is by no means indicative of the quality of the insert. At the manufacturer's recommendation both grades of CBN were used. It should be noted that the metallic binder CBN (high volume fraction grade) was well suited for the interrupted milling process, where as the low volume fraction ceramic binder was primarily developed for hard turning applications.

The high volume fraction CBN (grade 1) tools failed primarily by reaching maximum specified flank wear for both material hardnesses. However, it should be noted here that for higher chip loads such as a feed of 0.1 mm/tooth, axial depth of cut of 2.0 mm, or when using honed and chamfered cutting edges, plastic deformation of the tool nose has been observed repeatedly. This was found to accelerate the tool wear and cause a faster end to the tool life. An example of this plastic deformation induced failure can be observed from the SEM image in Figure 3.5. Tool chipping was consistently observed when using a honed cutting edge at low feed. This was attributed to the high ploughing force component caused by the large effective rake angles produced by the hone. This occurred because the commanded feed rate was larger than the hone, but the actual chip load was much smaller, due to the radial and axial thinning caused by a 1:50 immersion ratio. Thus, the hone was in effect much larger than the actual chip, giving a highly negative effective rake angle.

It was also observed that catastrophic tool failure occurred when flood coolant was used. The high volume fraction cutting tools were expected to perform well due to the toughness of the metallic binder used. Even so, using flood coolant caused catastrophic tool failure to occur. This was attributed to thermal shock introduced by the coolant. Clearly, as indicated by the chip morphology, the milling process causes high temperatures to be encountered in the region of chip formation. Flood coolant, on the other hand, retained ambient temperatures, and as a result caused large thermal gradients at the maximum depth of cut region (presumably corresponding to the highest temperatures). Differential thermal expansion then caused failure of the cutting edge at the highest point of engagement.

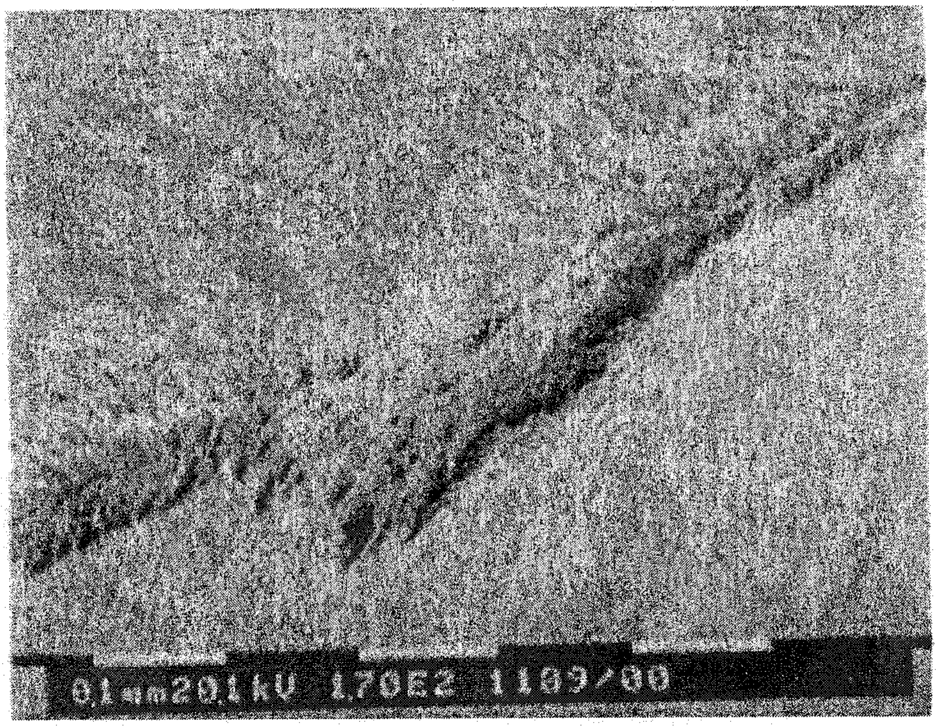

Figure 3.5 Plastic deformation induced chipping of high volume fraction CBN tool.

3.2.3.2 Modes of Failure of Low Volume Fraction CBN Tools

It was observed that low volume fraction (Grade 2) tools failed primarily by edge chipping. Chipping occurred irrespective of the type of edge preparation or cutting conditions used. For honed cutting edges and low feeds, massive chipping was observed after the first cutting pass. For sharp cutting edges, tool wear developed uniformly on the flank until its level was 0.04 mm. Then, plastic deformation started on the tool nose leading to tool chipping. Material adhering on the rake face of the chamfered cutting edges always led to catastrophic failure of the tool at low feed, as shown in figure 3.6. Severe depth of cut notch wear repeatedly occurred when a honed cutting edge was used with flood coolant.

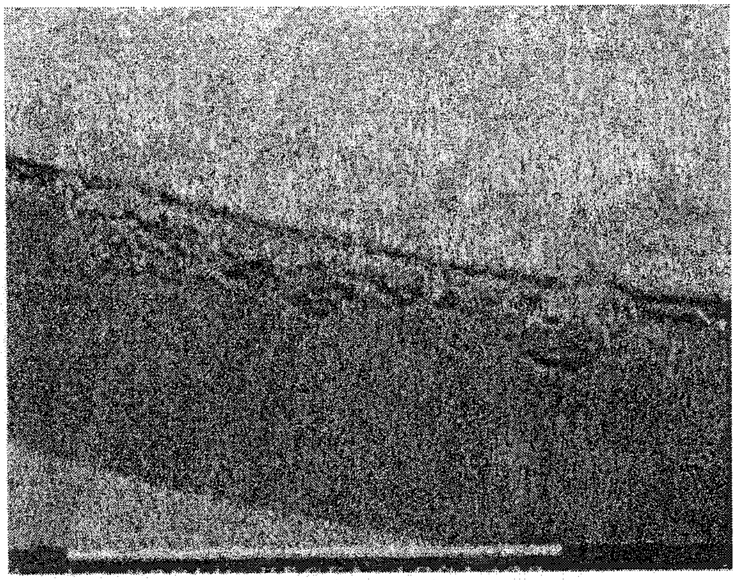

Figure 3.6 Chipping of the cutting edge caused by material adherence for low volume fraction CBN tool. (N=10000 RPM, ADOC=0.625 mm, f=0.1016 mm/rev, H13 55 HRc)

3.2.4 Tool Wear Mechanisms for CBN Tools (H13)

Generally in the early stages of cutting, the tool started to wear at the point where the maximum cutting speed was achieved. With the progress of the cut, uniform tool wear developed along the whole length of contact with the workpiece. Depending on the cutting conditions and the cutting edge preparation, plastic deformation on the rake face may develop and was repeatedly observed before catastrophic failure occurred. This was due to the tool nose deforming in the vicinity of the cut, causing high normal stresses and thus chipping of the cutting edge was initiated.

Figures 3.7-a and b show two SEM images of the tool wear regions. Figure 3.7-a corresponds to the wear developed on the cutting edge at a spindle speed of 10,000 rpm. The figure shows the evidence of material sticking and fine grooves formed on the rake face, and nose deformation. The very smooth surfaces on the rake face near the cutting edge shown in the SEM image may indicate that the binder material (cobalt) in high CBN tool diffuses into the chips produced. This may lower the bonding strength of the tool, allowing the pull-out of the CBN abrasive particles causing abrasive action on the flank. This is consistent with the observed results that little or no crater wear was observed for the ball end mills. The predominant wear occurred primarily on the flank face of the cutter.

Figure 3.7-b shows an SEM image of the tool wear produced during milling at a spindle speed of 60,000 rpm. A protective layer (liquid phase) is deposited on the cutting edge. This protective layer can act as a buffer between the cutting edge and the chip giving rise to the extended tool life observed when milling at the higher speeds. Further, material adherence has also been observed located at intermediate cutting velocities. At the highest contact point (highest velocity), material adhesion was not observed. At the extreme point of contact between the tool and the workpiece, the high temperature generated during machining deforms the softer matrix of the workpiece, leaving the carbide material intact. Thus the possibility of abrasion wear may exist from these carbide particles.

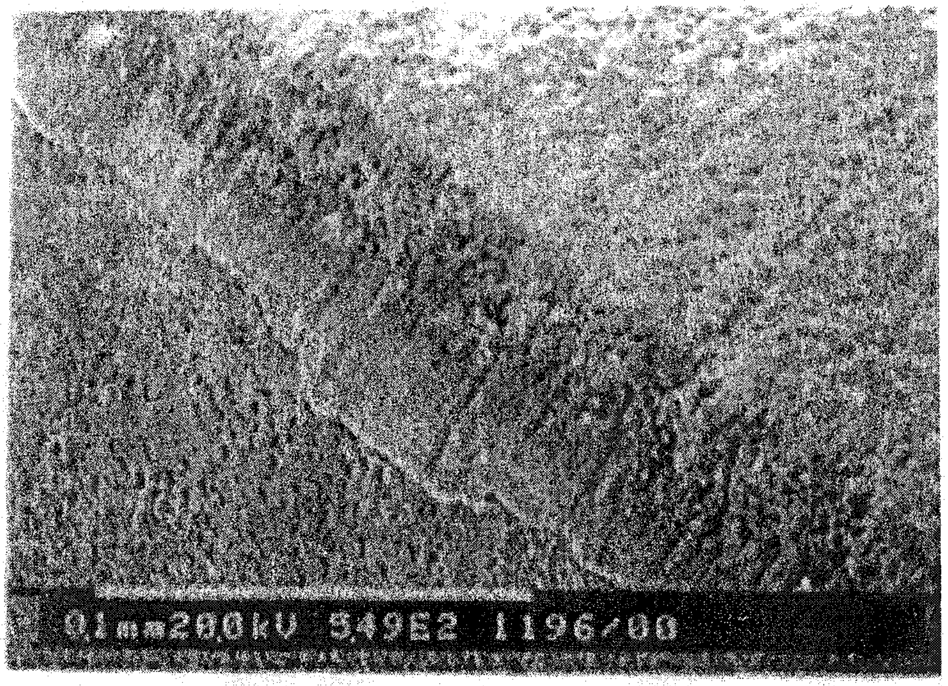

Figure 3.7 a). Tool wear at low cutting speed (10000 RPM, f=0.025mm/rev AISI H13, 55 HRc)

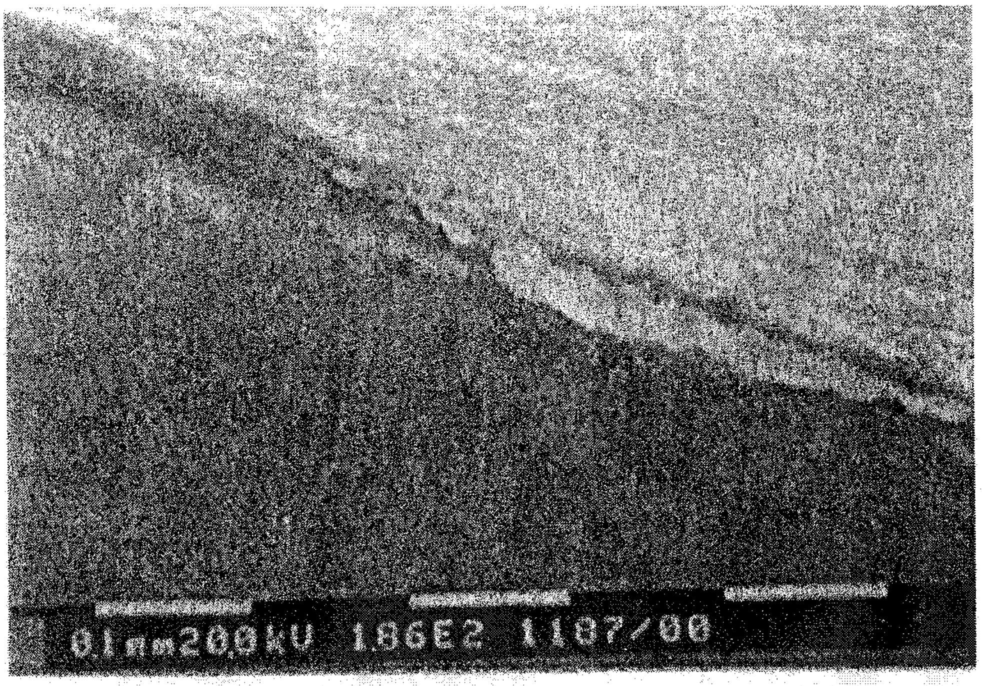

Figure 3.7 b. Tool wear at high cutting speed (N=60000 RPM, f=0.025mm/rev, AISI H13, 55 HRc)

3.2.5 Effect of Process Parameters on Forces for CBN Tools

Figure 3.8 shows a typical trace of the force components measured while end milling at 10,000 rpm spindle speed. As can be seen, the higher force component is in the thrust direction (Fz). Recalling that the workpiece was inclined at 10°, Fz contains components from Fy. Irrespective of the resolution of forces, Fz is considerably higher than the others. This phenomenon can be related to the hard machining process where a pronounced increase in the thrust component is always observed when cutting at low feeds and depths of cut (Konig and Wand, 1987). The use of negative rake angles and a large nose radius generates a ploughing force component, which makes the magnitude of the thrust force component exceed that of the tangential component (El-Wardany et.al. 1995). This is expected since the axial and radial depths of cut were very small and the ploughing process is dominant.

The average resultant force versus cutting time for different spindle speeds, feeds, axial depths of cut and edge preparation were investigated. The average force (within one tooth period) was calculated as the square root of the sum of the squares for the three cutting force components Fx, Fy and Fz. A reduction of the average cutting force occurred with the increase in cutting speed, which can be related to chip thinning, as well as thermal softening (to be addressed later). It should be noted here that the use of a magnetic bearing spindle for the higher speed machining induces large dynamic force components which were four times the actual cutting force. This must be taken into consideration as it will affect the surface finish.

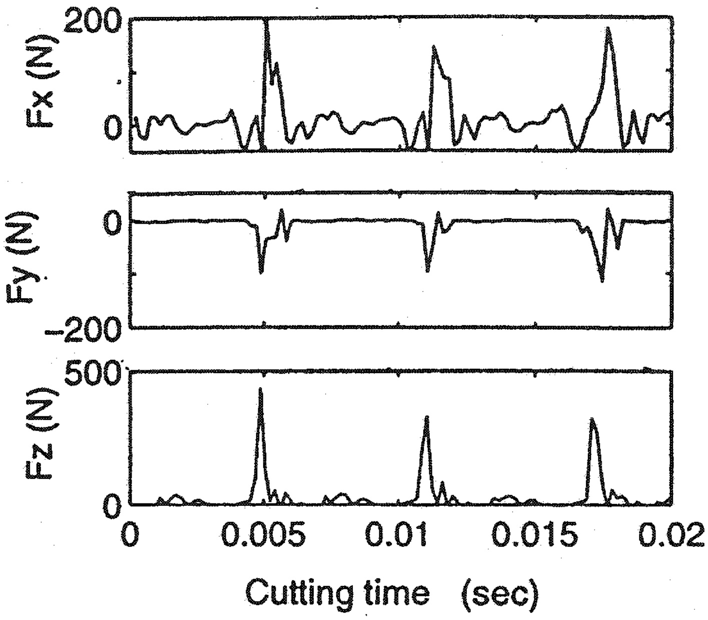

Figure 3.8 Typical force pattern generated during end milling. (N=10000 rpm, f=0.025 mm/tooth, ADC = 0.625 mm, High Volume fraction CBN.

The results from Figure 3.9 indicate that increasing the feed produces a more stable cutting process and a reduction of total cutting force. The dynamic component of the force diminished as the feed was increased due to a more efficient shearing process. This was attributed to a larger effective chip load causing the plowing action to reduce. On the other hand, the cutting edge preparation has a significant effect on the cutting forces generated (Figure 3.9). The cutting forces were the highest when honed edge was used. The highly negative effective rake angle of honed edges result in more ploughing action instead of cutting, which increases the friction force component.

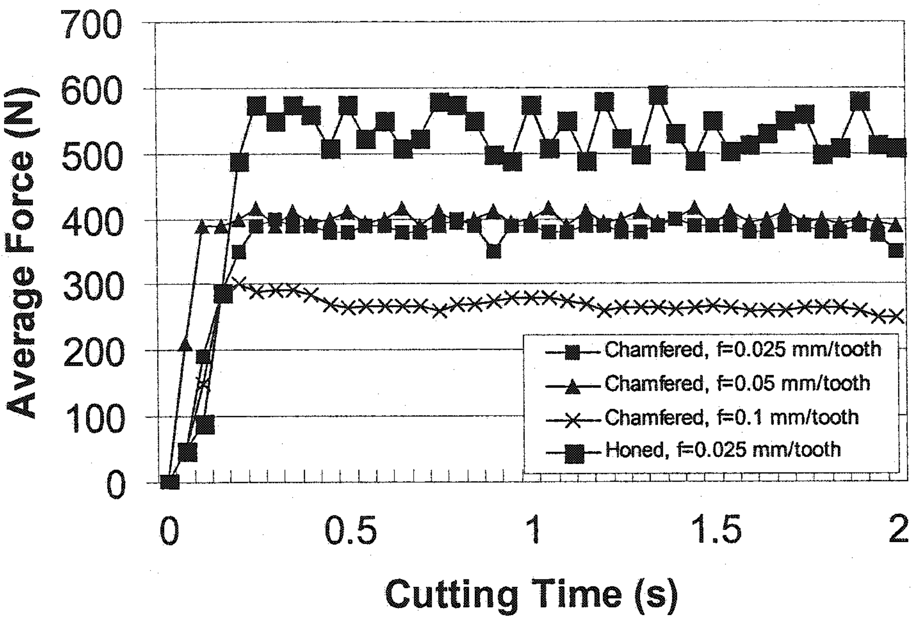

Figure 3.9 Effect of feed and edge preparation on average resulting cutting forces. (N=10000 rpm, high volume fraction CBN, H13 at 55HRc, Hone size = 0.0254mm, Chamfer size = 0.254 mm – 30°)

Increasing the axial depth of cut increases the average resultant forces as the chip width increases (Figure 3.10) which is to be expected due to the larger chip load. It was also observed that the force was strongly dependant on the material hardness. An increase in cutting force was observed for a decrease in hardness of 10 HRc (Figure 10). Figure 3.10 shows that there is approximately 3 times the force to mill the softer material. This illustrates the dependence of cutting forces on the mechanical properties of the alloy.

It is hypothesized that the increase in cutting force can be attributed to the increase in friction on the rake face of the cutting tool, as illustrated by the tool wear mechanism. Material adhesion was predominantly observed as the wear mechanism for the 45 HRc alloy.

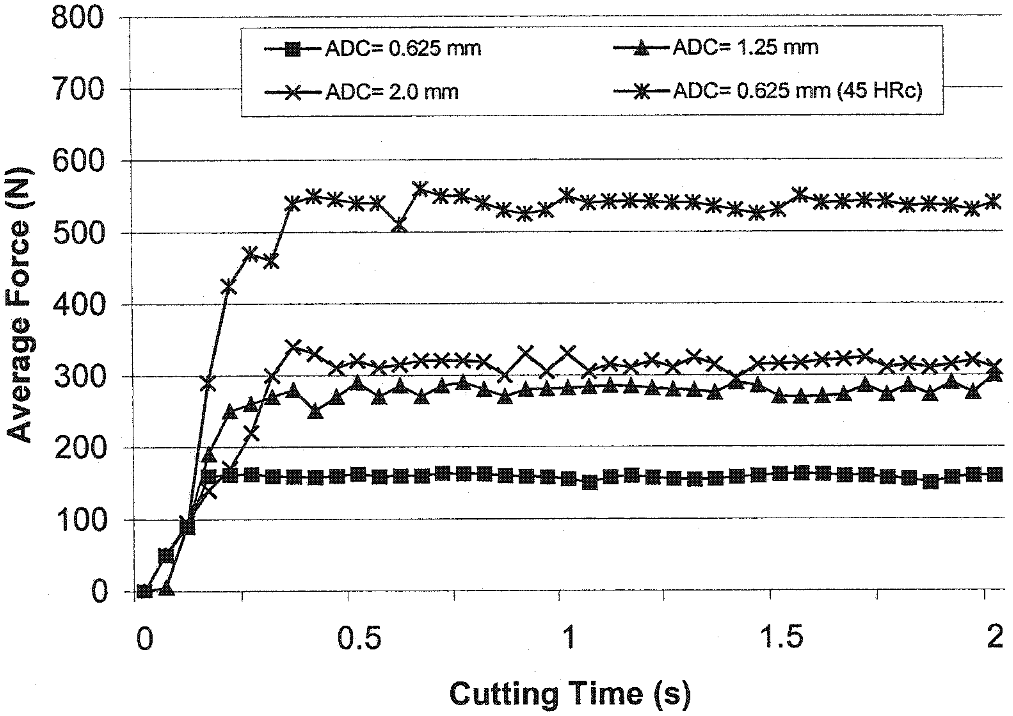

Figure 3.10 Effect of axial depth of cut and workpiece hardness on milling forces (10,000 rpm, high volume fraction CBN)

3.2.6 Effect of Process Parameters on Tool Life for CBN Tools

Figure 3.11 shows the effect of edge preparation, flood coolant, tool material grades and tool path on the performance of the PCBN tools. The best tool performance was obtained when using a high CBN content cutting tool material with a sharp edge preparation. The high CBN grade performed better than the low CBN grade under the given conditions except when flood coolant was used. Since the high CBN cutting tool has a higher apparent thermal conductivity (100 W/m/K), the heat generated during cutting can dissipate rapidly from the cutting zone, thereby diminishing the produced "hot machining effect leaving the material difficult to cut (Konig et.al., 1990). Hence, using flood coolant, a 10-fold reduction in tool life is observed. Further, CBN tools (as with most ceramic materials) have poor thermal shock resistance and, thus, flood coolant application results in rapid tool failure.

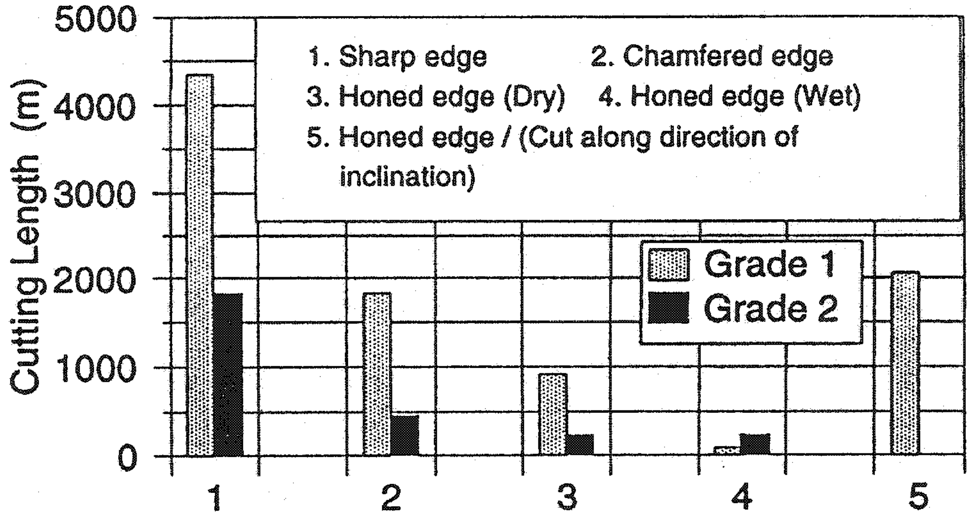

Figure 3.11 Effect of tool edge preparation and use of coolant on tool life.

The high volume fraction CBN tool outperformed the low volume fraction CBN tool because of its higher transverse rupture strength. The microstructures of the high CBN tools show that the void between the CBN particles is filled with a pool of liquid metal infiltrating from the molten tungsten carbide interface (Rai, 1993). The liquid metal pool and the high strength carbide substrate provide additional mechanical support to the polycrystalline CBN layer, which gives high CBN tools favourable impact strength for use in interrupted cutting conditions.

The honed cutting edges gave the worst tool performance. This was unexpected since this edge preparation is usually employed and recommended for finish cuts. This is consistent with the results obtained by Chou et al. (Chou and Barash, 1995). This can be attributed to the large negative effective rake angle of honed edges which result in more ploughing action instead of cutting. This leads to higher friction and tool wear. The tool life of chamfered cutting edges was also less than that of sharp edges. This is because the effective negative rake angle in the case of chamfered cutting edges was -30^o, which caused extensive wear on the rake face noted by a steepening of the tool edge, and chipping.

A noticeable increase in the tool life was obtained when upward cutting was used where the tool axis was inclined in the feed direction with respect to the surface normal. These results were expected since this type of tool path gives the minimum tool-workpiece contact area, as shown in (Chou and Barash, 1995). Also, this type of tool path prevents any engagement between the tip of the ball nose end mill and the workpiece surface. It is well known that in the centre of this tool the cutting speed equals to zero and thus, the effective chip velocity is very small. This leads to cutting edge chipping and a higher wear rate due to a ploughing effect as opposed to a shearing process.

Figure 3.12 shows that wear on high CBN tools decreases as the workpiece hardness increases. Increasing the cutting speed has a limited effect on the tool life as a function of the cutting length when machining the harder H13 workpieces (refer to Figure 3.12). Conversely, when machining the less hard material, the tool life was reduced from 3750m to 1000m length of cut. The variation of chip morphology as a function of workpiece hardness indicates that more heat is generated during the machining of 55 HRc tool steel. The higher the heat generation, the more the chip will be softened and the better the workpiece plastification. This will reduce the mechanical load imposed on the tool and, therefore, less tool wear will exist.

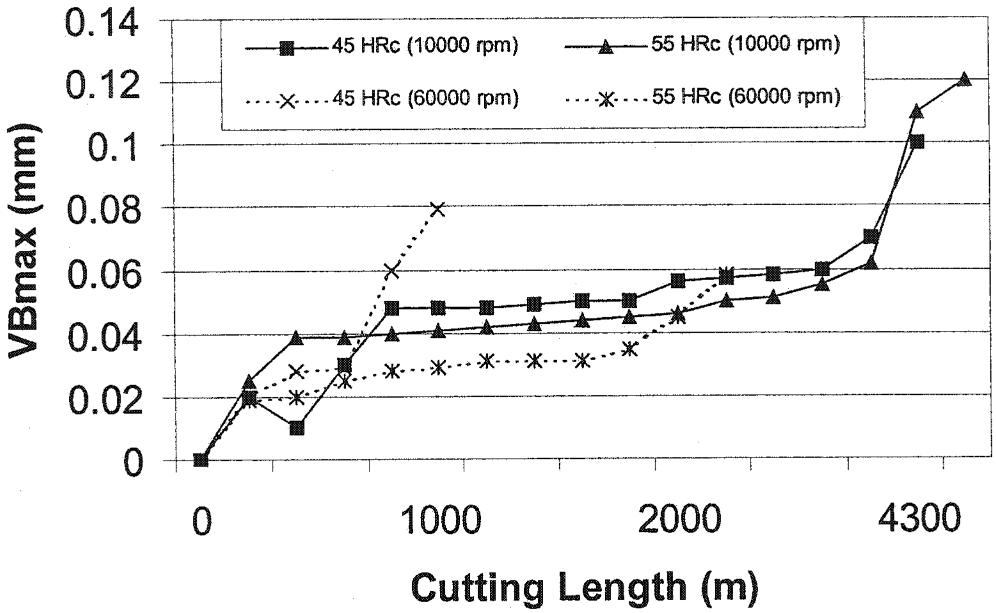

Figure 3.12 Effect of hardness and speed on tool flank wear.

The axial depth of cut in ball end milling determines the effective maximum cutting speed that the tool is subjected to. The effect of varying the axial depth of cut on tool life is shown in figure 3.13-a. It can be seen that the tool life was reduced as the axial depth of cut was decreased. The tool failure mode for the small axial depth of cut was notch wear at the maximum point of engagement. Since the reducing the effective cutting speed (by reducing the effective cutting radius) tends to reduce the temperature, the material did not thermally soften enough for the CBN to cut efficiently. Increasing the axial depth of cut will increase the maximum cutting speed, and therefore the heat generated, and thus increases tool life.

The effect of feed on the tool wear for the cutting edge of both PCBN grades was also explored. In general, it was observed that an increase in the feed reduced the level of tool wear (figure 3.13-b). It is true that a higher feed generally increases the cutting force, but is also increases temperature. It may seem misleading to assume that an increase in chip load will shorten tool life; as the feed is increased, a larger fraction of the heat generated during the shearing process is removed with the chip which, reduces the temperature on the tool. As a consequence, an increase in tool life was observed for a larger feed.

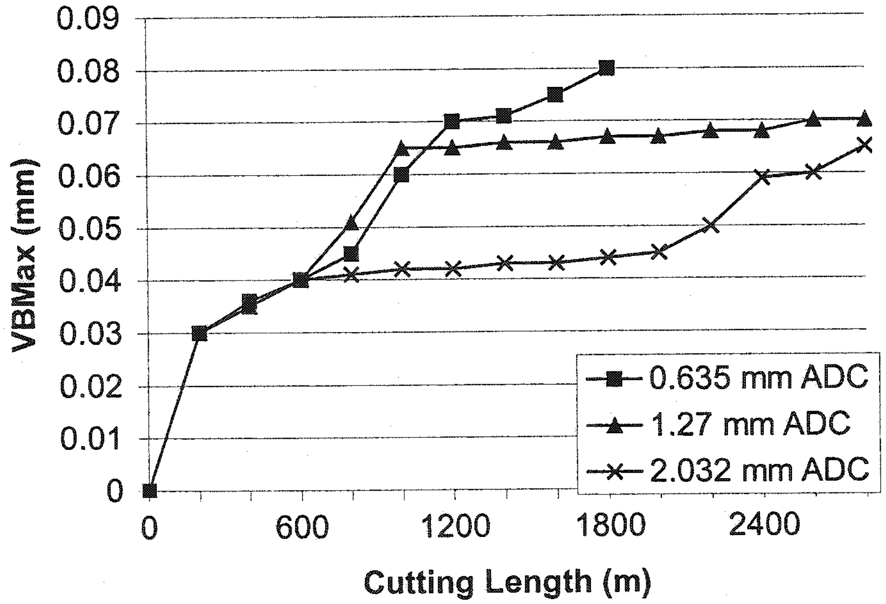

Figure 13-a. Effect of axial depth of cut on tool flank wear.

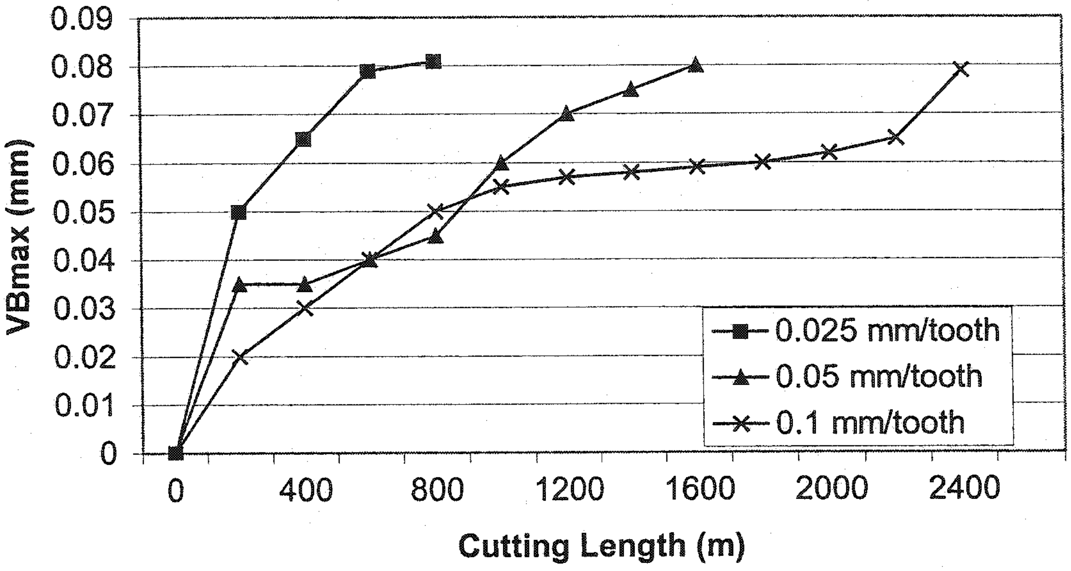

Figure 13-b. Effect of feed on tool flank wear.

3.2.7 Effect of Process Parameters on the Surface Integrity

The feed rates used combined with the high cutting speed and large nose radius consistently produced very good quality surface finishes. Geometric error was found to be in the range of 0.025 mm and it increases to 0.075 mm as the tool wears. The range of surface roughness varied from 0.2 μm (fresh edge) to 0.6 μm (very worn tool) Ra in all cases of the 10,000 rpm speed (e.g. Figure 3.14-a). Rmax was found to be lower for the harder material (2.0 μm) as opposed to less than 4.0 μm for the 45 HR, workpiece. When the magnetic bearing spindle speed was used at 60,000 rpm, the maximum roughness obtained was 66 μm Ra, resulting from the vibration induced to the cutting system by the flexibility of the magnetic spindle. A noticeable increase in surface roughness was not realized as the cut off value of the flank wear is very low for finishing. Hence, the end of tool life was very difficult to gauge from the surface roughness. The value of the roughness when the tool catastrophically failed was obviously very high. At the high spindle speed, Rmax was found to vary contrary to what was observed at low spindle speeds i.e. increasing hardness increases the roughness (figure 3.14-b).

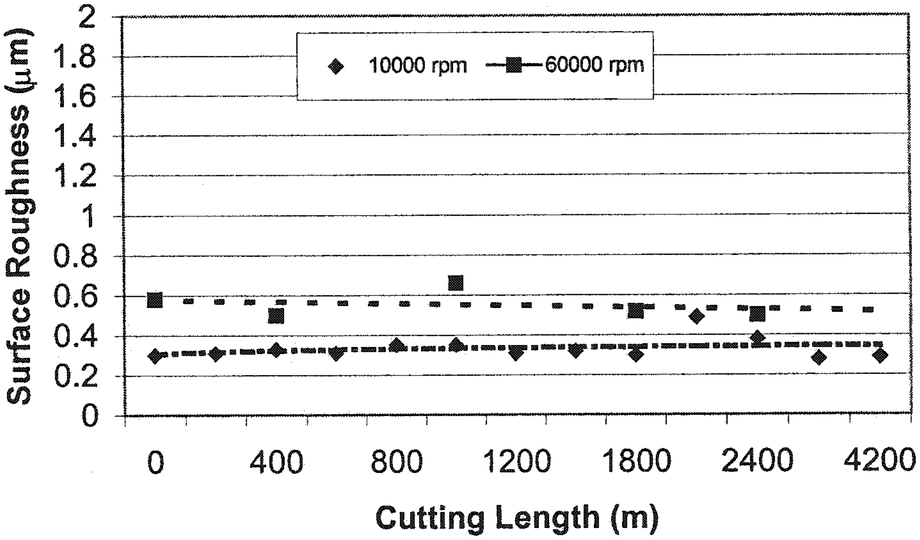

Figure 3.14-a. The effect of cutting speed on surface finish. f=0.025 mm/tooth, ADC=0.625 mm, RWC =0.254 mm, dry cut, sharp cutting edge.

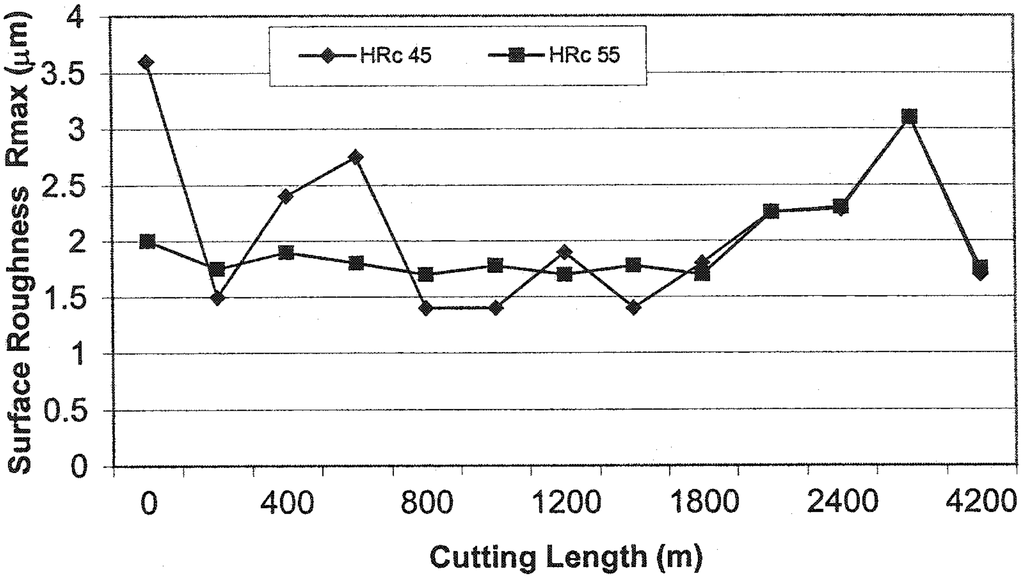

Figure 3-14 b. The effect of hardness on surface finish.

Metallographic examination of the workpiece subsurface revealed that a damaged layer exists a few microns under the cut surface and has a thickness of approximately 4-6 μm. This damaged layer is evident in all of the cuffing conditions. It is metallurgically different than the fine martensitic structure (marked by a difference in contrast) of the bulk material refer to Figure 3.15-a. The workpiece hardness has a great influence on the observable structure of the damaged layer. The 45 HRc workpiece revealed a relatively coarse martensitic structure far under the surface (>20 μm). However near the cut surface, it is apparent that the martensite grains are clearly deformed in the direction of chip flow, refer to figure 3.15-b.

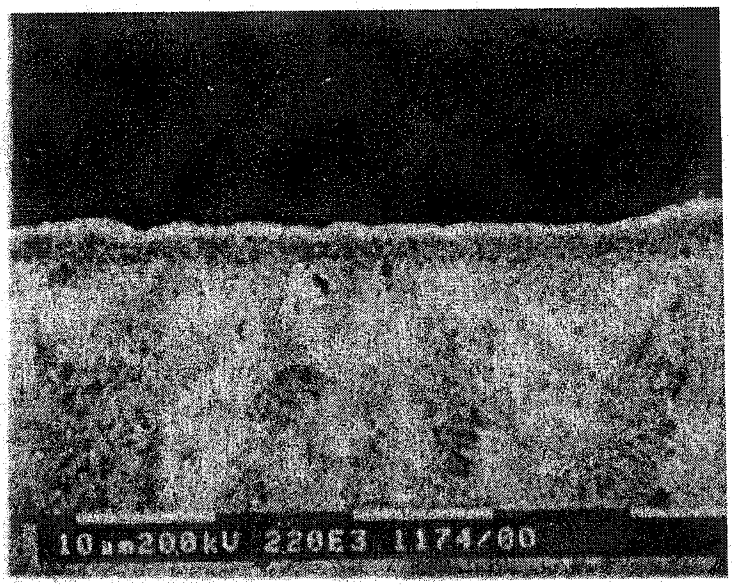

Figure 3.15-a. SEM images of workpiece subsurface damage for H13 at 55 HRc. (N=10000 rpm, f=0.025 mm/tooth, ADC=0.625 mm.)

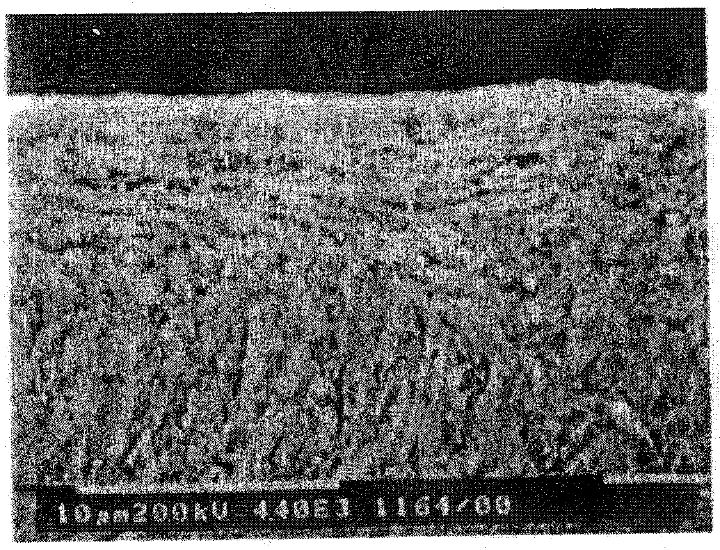

Figure 3.15-b. SEM images of workpiece subsurface damage for H13 at 45 HRc. (N=10000 rpm, f=0.025 mm/tooth, ADC=0.625 mm.)

3.3 High Speed Milling of AISI D2

The remainder of the chapter will be devoted to the difficulties associated in machining AISI D2 tool steel at 62 HRc. The experience gained from successfully milling H13 at 55 HRc was to be employed when machining D2 at 62 HRc. CBN cutting tools were selected with optimal cutting conditions obtained from the previous research for finish milling. The ultimate goal of the experimental work was the successful production of a sculpted die topology in 5 axes. Thus, the research focused on the experimental verification of linear cutting D2 tool steel, and extending the cutting conditions to 5 axes.

3.3.1 Linear Cut Experiments on Hardened AISI D2

Linear cutting tests were performed on hardened AISI D2 tool steel. The workpiece was in the form of 50x100x300 mm blocks hardened to a Rockwell hardness (C-scale) of 62 ± 1 HRc. Each machined surface was previously ground to remove any scale left over from heat treatment. The edges were then beveled to prevent chipping of the cutting tool by providing a uniform chip load on entry.

The cutting tools used were the high volume fraction CBN with a metallic binder for its toughness and wear resistance in interrupted cutting. The cutting tools were 12.5 mm diameter ball nose end mills with a -10° rake angle. The edge preparation used were sharp cutting edges, honed cutting edges with a 0.025 mm radius, and chamfered cutting edge with a 0.025mm T-Land at –20°. The relief angle was 5° to eliminate any rubbing or gouging of the workpiece. The workpiece was initially held at a fixed tilt angle of 10° with the rotary axes on the machine tool locked to minimize vibrations. Further testing required that the tilt angle be adjusted to 25° to increase the cutting speed.

The cutting conditions used are outlined in table 3.2. The feeds, axial depth of cut, radial width of cut, and cutting speeds were based on the results obtained from milling H13 at 55 HRc. Since flood coolant was found to be detrimental to tool life, all cutting tests were conducted under dry cutting conditions.

Cutting Condition	Values Used
Feed (mm/rev)	0.0508, 0.1016
Axial Depth of Cut (ADC in mm)	0.625, 1.125, 2.0
Radial Width of Cut (mm)	0.254
Spindle Speed (rpm)	10000

Table 3.2. Cutting conditions for linear cutting AISI D2 tool steel at 62 HRc.

3.3.2 Linear Cut Experimental Results

The previous section showed that high speed milling of H13 is a viable technology. H13 is considered difficult to cut in the hardened condition. Even so, the tool life obtained from the optimal cutting conditions provided over 4000 m lengths of cut. This translates to a machining time in excess of 4 continuous hours. D2 on the other hand, proved to be very difficult to cut. Aside from metallurgical differences, D2 was merely 7 Rockwell points harder on the C-Scale. This verifies that hardness plays a critical role in the machinability of tool steels. The machining tests conducted on D2 showed that the machinablity was far lower than that of H13.

The results of the milling tests conducted with the CBN end mills are summarized in table 3.3. Table 3.3 presents the conditions used in the experiments and illustrates the mode of tool failure for the cutting tests along with the length of cut expected for each test. The main mode of tool failure for each test was chipping of the cutting edge predominantly at the nose of the cutting tool (slightly above the minimum engagement level). Tests 9 and 10 (marked by an asterisk) were conducted at a 25° tilt angle. These tests were performed to increase the effective cutting speed at the nose of the ball end mill by increasing the effective cutting radius. Figure 3.16 illustrates this phenomenon.

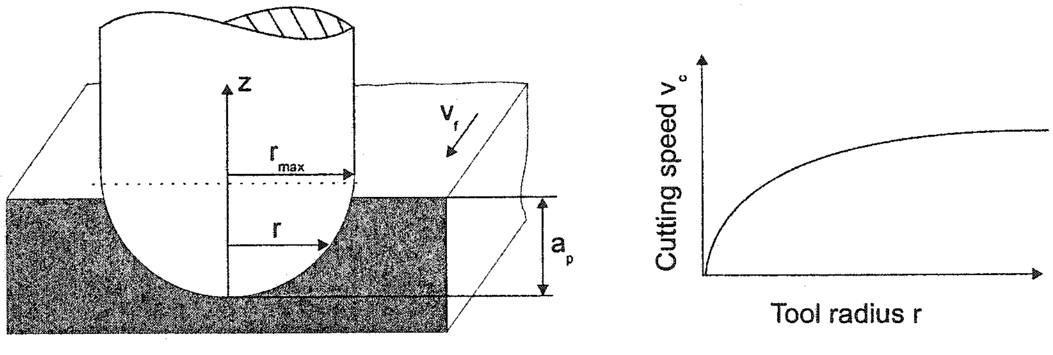

Figure 3.16 The effect of ball radius on the cutting speed from r to r_{max}.

Test #	Edge Preparation	Feed (mm/rev)	Axial Depth of Cut (mm)	Cutting Length (m) (failure mode)
1	Sharp	0.0508	0.625	293 (Chipped minimum point of engagement)
2	Sharp	0.1016	0.625	127 (Chipped minimum point of engagement)
3	Sharp	0.0508	1.125	21 (Chipped minimum point of engagement)
4	Sharp	0.1016	1.125	31 (Catastrophically failed due to chipping)
5	Sharp	0.0508	2.0	146 (Catastrophically failed due to chipping)
6	Sharp	0.1016	2.0	5 (Catastrophically failed due to chipping)
7	Honed	0.0508	0.625	20 (Catastrophically failed due to chipping at minimum)
8	Chamfered	0.0508	0.625	29 (Chipped at minimum point of engagement)
9*	Sharp	0.0508	0.625	98 (Depth of cut notch, and chipping at max.)
10*	Sharp	0.01016	0.625	73 (Chipped minimum point of engagement)

Table 3.3 Results summary of Machining tests on D2 using 12.7 mm CBN ball end mills.

It was thought that an increase in effective cutting speed at the lowest point of engagement would alleviate the chipping problem by increasing the cutting temperature and allow thermal softening the material. The tool failure mode indeed changed, however the tool life was lowered by a factor of 2. This was attributed to the excessive vibrations that occurred at the larger tilt angles. Recall that hard milling produces a large thrust component (z-direction) as illustrated in figures 3.8 and 3.17. At low tilt angles, the z-component of the force is predominantly directed axially along the spindle. Increasing the tilt angle causes the z-component to reduce, but the y and x components become greater in the machine coordinate system. This results in a large force component lateral to the spindle bearings and excites the machine structure more readily.

Several tools failed catastrophically with edge preparations other than the sharp condition. This was due to the excessively high cutting force observed for the tests prior to chipping. Figure 3.17 illustrates the magnitude of the resolved force components (Fx, Fy, Fz) against the tool life for the experimental edge preparations.

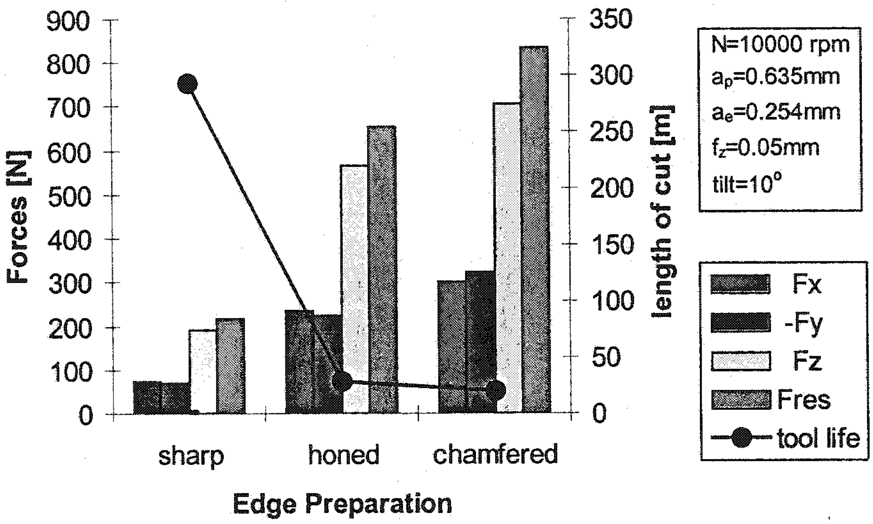

Figure 3.17. Force components and tool life for milling hardened D2 tool steel for various edge preparations (12.7 mm cutter radius).

It can be seen from figure 3.17 that the resultant cutting force increases by nearly a factor of 4 for chamfered cutting edges, and more than double for honed cutting edges. This also indicates that the force is directed primarily into the nose of the ball. The high force values for the non-sharp cutting edges can be attributed to a predominantly ploughing cutting action as opposed to an efficient shearing process. This can be observed from the chips collected from the cutting tests. Figure 3.18-a is a micrograph of a typical chip collected using a honed cutting edge. The chip cross-section reveals an extensive shear zone where high stresses, and high temperatures occurred. Note the presence of several carbides in the chip cross section. The white layer in the chip is presumably transformed martensite, and clearly indicates that the material has undergone phase transformation (Poulachon et al., 2000, Kishawy, 1998). This indicates extremely high temperatures caused by the severe ploughing action from highly negative effective rake angles. This is in contrast to figure 3.18-b using a sharp tool. The undeformed segments in the chip cross section are much more apparent, as is a reduction of the transformed shear band. The white layer is not expected to occur on the workpiece surface, as it is primarily a result of tool flank wear (Kishawy, 1998).

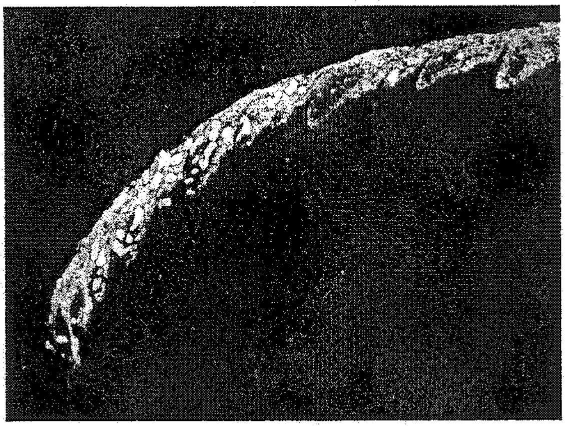

Figure 3.18-a. Micrograph of chip formed during cutting D2 with a honed cutting edge. (N=10000 RPM, ADOC =0.625 mm, f=0.0254mm/tooth, 38 mm diameter high volume fraction CBN ball end mill).

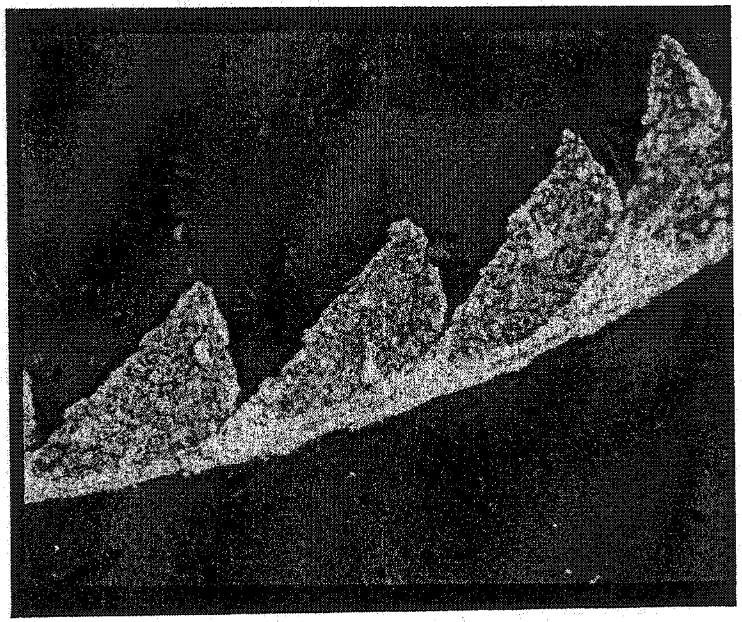

Figure 3.18-b. Micrograph of chip formed during cutting D2 with a sharp cutting edge. (N=10000 RPM, ADOC =0.625 mm, f=0.1016 mm/tooth, 38 mm diameter high volume fraction CBN ball end mill).

The ultimate goal of the experimental work was to produce sculpted die topography in hardened D2. Due to the poor tool life observed for the 12.7 mm ball nose end mills, it was concluded that a higher cutting speed was needed to cause softening the material to observe an increase in functional tool life. Since the maximum spindle speed of the machine tool was limited to 10000 rpm, it was concluded that in increase in effective diameter of the ball end mill was needed. As a result, tests were conducted using ball end mills with a diameter 38.1 mm. A nominal increase of cutting speed from 220 m/min to 317 m/min was immediately realized.

The results of the tests preformed for the 38.1 mm diameter ball end mills are summarized in table 3.4. It was found that a feed of 0.0508 mm/tooth, a 10° tilt angle, an axial depth of cut of 0.625 mm and a radial width of cut of 0.254 mm was the best cutting condition to maximize tool life. This was consistent with the experience gained from the 12.7 mm diameter ball end mills.

Test #	Axial Depth of Cut (mm)	Radial Width of Cut (mm)	Feed (mm/tooth)	Tilt angle (degrees off horizontal)	Tool Life (m) and failure mode
1	0.625	0.254	0.0508	10	234 (Chipped at min. speed)
2	0.625	0.254	0.1016	10	219 (Chipped at min. speed)
3	0.625	0.508	0.0508	10	69 (chipped in middle)
4	0.625	0.254	0.0508	25	146 (Chipped at max. speed)
5	0.625	0.508	0.0508	25	35 (Chipped at max. speed)

Table 3.4 Results summary of Machining tests on D2 using 38.1 mm CBN ball end mills.

The results of tests 4 and 5 (from table 3.4) merit further discussion. These tests were conducted to determine if the cutting speed could be increase further to improve the tool life. Increasing the tilt angle increased the effective cutting speed, however the increased radius of the ball created much higher cutting speeds. High speed machining is a relative term; high speed when cutting aluminum or cast iron may be of the order of 2000 m/min cutting speeds, where as for titanium, high speed is anything above 50 m/min. Thus, high speed for D2 in the hardened state may be interpreted as less than 370 m/min. Above this cutting speed, catastrophic tool failure was found to be imminent.

The previous cutting tests determined the optimal cutting conditions for linear cutting hardened D2. The results obtained were extended to the production of a 5 axis die surface to verify the validity of the data.

3.4 Multi-Axis Cutting of a Die Cavity in Hardened AISI D2

A forging die cavity was designed to represent the typical features in dies and molds and to simulate several effects resulting from complex tool path generation. Cutting tool materials used were coated carbide for the roughing and semi-finishing processes and Cubic Boron Nitride (CBN) for the finishing process. The effects of complex tool paths on several critical machining issues such as chip morphology, tool wear mechanisms, tool life, and surface integrity are presented.

3.4.1 3D Solid Modelling and NC Preparation of a Pocket

The pocket designed for this investigation represents the features of a medium size die or mold. A 3D commercial CAD/CAM system was used to generate the free form surface of the pocket depicted in figure 3.19. The surface was designed such that tool gouging was eliminated.

The geometry of the surface was then transferred into the NC programming system to generate a 5-axis, unidirectional flow line tool path. Flow line machining was utilized to provide uniform scallop heights around the surface, to facilitate the editing of the post processor program, to allow the use of down milling process, and to enable stopping the machine after each 10th pass to gauge tool life. The instantaneous variation of the tilt angle was minimized by keeping the CL data points very close together, nominally 0.025 mm apart for finishing and 0.254 mm for roughing and semi finishing. Setting the CL data points much closer affected the prescribed feed rates, which were rarely achieved by the machine controller due to processing limitations, as well as excessive rotations inherent in 5-axis machining. The pre-specified feed was incorporated in the post processor to yield inverse time feed commands. This was necessary because the machine controller can not interpret conventional (mm/min) feed commands in rotary motion even though the physical interpolation between consecutive points are linear.

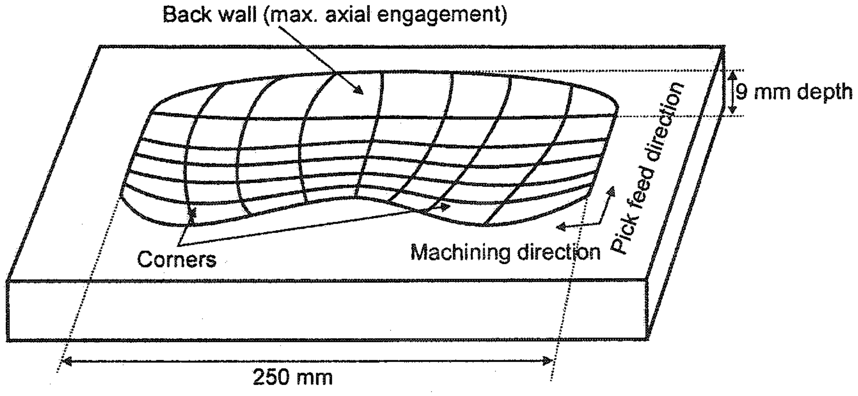

Figure 3.19. Generic pocket created to illustrate the effects of cornering when High speed machining hardened tool steels.

3.4.2 Experimental Procedure for Pocket Milling

Dry milling tests were performed using ball nose end mills. The workpiece material was D2 (63 HRc) tool steel prepared in the form of 50x100x300 mm blocks. Coated carbide inserts were used for roughing and semi-finishing of the pocket. The cutter diameter was 12.7 mm and the rake angle was 0°. For the finishing process, 91% volume fraction PCBN with cobalt binder and sharp edge preparation tools were used. The cutter diameter was 38.1 mm and rake angle was -10°. All tools were balanced for high spindle speeds. The optimum cutting conditions for both roughing and finishing processes were obtained from previous investigations (Elbestawi et.al., 1997, Boehner et.al., 1999) conducted for straight milling tests. The spindle rotational speed was kept constant (6000 rpm for roughing and 10,000 rpm for finishing) for all tests. The cutting conditions are listed in Table 3.5.

	Speed V (m/min)		Feed f (mm/ tooth)	Axial depth of cut (mm)	Radial width of cut (mm)
	min	Max			
Roughing	101	238	0.1016	1.905	0.635
Semi-finish	101	170	0.1016	1.25	0.635
Finishing	207	1197	0.0508	0.635	0.254

Table 3.5. Cutting conditions obtained from the pocket machining process.

The cutting force components (Fx, Fy, Fz) were measured using a Kistler Type 9255b table force dynamometer. The dynamometer was secured to the rotary table using the recommended 8-bolt pattern providing a flat response up to 2.4kHz. At the end of each 10th pass the tool was examined for chipping, breakage, notch wear, or material sticking on the tool rake face using a toolmaker's microscope of 20x magnification. The parameters measured to represent the progress of the wear were average and maximum tool wear V_{Bb} and V_{bmax} respectively. The position of the maximum tool wear on the cutting edge was recorded. At the end of the tool life, the tools were examined by scanning electron microscopy (SEM) to study the different mechanisms of tool wear. Chips were collected and mounted in an epoxy metallurgical mount, polished, etched and examined by optical microscopy at high magnifications. The surface roughness was measured after each 10th pass.

3.4.3 Experimental Results for Pocket Milling

The variation of the instantaneous tilt angle (one of the main features in 5-axis machining) as well as geometric influences of the die surface topography caused a non-uniform chip load during the milling of the cavity. Also, variable axial depths of cut occur due to the cornering of the tool path, combined with the various rotations of the rotary axis. These phenomena affect the pattern of chip morphology, tool wear mechanisms, cutting forces and tool life.

3.4.3.1 Chip Morphology during Roughing

The chip formation process in 5-axis roughing was similar to linear cut test data (Elbestawi et.al., 1997). All roughing conditions produced saw toothed chips with a white layer formed on the secondary shear zone. However, the size of the chips produced during the 5 axis roughing process varied substantially indicating a variation in the instantaneous chip load. Figure 3.20 shows chip cross sections produced by sharp and worn tools.

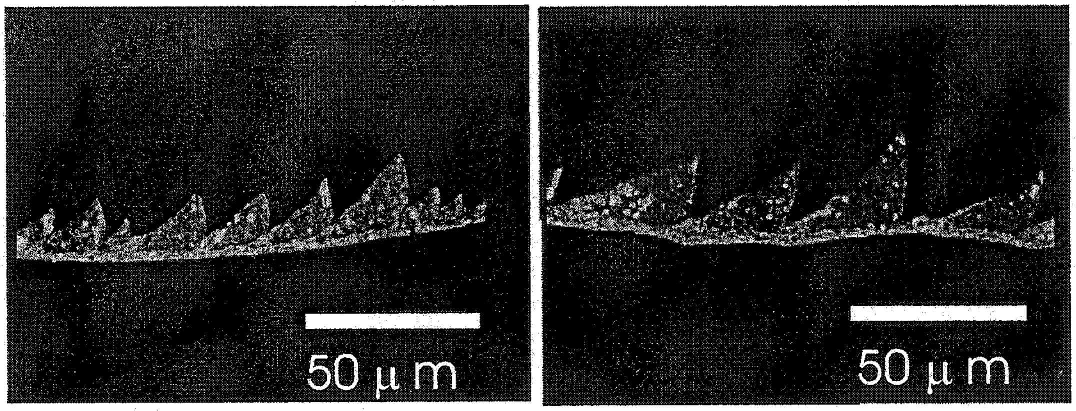

a) Sharp Tool b) Worn Tool

Figure 3.20 Chips produced during roughing using coated carbide ball end mills.

3.4.3.2 Chip Morphology during Finishing

Non-uniform saw toothed chips were formed during 5-axis finishing of D2 tool steel with CBN tools. The chips produced were blue at the thickest portion whereas the thin sections were straw colored. During the milling of the wall (attributed to the maximum cutting speeds of 1197 m/min), the chips produced where white hot, and as tool wear progressed, the chips produced appeared oxidized, characterized by a dull finish. Excessive chip thinning was also observed at high cutting speeds as seen in figure 3.21. The maximum chip thickness was smaller than the mean grain size of the workpiece material because of the low feeds. Several chips were also observed where melted chip segments adhered to the free surface of the chip in the form of recrystallized spheres as in the 60000 rpm machining of H13. This indicates extremely high temperatures were generated in the primary and secondary shear zones (greater than the melting temperature of the tool steel). Thus, the shearing process has produced significant thermal energy.

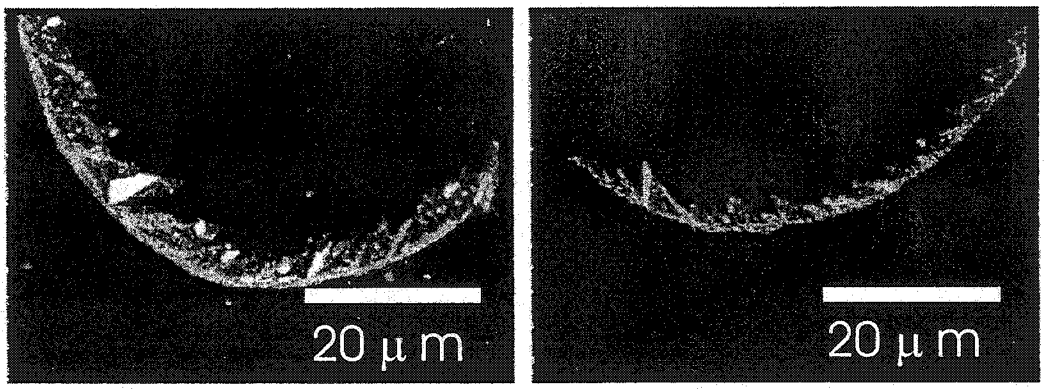

Worn Tool Sharp Tool

Figure 3.21. Chip morphology when finish milling using CBN cutting tools.

3.4.4 Tool Wear Mechanisms in Multi-axis Machining

Irrespective of the tool wear mechanisms, or tool failure mode, uniform wear patterns were observed in straight milling for carbide end mills. This is due to uniform contact of the cutter in the same area throughout the cut. For instance, when milling linear cuts, the depth of cut notch was predominant at the highest cutting speed zone (Elbetawi et.al., 1997). However, when 5-axis milling was performed, variable tool wear patterns were always observed due to the variation of the true chip load and in-cut geometry. In addition, the tilt angle was constantly changing, causing shifting of the contact area of the maximum engagement point.

3.4.5 Modes of Tool Failure in 5-axis Roughing of D2 Tool Steel

Flank wear was found to be the main wear mechanism in roughing. However, the tool failure mode was chipping at the lowest cutting speed zone (101 m/min). As the tool wear progressed to approximately 0.3 mm flank wear, sparks were produced from the worn tool and the cutter was much more susceptible to chattering as the tool exited a corner into a straight cut due to higher chip loads. Chatter was detected through surface roughness observation as well as characteristic chatter noise.

3.4.6 Modes of Tool Failure in 5-axis Finishing of D2 Tool Steel

Nose wear was the main mechanism of tool wear during the finishing process with PCBN. Plastic deformation was observed on the cutting edge as shown in figure 3.22. During the milling of the wall, the tool nose wear progressed to 0.08 mm, which was attributed to the maximum cutting speeds of 1197 m/min. Catastrophic failure, characterized by micro-chipping of the cutting edge, occurred without prior indication of imminent failure. The edge chipping occurred in the cutting speed region of approximately 700 - 1000 m/min and can be correlated to the vibration of the machine/workpiece system.

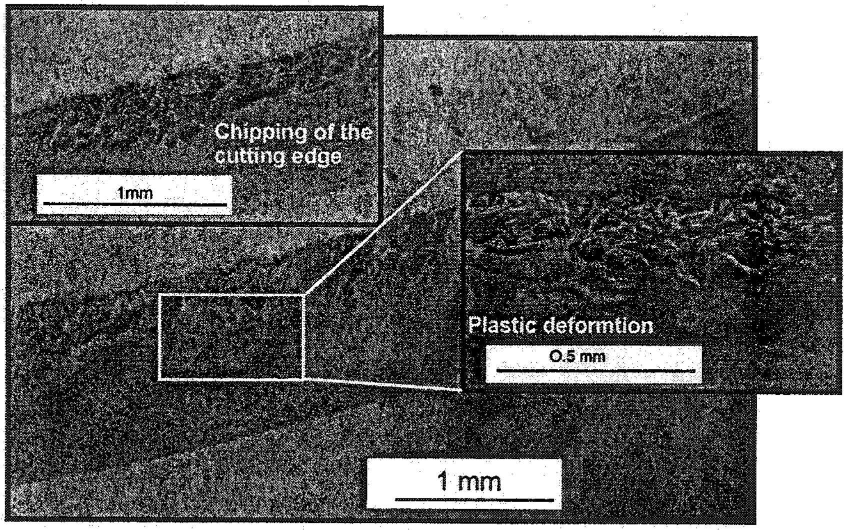

Figure 3.22. Typical tool wear mode during finish machining of AISI D2.

Figure 3.23 shows a comparison of the tool life obtained during the linear and 5-axis milling of D2 tool steel with the same cutting conditions. Comparable tool life was achieved in both roughing and semi-finishing processes. However, tool life was 1.5 longer in 5-axis finishing of D2 tool steel. During linear milling (3 or 4 axis), uniform contact of the cutter in the same area throughout the cut occurs. The contact of the lowest point of engagement always remained in contact with the surface. During 5-axis finishing the tilt angle was constantly varying, changing the contact area of the maximum and minimum points of engagement. Therefore, the load on the cutter was constantly changing positions over the entire length of contact of the tool. This occurred even during the milling of the back wall of the pocket where severe cornering and generally larger axial immersions were required. The premature failure of CBN tools was presumably due to the machine dynamics, specifically, the rigidity of the 4th axis (the tilting axis about the x-direction).

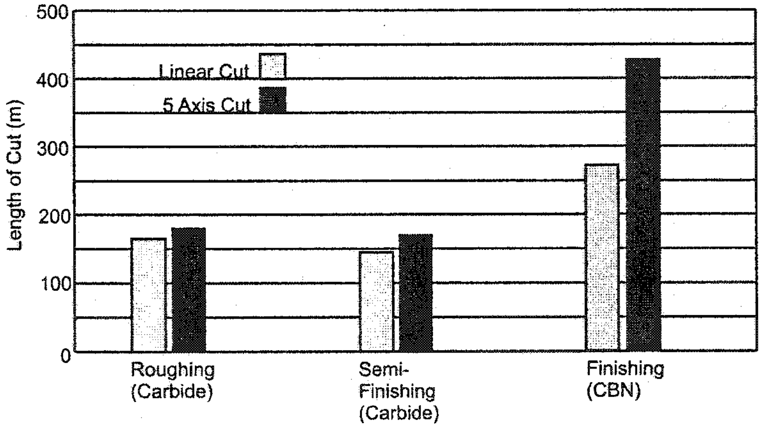

Figure 3.23. Tool life compared to linear cuts when machining AISI D2 tool steel

3.4.7 Forces in 5-axis Milling of D2 tool steel

The high frequency dynamic force component (measured at 675 Hz) present during the milling of D2 tool steel was caused by the hardness of the material. The magnitude of the dynamic component of the cutting forces was almost in the same order as that of the steady state components. In general a stable cutting process was not achieved even after employing a wide range of cutting conditions. This dynamic instability will facilitate the probability of tool chipping and premature catastrophic failure. Figure 3.24 illustrates the large dynamic component in the cutting force signature for finish machining. Another problem encountered during the milling process was the inability of the milling machine to provide the desired feed rate. The feed rate was not maintained when the die topography required large angular rotations of the 4th and 5th axes. The maximum angular velocity of the rotary table was less than that required for maintaining the desired feed rate. This is a potential problem with all milling operations utilizing more than 3-axis. The reduction of the feed rate at the corner is expected to reduce the actual chip load and consequently increase the tool life as shown in figure 3.23.

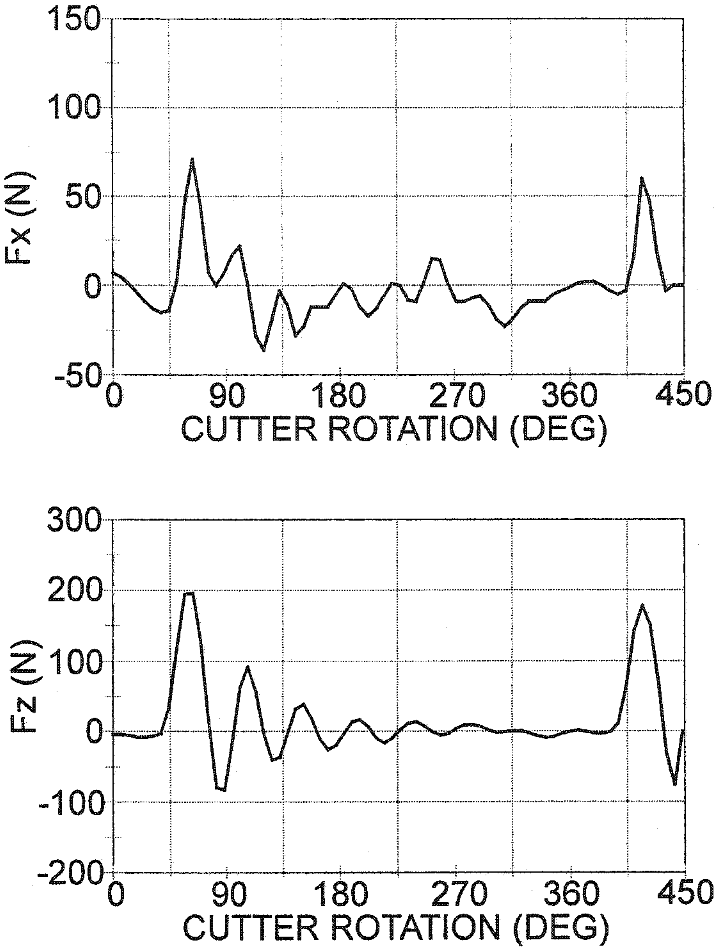

Figure 3.24. Force trace for finish machining D2 illustrating the large dynamic component. (N=10000 rpm, f=0.05 mm/rev, ADC=0.625 mm, RWC=0.254 mm, 10° tilt angle)

3.5 Chapter Summary

The present chapter summarized the experimental work conducted in high speed milling applications for hardened tool steels. The results of the chapter show that high speed milling is a viable technology when applied to H13 at a hardness of 55 HRc. This is, of course, provided that the optimal cutting conditions are used. D2 tool steel at 62 HRc on the other hand, is a much more formidable opponent. The tool life of CBN when cutting D2 is much more sensitive to the cutting conditions and is less forgiving than H13. This is apparent when one considers the tool wear from the presented data.

High speed milling of hardened tool steels may be characterized by the following:

1) When machining hardened steels, a sharp cutting edge is necessary to improve the shearing efficiency of the cutting process to maximize tool life.
2) High speeds are required to thermally soften the material to allow efficient shearing.
3) Tool wear and tool life are strongly dependent on the cutting conditions, especially when machining D2 at 62 HRc.
4) Segmented saw-toothed type chips are formed causing high temperatures as well as high stresses on the cutting edge.
5) Effective die machining can be accomplished using continuously varying 5 axis motion to prevent constant force on the same region of the cutting edge.

6) Machining dynamics proves to be a very important issue when milling hardened materials. Classical methods, which are used to provide process damping to reduce cutting induced vibrations, will not work with hardened tool steels. Techniques such as honed edges may damp out vibrations but severely decrease tool life due to material effects.

It is evident from the present research that effort must be focused on the mechanics of the cutting process incorporating the metallurgical properties of the alloy in question. The following chapters are dedicated to this task.

Chapter 4

Flow Stress Characterization of AISI D2

4.1 Introduction

Chapter 3 illustrated the difficulty associated with the machining of hardened AISI D2 tool steel. It was shown that the tool life (in contrast to hardened H13) was extremely short due to the mechanical properties of the alloy and the machining dynamics. The chapter concluded that it is necessary to understand the mechanical behaviour of the alloy. It is the objective of the research to develop a force model, which utilizes material properties in the form of flow stress during the chip formation process.

Issues regarding chip formation mechanics and mechanisms (Elbestawi et.al, 1996, Elwardany et.al., 2000 (Part I), Elwardany et.al., 2000 (part II)), chip morphology , (Elwardany et.al., 2000 (Part I)) surface integrity and residual stress calculations (Elwardany et.al., 2000 (Part II)) have been steadily explored with considerable success. Analytic force modelling on the other hand has largely been left to empirical approaches using existing force data to calibrate for the stress levels. The reason for this limitation is a lack of data and models describing the material behaviour given the high strain rates and large strains associated with chip formation. Strain rates encountered in machining are of the order of (10^3-10^6 s^{-1})(Shaw, 1984) and strains well in excess of unity are the norm rather than the exception. The quantification of the material flow stress behavior in this regime has proven difficult because standard quasi-static (low strain rate) material tests do not attain such conditions. It should be clearly understood that the flow stress of materials varies substantially from quasi-static tests to high strain rate conditions. Elevated strain rates can also lead to different failure mechanisms. For instance, adiabatic shear localization can occur at higher strain rates, and is rather frequently encountered in machining hardened steels (Bai and Dodd, 1992).

Any fundamental analytic force model should require knowledge of the flow stress of the material at elevated strains and strain rates combined with the high temperatures encountered during machining. Metallurgical changes such as phase transformations, impurities and strengthening phases in the material also add difficulty in the quantification of the flow stress. As a result, a range of constitutive laws defining the flow stress of materials has been used in predictive FEA force modeling applications as reviewed by Childs (Childs, 1998).

Many approaches have been proposed for quantifying the high strain rate behaviour of materials at elevated strains and temperatures. Some investigators attempt to derive and quantify constitutive laws from turning processes (Lei et.al., 1997). The difficulty with these methods results in an imprecise determination of deformation temperatures, friction conditions on the tool face as well as precise quantification of strains, which may cause variations in the flow stress applicable only to the cutting conditions, encountered during the tests. The strains must be determined post deformation by analysis of the chips. As such, the precise strain history is difficult to determine strictly from metallography or a kinematic representation of the chip formation process. More fundamentally, the loading path during machining (the strain and strain rate history) is not well understood. Any precise stress-strain relation must map the exact deformation conditions with the loading conditions so that a true correlation can be made. Any small deviation in conditions will jeopardize the validity of the flow stress if the cutting conditions change.

Other methods exist which are dedicated to measuring the flow stress behavior of materials at elevated strain rates in which precise determination of temperature and strain rates are attained. These methods include ballistic impact testing as well as the Compressive Split Hopkinson Bar tests (CSHB). The merits of the CSHB in uniaxial compression arise from the ability to precisely measure the strains, strain rates and temperatures during loading and unloading of the specimen. Merits of the torsional SHB have been proposed in (Saunders and Nutting, 1984), however the extent of strain is small and the strain rates are much less than 10^4 s^{-1}. For certain configurations, the strain rates that can be obtained from CSHB tests (10^3-10^4 s^{-1}) approach that of machining. To extend the CSHB apparatus to consider large shear strains and strain rates, a punching shear sample configuration has been proposed (Andrade et.al., 1994, Mason et.al., 1997). For this configuration, strain rates in excess of 10^4 s^{-1} and strains larger than unity can be readily achieved. Data collected at high strain rates from CSHB tests were used in modelling machining processes with good results (Jaspers, 1999).

Hardened tool steels are classified as difficult to cut due to their extreme hardness and resistance to flow. AISI D2 is a cold work die steel commonly used in the die and mold industry. This material has been the focus of several investigations involving chip formation and morphology, cutting force analysis, and tool wear (Boehner et.al., 1999, Boehner et.al., 1999, Becze et.al., 2000). Characterization of cutting forces will provide significant insight on the machinability characteristics. In order to model forces in machining D2, knowledge of the flow stress is required in the "as machined" state. There is no data expressing the high strain rate, high temperature flow properties of this material under maximum hardness conditions. Thus, the present research focuses on characterization of the flow stress and deformation behavior of AISI D2 for use in machining simulations.

The extreme hardness of the material limits the availability of applicable test techniques to determine the flow stress at elevated strain rates. The Compressive Split Hopkinson Bar technique in the punching shear configuration was chosen due to the ability to achieve high strain rates, as well as the robustness of the test apparatus. In conjunction to the high strain rates, the temperature dependence of the flow stress was also determined. The tests permitted constitutive representations of the flow stress in the form of empirically based (Johnson-Cook) and physically based (Zerilli-Armstrong) constitutive laws as functions of the large strains, high strain rates, and temperature. The sheared specimens were used to characterize the failure modes as a function of loading rate and temperature. Elevated strain rates and high temperatures generally cause deformed or transformed shear banding. The presented work provides qualitative observations of the deformation structure of the shear bands and on the fractured surfaces, under various test conditions as well as quantitative results relating the flow stress of the material to the large strain, high strain rate and high temperature dependence.

High strain rate mechanical testing on fully hardened AISI D2 tool steel (at 62 HRc) was performed utilizing the Compressive Split Hopkinson Bar technique (CSHB) incorporating a punching shear strain state. The high strain rate conditions were comparable to those encountered in machining processes, with shear strain rates on the order of 5×10^4 s^{-1} and shear strains in excess of unity (100% mm/mm). The tests were performed at various initial temperatures ranging from 296-873 K to investigate the flow stress behaviour of the hardened tool steel as a function of temperature. The high strain rate experimental shear stress-strain data was used to fit the flow stress by; i) an empirically based constitutive law in the form proposed by Johnson and Cook; as well as, (ii) a physically based constitutive law proposed by Zerilli and Armstrong which accounts for strain, strain rate, and temperature dependence of flow stress. The data incorporated the adiabatic temperature rise in the shear zone and was used in the constitutive law modelling. The deformed microstructure was investigated using optical and scanning electron microscopy to determine the extent of the shear localization zone and the final fracture mode.

4.2 Principles of the Compressive Split Hopkinson Bar Test

Figure 4.1 is a basic illustration of the compressive split Hopkinson pressure bar apparatus. The test rig consists of a striker bar which is fired by some means (usually compressed air) at very high velocities. The velocities are chosen such that the pressure wave transmitted into the incident bar is still elastic. The striker bar then hits the incident bar establishing an elastic pressure wave to propagate down the incident bar. Strain gauges are used to measure the strain of the elastic wave and store the "incident" pulse. Let ρ_b be the density of the pressure bars, and E_b the Young's modulus, then the elastic wave velocity C_e in the bars can be written as equation 4.1:

$$C_e = \sqrt{\frac{E_b}{\rho_b}} \quad \mathbf{4.1}$$

This compressive pulse is partly transmitted across the incident bar interface to the specimen and partly reflected into the pressure bar as a tensile wave. While propagating in the specimen, the pressure wave plastically deforms the specimen, where as part of the wave is reflected back through the incident bar. At the specimen transmitter bar interface, a part of the remaining stress wave is transmitted and a part is reflected into the specimen. Due to reverberations of the plastic wave in the specimen and because the initial stress wave length is chosen to be much larger than the specimen length, a situation is reached at which the specimen deforms in a uniform state of stress.

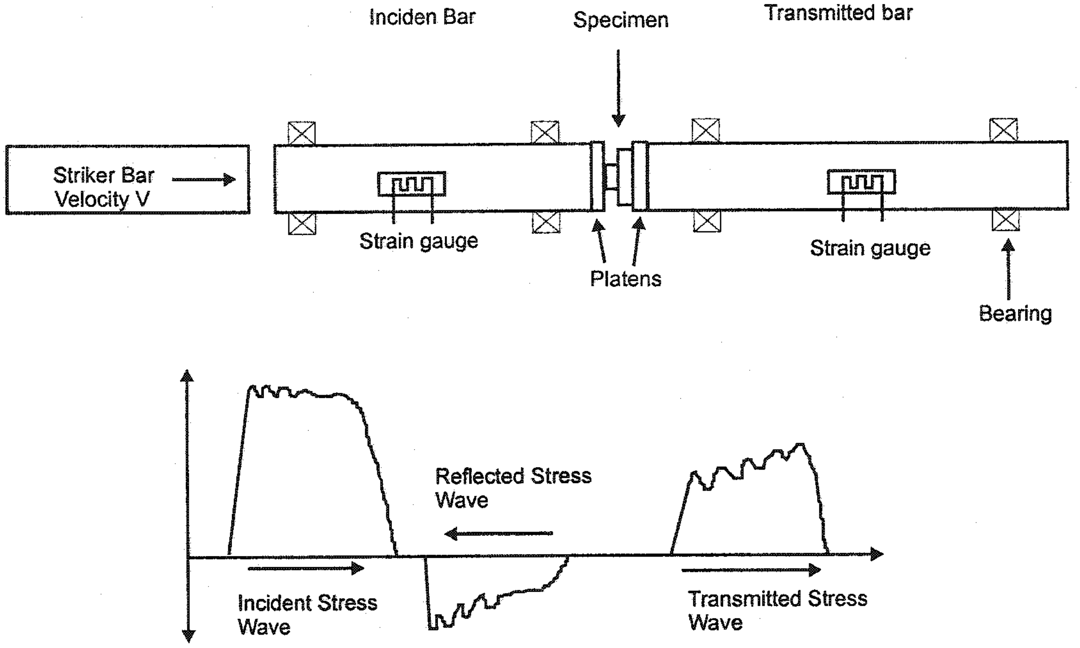

Figure 4.1. A schematic representation of the Compressive Split Hopkinson Bar Apparatus.

The time varying strain (ε (t)) in equation 4.2 and time varying stress (σ(t)) in equation 4.3 for the specimen may be calculated by using one-dimensional elastic wave propagation theory for stress waves:

$$\varepsilon(t) = \frac{C_e}{L}\int_0^t \{\varepsilon_i(t) - \varepsilon_r(t) - \varepsilon_t(t)\}dt \qquad 4.2$$

$$\sigma(t) = \frac{E_b A_b}{2A}\left[\varepsilon_i(t) + \varepsilon_r(t) + \varepsilon_t(t)\right] \qquad 4.3$$

where, t is time, εi is the measured incident strain of the stress wave, εr is the strain of the reflected stress wave, εt is the transmitted stress wave strain, Eb and Ab are the Young's modulus and area of the pressure bars, where as L and A are the instantaneous length and area of the specimen.

4.3 Experimental Testing and Procedures

Meyer has proposed a geometry for large strain CSHB testing. The geometry was modified to accommodate the high stresses involved with the testing of D2 tool steel. Figure 4.2 illustrates the geometry of the specimen used for the present work. 60 D2 tool steel specimens were machined to the required geometry of high strain rate Compressive Split Hopkinson Pressure Bar tests (CSHB) configured for punching shear type tests (figure 4.2). The tolerances were kept extremely tight (± 12 μm) to reduce the error in predicted stress values. The specimens were then heat treated to 62 ±1 HRc. Following heat treatment, the impact surfaces were then precision ground to ensure flatness. As a further precaution, the samples were measured and grouped so that the tests were repeated under the same geometric conditions.

During testing, the specimen is compressed such that the solid cylinder region is driven into the hollow cylindrical region generating a region of intense shear (region δ) illustrated in figure 4.2. The CSHB test condition results in an imposed velocity difference between the incident and reflected bars of 6.35 m/s over the specimen length. Given a gauge length dimension of 0.127 mm, the computed nominal strain rate becomes 50000 s^{-1}. Further description of the CSHB punching shear technique is given in (Mason et.al., 1997, Mason and Worswick, 2000). The specimen design of Figure 1 was precision machined from the same stock and all tolerances were kept to ±0.025 mm.

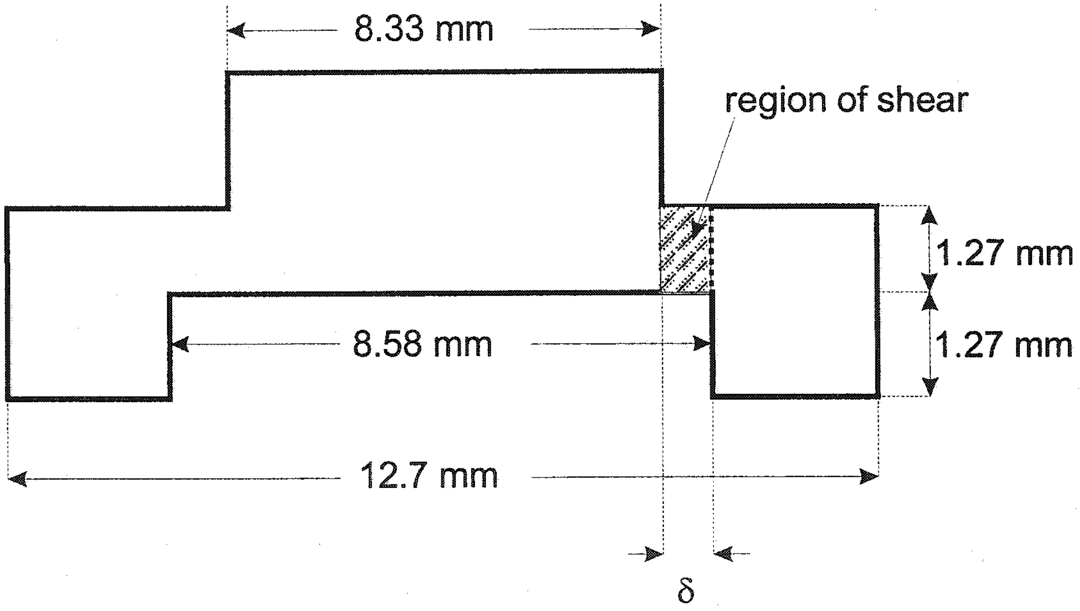

δ is shear band gauge length (=0.127 mm)

Figure 4.2. Modified high strain rate monolithic specimen cross section for use in CSHB tests on fully hardened AISI D2 tool steel (62 HRc).

The CSHB apparatus includes 12.7 mm diameter striker, incident and reflected bars made of O1 tool steel. The striker bar length of 305 mm was selected to ensure adequate energy transfer to the specimen, as shorter striker bars did not deliver adequate energy transfer to deform the specimen at low temperatures. The incident and reflected bars used were 711 mm in length.

Due to the extreme hardness of the test specimens, hardened AISI O1 tool steel platens were used to protect the Hopkinson bar interfaces, and to prevent extraneous stresses due to specimen indentation. The platens were at least 5 HRc harder than the specimen. Alignment fixtures were used to ensure consistent alignment of the test specimens with the CSHB bars interfaces and the platens.

A quartz lamp/furnace was used to heat the specimens to the desired temperatures (up to 600 ^{o}C). A thermocouple was spot welded to the outer diameter region of the specimen to monitor and control the temperature for all tests. Each specimen was allowed to equilibrate at the desired temperature for 30 seconds, which ensured uniform temperature distributions throughout the cross section. The incident and reflected bars were isolated from the heating lamps by use of a protective aluminium shroud exposing only the specimen to the thermal source. To further minimize possible thermal errors affecting the wave propagation characteristics of the incident and transmitter bars, brass bushings, acting as effective heat sinks, were placed 30 mm away from the specimen. The testing considered variation of temperatures and strain rates to obtain data for the thermal dependence of the constitutive law. Table 1 outlines the test parameters used in the present investigation.

Table 1. Test parameter variations.

Parameter	**Value**
Initial Temperature (K)	294, 373, 473, 573, 673, 773, 873
Strain Rates (s^{-1})	10^3 - 10^4

The data was collected using a high frequency Nicolet Pro30 digital storage oscilloscope with 12-bit resolution. The sampling rate was set at 10 MHz (i.e. a 0.1 μs time differential per data point). The output of the tests was processed using the University of Waterloo's software to obtain strain rate vs. time and stress vs. strain curves. For each test it was observed that the strain rate varied less than 5000 s^{-1} while the material was deforming under steady state conditions, up until failure occurred in the specimen and the strain rate decreased rapidly. Wave reflections in the specimen caused variations in the strain rate up to a strain level of 0.1 m/m. The coefficients for the Johnson-Cook and Zerilli-Armstrong constitutive laws were then determined from the stress vs. plastic strain, instantaneous strain rate, and instantaneous temperature values using a multidimensional-multivariable non-linear regression technique.

After the tests were performed, the specimens were sectioned and mounted in a metallurgical cold mount, polished and etched to reveal the deformed microstructure of the shear cross section. Scanning electron microscope (SEM) analysis was used on the sheared interfaces to observe the structure of the fractured surfaces.

4.4 Results and Discussion of High Strain Rate Tests

4.4.1 Punching Shear Results

The output of the compressive split Hopkinson bar test did not directly provide the required stress-strain data. The signal came in the form of voltages supplied by the strain gauges. This signal first had to be assessed to ensure the validity of the tests. A clean signal with minimal reflection was the main criteria as a valid representation of the flow stress. Due to the extreme hardness of the alloy, as well as the very large flow stresses associated with the deformation of the specimen, some reflections were observed and are an inherent difficulty associated with the testing. Reflected pulses after deformation, are permissible, but the data was not used after deformation has occurred. Figures 4.3 and 4.4 illustrate typical signals used for the deformation analysis. Figure 4.3 shows an impact signal on the transmitted pulse at 260 μs which occurred in several tests. This was shown to be the impact of the specimen *after* shearing on the transmitter bar interface. These types of signals were not used in the data. The data was then processed using equations 4.2 and 4.3 to provide the raw data for the analysis.

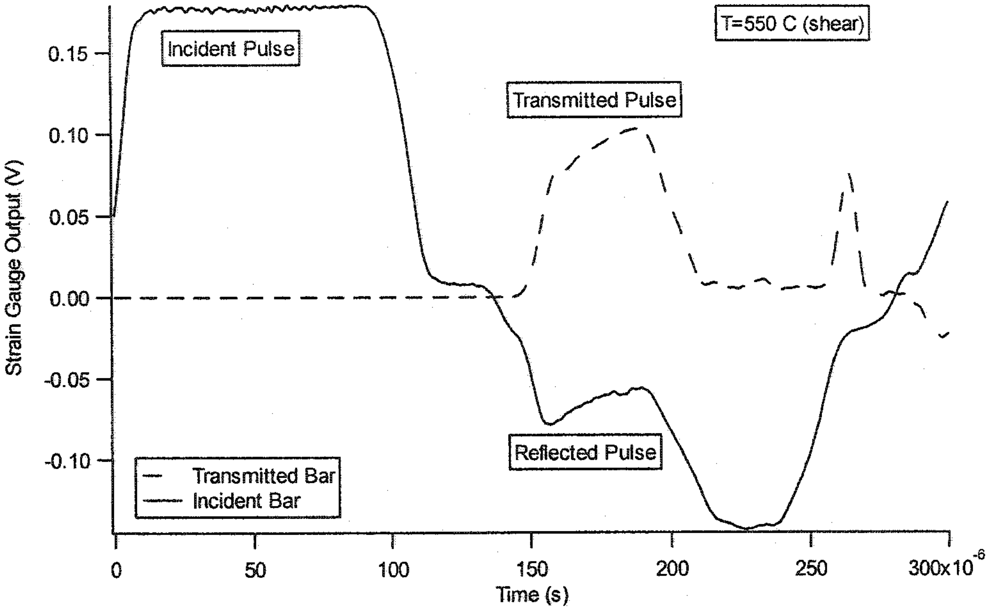

Figure 4.3. Typical output for the Compressive Split Hopkinson Bar in Shear configuration.

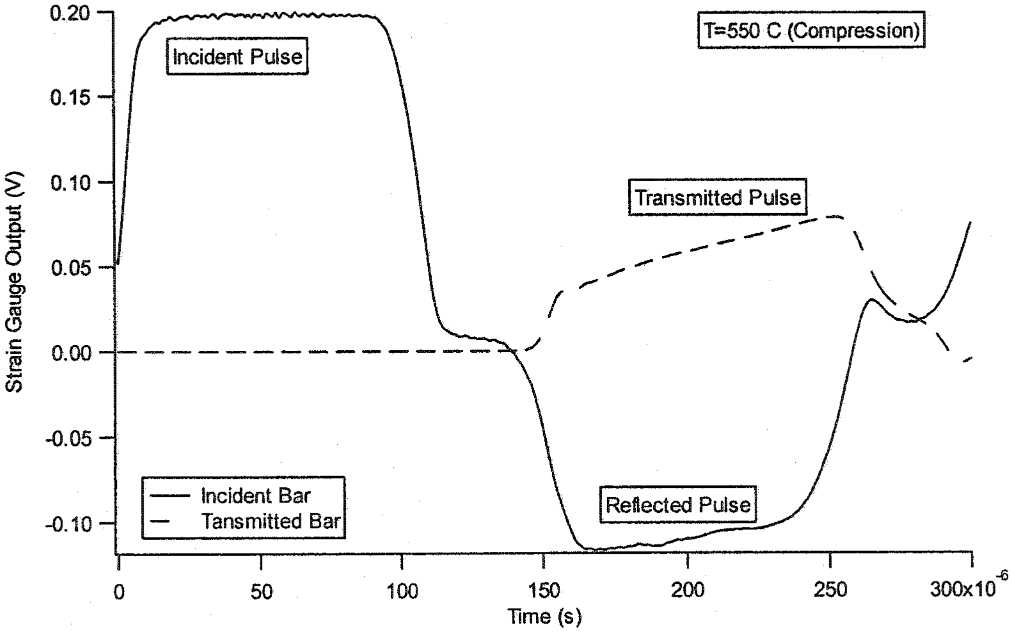

Figure 4.4. Typical output for the Compressive Split Hopkinson Bar in Compression Configuration.

A further stipulation was added to the data to ensure the validity of the results; the strain rate must remain relatively constant over the strains tested. This is ensured that equilibrium was established through the entire deformation process. It was found experimentally that strains beyond 5% were in complete equilibrium for all conditions tested and is illustrated figure 4.5. The limitation placed on the flow stress for strains below 5% is of no consequence in the present investigation. Machining induces strain well in excess of unity. Thus, small strain deformation is of little consequence during machining. Further, the continuous nature of plastic flow of the constitutive laws used will also ensure that reasonable stress levels are predicted in the modelling.

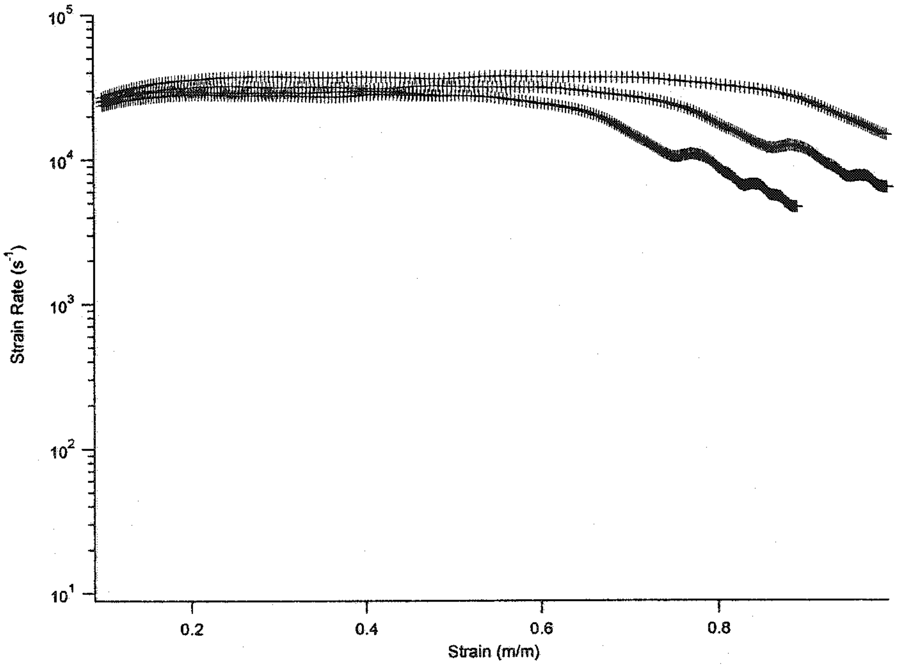

Figure 4.5. Strain rate variations for the CSHB shear configuration at ambient temperature (23^0 C). The cut off strain used for this test was 0.6 (m/m).

The stress-strain data from the CSHB punching shear tests was processed to generate a multidimensional array, which quantified the instantaneous stress, strain, and strain rate associated with the deformation process for each given strain increment during the test. Since the stored stress-strain data contained the elastic portion of deformation as well as the plastic portion, the elastic portion of the strains was removed from the total measured strains according to:

$$\gamma_p = \gamma_T - \frac{\tau_i}{G(T)} \qquad 4.4$$

where γ_p is the plastic shear strain increment, γ_T is the total measured shear strain, τ_i is the shear stress level at the total plastic strain increment and G(T) is the temperature dependent shear modulus.

Strains in excess of unity were consistently achieved. This implied that significant thermal energy was added to the deforming shear zone due to mechanical work. In order to model the actual instantaneous temperature, the thermal energy was calculated by assuming all plastic work was converted into thermal energy. The temperature at each state was estimated from the portion of plastic work converted into heat by:

$$T(i) = T_o + \Delta T = T_o + \frac{\beta}{\rho Cp}\int_0^{\gamma} \tau d\gamma \qquad 4.5$$

where T(i) is the temperature associated with shear deformation, T_o is the initial test temperature, ρ is the density (7750 Kg/m^3), and Cp is the specific heat capacity (485 J/Kg K). β is the fraction of plastic work converted into heat (Bai and Dodd, 1992). It has been stated that β can vary from 0.7 for annealed un-worked materials, and increases to near unity for wrought materials. In the present work, β was chosen to be 0.9, although independent measurements of temperature were not available. Values of temperature were calculated for each measured stress, strain, and strain rate increment in the regression fits of the constitutive parameters. In all experiments, the temperature rise associated with deformation proved significant, as increases of 120-150 ^oC were predicted for strain values of 1. For strains over 100%, the specimens localized in shear as demonstrated by a rapid reduction in the nominal flow stress.

Figure 4.6 illustrates typical experimental stress-strain curves obtained from the high strain rate tests. The results indicate that an increase in ductility occurred with increasing temperature with shear localization occurring at higher temperatures. It should be noted that the analysis only considered strains greater than 0.1 because the sample was not in stress state equilibrium prior to this time due to rise time limitations. The rise time of the stress levels are affected by reflections from the specimen interfaces due to the geometry as well as acoustic impedance variations caused by non-uniformity of temperature in the bar. It was observed that the stress-strain signal reached equilibrium after shear strains of 0.1 m/m for all tests performed. After 473 K, the specimen failed at strains greater than unity showing the effect of temperature on the ductility of the specimen except for temperatures greater than 773 K. At 773 K, shear localization occurred at a strain value of 0.8. The shear strength at failure was measured at 1500 MPa (~3000 MPa effective stress). Considerable work hardening was observed in the high strain rate as well as the lower strain rate tests over the entire strain range tested.

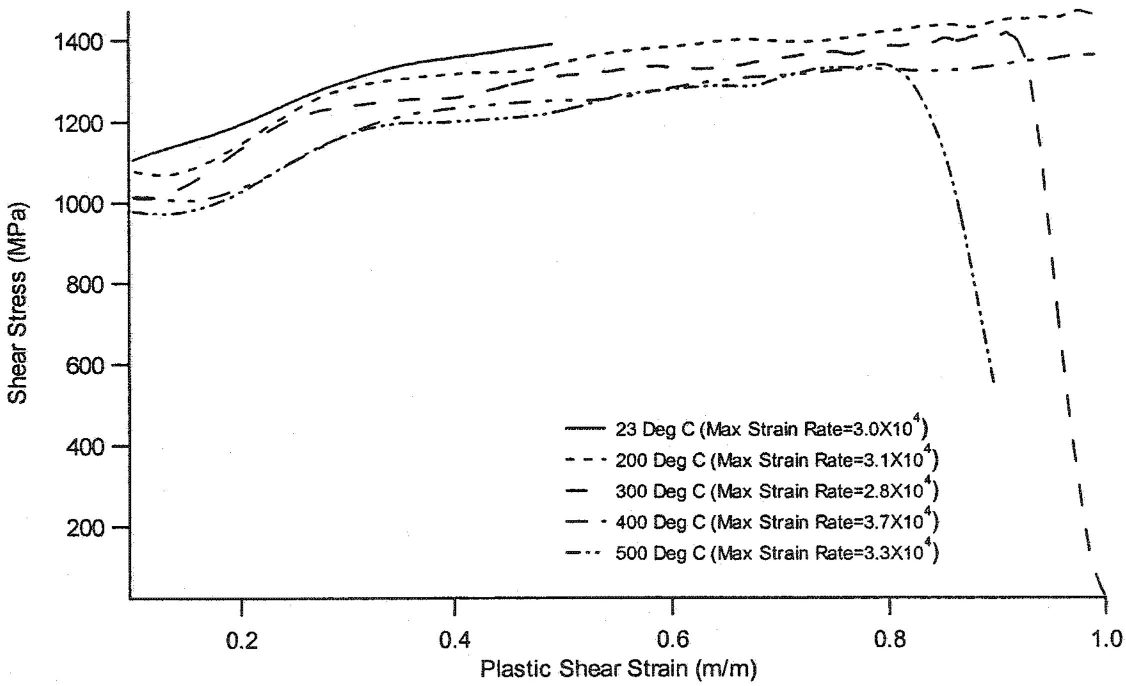

Figure 4.6. Experimental shear stress-plastic strain curves illustrating increasing ductility and reduction of flow stress as a function of initial test temperature.

The stress-strain curves (figure 4.6) illustrate a limited temperature sensitivity up to 773 K. Very little evidence of a reduction of flow stress with increasing temperature effects in the range considered was observed, indicating metallurgical stability and resistance to thermal softening (Figure 4.7). Generally, the flow stress of a material will decrease with increasing temperature until the melting point of the material is reached where the material strength essentially vanishes. However, this functional dependence is often not a simple monotonically varying function. It has been reported that some ferrous and non-ferrous alloys exhibit a flow stress plateau with increasing temperature (Bai and Dodd, 1992).

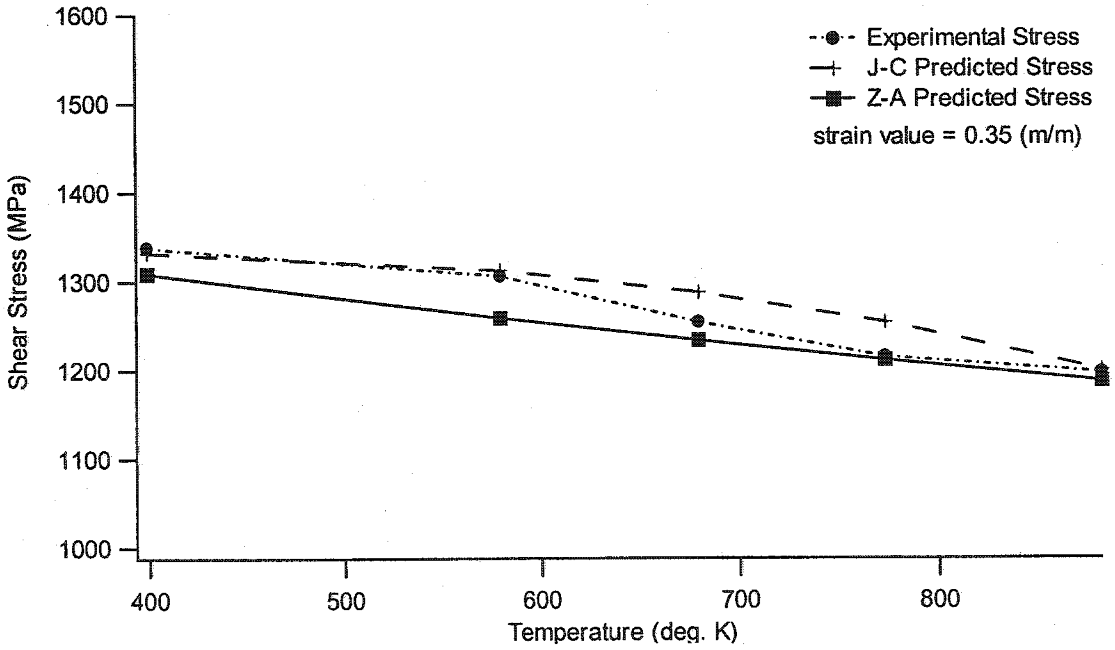

Figure 4.7. Variation of experimental and predicted flow stress with adjusted adiabatic temperature at constant strain value of 0.35.

Plastic slip in metals is governed by dislocation motion. The ease with which a dislocation propagates through the crystal matrix determines the magnitude of the flow stress. Secondary phase particles act to strengthen the material by creating local obstacles, which pin or impede the dislocation motion through dislocation forests or particle interaction mechanisms. D2 tool steel in its maximum hardened state contains large percentages of high temperature alloy carbides (such as chromium and vanadium carbides) giving the material its wear resistance and strength. The strengthening of the alloy at low temperatures is obtained from the martensitic structure in which massive chromium carbides as well as relatively smaller spheroidal alloy carbides are dispersed. The material insensitivity to thermal softening for the temperature range considered in the present investigation is attributed to the thermal stability of the alloy carbides. The alloy carbides are relatively insensitive to thermal softening effects for the temperature range investigated. Since the carbides are stable at higher temperatures, they still act as effective dislocation obstacles, which increase the Orowan stress of the material. Thus, at the higher test temperatures, the limited reduction in the flow stress is primarily due to thermal softening of the matrix. Thermal softening of the matrix may be due to de-tempering effects, as temperature has a marginal effect on the tempered hardness of the alloy, which in turn limits the flow stress. Strong materials generally require thermal energy greater than half the melting temperature on the absolute scale to activate dislocation motion (Kelly and MacMillan, 1986). Since the microstructure of AISI D2 has a large volume fraction of high temperature alloy carbides, the flow stress is not expected to be a strong function of temperature below 0.5 Tm (where Tm =1763 K) of the alloy.

Compression CSHB tests were also performed on D2 tool steel using cylindrical specimen geometry. In these experiments, a marginal increase in ductility was observed for strain rates of 3500 s^{-1} with increasing temperature. The failure mode of the specimens was predominantly by gross fracture up to and including the tests performed at 773 K. At an initial test temperature of 873 K, the specimen plastically deformed with no evidence of fracture. This is consistent with the shear tests where it was also observed that the ductility increased with increasing temperature, as expected, considering that the initial test temperature of 873 K is approximately 0.5 Tm where dislocations are more mobile.

4.4.2 Constitutive Parameter Determination

Quantification of the stress-strain behavior for materials is generally expressed in the form of a constitutive law that may be used in numerical simulations. Stress-strain constitutive laws are designed to represent the flow stress of the material as a function of strain, strain rate, and temperature. The forms of the constitutive laws are derived from either empirical formulations, which generally fit certain material behavior (Johnson and

Cook, 1983), or from a dislocation mechanics approach where the micromechanics and thermodynamics of material slip is considered (Zerilli and Armstrong, 1987).

In the present analysis, the stress, strain, strain rate, and temperature data was used to fit two constitutive law forms, the Johnson-Cook (Johnson and Cook, 1983) and Zerilli-Armstrong (Zerilli and Armstrong, 1987). Johnson and Cook developed an empirically based constitutive law for relating the stress, strain, strain rate, and temperature behavior of materials. The equation possesses the form:

$$\sigma = (A + B\varepsilon^{n})(1 + C\log(\frac{\dot{\varepsilon}}{\dot{\varepsilon}_{o}})(1 - \{\frac{T-293}{T_{m}-293}\}^{m}) \qquad (1)$$

where A, B, C, n, m, are material constants, σ is the flow stress of the material, ε is the strain, $\varepsilon^{\bullet}$ is the strain rate, $\varepsilon^{\bullet}_{o}$ is the reference strain rate used (3500 s^{-1}), T the measured temperature (in ^{o}K), and T_m the melting temperature of the alloy (1763 K).

The Johnson-Cook empirical constitutive law was fitted to the entire data set. The results of the non-linear regression are summarized in Table 2. The entire data set consisting of stress, strain, strain rate, and calculated temperature, including adiabatic effects, (Equation 2) was used to determine the coefficients of the Johnson-Cook equation. It is interesting to note that the adiabatic temperature rise indicated considerable heating of the shear band in the specimen due to the large flow stresses required for plastic flow. It is expected, due to the form of the constitutive law, that the large temperature rise in the shear band will lower the flow stress of the material. Due to the limited reduction in the material flow stress, a large thermal softening exponent was computed, limiting the effect of the adiabatic temperature rise in the shear zone.

Table 2. Comparison of material constants for hardened tool steels.

Johnson-Cook Material Constants	**D2 Tool Steel (HRc 62)**	**S7 Tool Steel (HRc 50)**
A (MPa)	1020	883
B (MPa)	522.36	248
C	.012	.012
n	.312	.18
m	3.38	1 (Assumed)

Johnson *et al.* performed mechanical tests on various limited ductility metals and provided the constitutive law constants for S7 tool steel (a shock resistant tool steel) at hardness of HRc 50. The mechanical tests on brittle materials provides a strain hardening exponent (n) in the range of 0.18 – 0.2 (Johnson et al., 1983 (b)). The present analysis yields a strain hardening exponent of 0.312, indicating a higher work hardening potential of the alloy. The large volume fraction of secondary phase particles causes a large number of dislocation pinning sites, which decrease the mobility of the dislocations. The dislocation forest and entanglement are presumed responsible for the relatively large work hardening parameter by impeding dislocation slip.

The thermal variation of the flow stress as discussed in (Johnson et al., 1983 (b)) was not measured. It was assumed the homologous temperature exponent (m) varied in a linear fashion (m=1). In contrast, the present work obtained a high value for m (3.38). This implies that alloy under the given high strain rate conditions is insensitive to marginal temperature increases. The relative insensitivity (a large m value) of the flow stress illustrates the importance of the microstructure and metallurgy on the thermal properties of the material.

Table 2 presents both the values obtained by Johnson *et al.* (Johnson et al., 1983 (b)) for torsional shear tests of brittle materials and the values calculated in the present work. Comparison of the constants illustrates that the materials are of similar yield strength (coefficient A). Although, the strain hardening and presumably the thermal softening dependence are different, the strain rate sensitivity is identical for both materials and is of similar magnitude for all less ductile materials presented in (Johnson et al., 1983 (b)).

Figure 4.8 illustrates the predicted stress-strain relations using the Johnson-Cook constitutive law for the experimental data. The constitutive law provided a good fit to the trends observed from the experimental results. The maximum error of the predicted stress with respect to the experimental stress was ± 40 MPa (± 8%) where the majority of the error arose from the stress plateau (presumably due to non-equilibrium effects in the apparatus) at low strains. The constitutive law provided a good representation of the flow stress for larger strains.

The Johnson-Cook constitutive law is an empirically based constitutive law and its relatively simple form has been scrutinized extensively. Thus, a second form of constitutive law was fitted to the experimental data, which is based on physics of dislocation motion. Zerilli and Armstrong developed a constitutive law for BCC and FCC structures. Since D2 is a martensitic structure, the form appropriate for BCC crystals of the constitutive law is:

(2)

$$\sigma = C_0 + C_1 \exp(-C_2 T + C_3 T \ln \dot{\varepsilon}) + C_4 \varepsilon^n$$

where C_i are material related constants, T the absolute temperature, ε the strain and $\varepsilon^{\bullet}$ the strain rate.

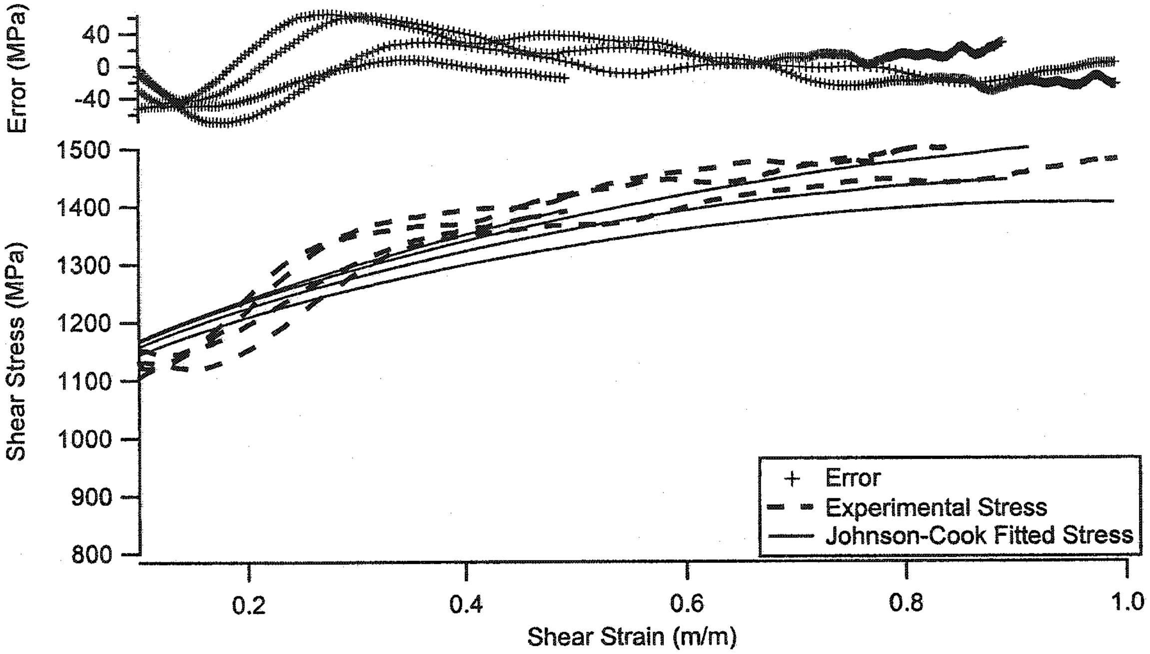

Figure 4.8. Johnson Cook constitutive law representation of experimental flow stress conditions.

The Zerilli-Armstrong formulation was developed for relatively simple materials where dislocation slip in various crystal structures was considered. Dispersion strengthened materials such as D2 tool steel contain large volume fractions of alloy carbides which impede dislocation motion. Since the formulation considers slip based on dislocation physics, it is expected that the constitutive law will describe the flow stress as adequately as the Johnson-Cook formulation.

The same algorithm was used for the Zerilli-Armstrong coefficient minimization as the Johnson Cook. The coefficients for the Zerilli-Armstrong equation are presented in Table 3, and the predicted stress levels are illustrated in figure 4.9. Both constitutive forms (Zerilli-Armstrong and Johnson-Cook) provided excellent prediction of flow stress over the range of conditions tested. It can be seen in figure 4.7 that both constitutive law forms capture the thermal dependence of the material relatively well. The Johnson-Cook constitutive law over estimates the flow stress for higher temperatures, but provides a good estimate for the low temperatures. On the other hand, the Zerilli-Armstrong constitutive law yields a more accurate estimate for the higher temperature range and is less accurate for low temperatures. The error associated with each constitutive form does not deviate from the experimental data by more than 5%.

Table 3. Coefficients of the Zerilli-Armstrong Constitutive Law.

Coefficients for equation 4	**Value**
C0	148 (MPa)
C1	560 (MPa)
C2	.000528
C3	1.21E-5
C4	1007 (MPa)
N	0.298

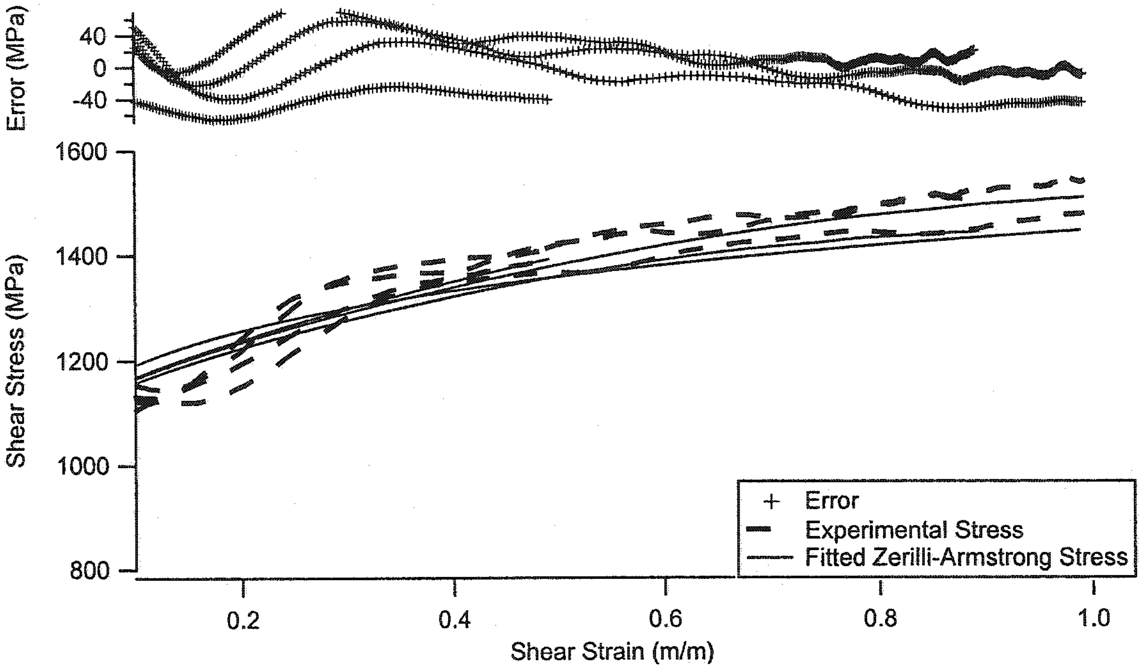

Figure 4.9. Zerilli-Armstrong Representation of shear stress using experimental data.

4.4.3 Localization Analysis

The morphology of the specimens indicated that transformed shear bands possibly occurred as a result of adiabatic shear localization. The so-called maximum shear stress criterion assumes that adiabatic shear instability occurs when an increment in strain causes a reduction in flow stress (Bai and Dodd, 1992). If the flow stress in shear (τ) is considered to be a function of strain (γ), strain rate ($\gamma^{\bullet}$), and temperature (T), catastrophic shear localization is imminent when the slope of the stress-strain curve is zero:

$$0=\frac{d\tau}{d\gamma}=\left.\frac{\partial\tau}{\partial\gamma}\right|_{T,\dot{\gamma}}+\left.\frac{\partial\tau}{\partial\dot{\gamma}}\right|_{T,\gamma}\frac{d\dot{\gamma}}{d\gamma}+\left.\frac{\partial\tau}{\partial T}\right|_{\gamma,\dot{\gamma}}\frac{dT}{d\gamma} \qquad (3)$$

At the high rates of strain under consideration, heat conduction is negligible and the deformation is adiabatic, thus $\frac{dT}{d\gamma}=\frac{\beta\tau}{\rho C_p}$. If the constitutive law is known as in equations 3 and 4, then the critical strain for instability can be computed. The expression using the Johnson-Cook constitutive law and the coefficients from the previous section are used to numerically solve for the critical instability strain. The assumption was made that the effect of strain rate on flow stress is negligibly small because the strain rates in the present investigation (~4.5 X 10^4 s^{-1}) are greater than 10^2 s^{-1} (Staker, 1981) which is consistent with the analysis presented in by Johnson et al. (Johnson et al., 1983 (b)).

Adiabatic shear was observed for several specimens at high strain rates. The critical strain for localization was found experimentally. The critical strain varied from 0.8 at 773 K to a value greater than unity for lower temperatures. The localization strain was taken as the strain for which the slope of the experimental stress-strain curve became negative. The critical instability strain was calculated as 0.328, for an initial test temperature of 773 K by using equations 3 and 5 and solving numerically. Clearly, the calculated instability strain using the constitutive form of equation 3 was less than that observed from the experimental data. The reason for this is the method outlined for computing the instability strain relies on thermal softening as the primary mechanism for instability (Bai and Dodd, 1992). The deviation in critical strain may arise from other mechanisms, which may affect the flow stress of the material such as solute strengthening, for which equation (5) does not consider. Further, after 773 K adiabatic heating may cause the material to achieve temperatures above 0.5 Tm (~ 830 K) of the alloy. The increase in temperature will generally cause an increase in ductility suppressing shear localization leading to a higher critical instability strain. Adiabatic shear localization may occur in ballistics, in machining, and in any high strain rate deformation process and is considered a very complicated phenomenon. Volumes of material have been written to predict, understand, and explain the occurrence of adiabatic shear localization. However, prediction of failure mechanisms based solely on constitutive laws, such as the Zerilli-Armstrong because of the physical based formulation may lead to erroneous results. Constitutive laws such as the Zerilli-Armstrong neglects to account for damage induced by secondary phase particles.

4.4.4 Metallographic Analysis

Metallographic sections were prepared to observe the deformed microstructure of the high strain rate shear specimens and are shown in figures 4.10 to 4.13. The specimens exhibit a highly deformed microstructure in the vicinity of the shear zone. Shear banding was observed in all specimens. Two basic types of shear bands have been reported to occur in elevated strain rate testing: deformed shear bands and transformed shear bands. Deformed shear bands occur generally when the temperatures of deformation are below the martensitic transformation temperatures. Transformed shear bands occur when the local temperature rise is enough to cause a phase transformation in the material. For the elevated temperature experiments, it was presumed that the localized shear bands were actually transformed shear bands (Figures 4.12 and 4.13) although TEM investigations were not performed to verify the austenitic structure. The transformed shear bands were characterized as highly localized regions of intense deformation devoid of observable grains indicating possible dynamic re-crystallization. The adjacent regions show evidence of tempering (characterized by variations in etch contrast) due to the excessive local temperature rise associated with deformation. Closer investigation of the deformed microstructure indicates that crack initiation occurred as a result of shear band formation and exhaustion of ductility of the specimen which is consistent with Shaw's theory of deformation in machining (Shaw, 1984).

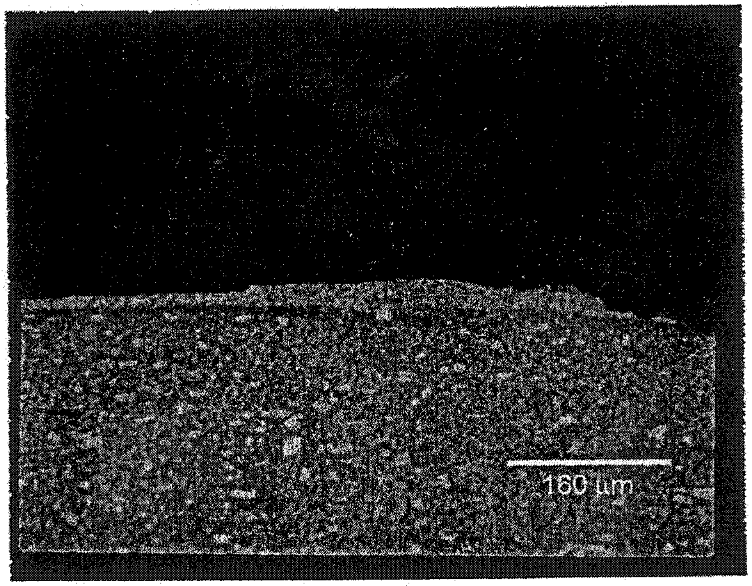

Figure 4.10. Optical image of deformed cross section of shear band showing thermally effected zone and deformed microstructure. (Test temperature: 473 K)

The low temperature experiments revealed deformed shear bands located in the shear zone of the material (figures 4.10 and 4.11). The layers adjacent to the sheared surface show that the grain structure is extremely deformed, indicating considerable large strain deformation localized in the shear zone of the specimen. The lower initial temperature specimens also exhibit a pronounced thermally affected layer indicated by a decrease in the etch contrast. This illustrates that a significant temperature rise occurred during deformation, although not high enough to cause the material to transform.

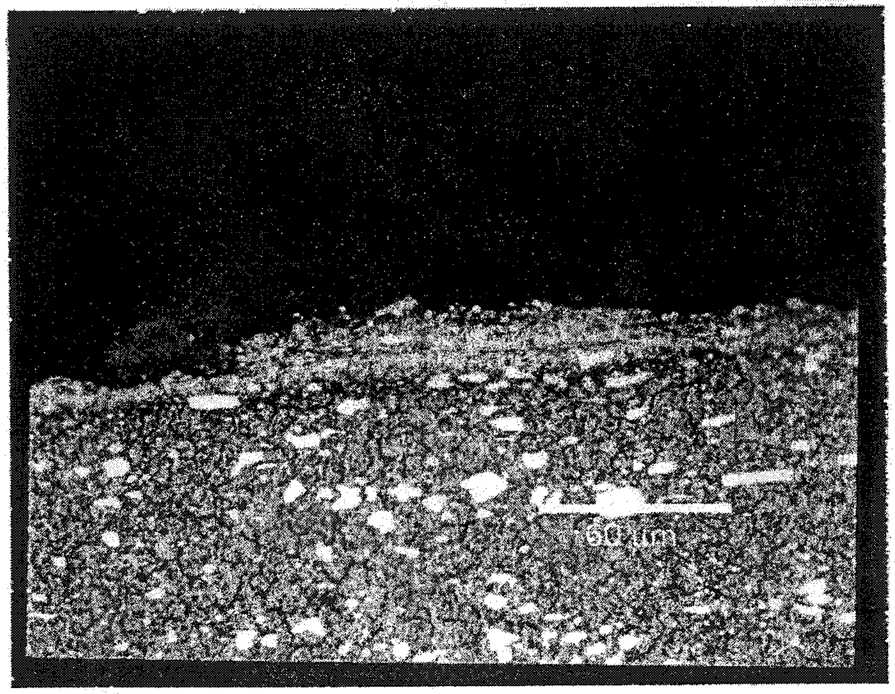

Figure 4.11. Microstructure deformed at 573 K. Note highly deformed grain structure in temperature effected zone.

Cracks were observed to nucleate adjacent to the localized shear bands illustrated in Figure 4.12. This was due to the extreme stress and high local temperatures where thermal softening was more evident as well as high local strain rates accompanying the deformation. The highest temperature shear tests (873 K) revealed shear bands that seemed to act as an interface where the local plastic deformation was less evident below the shear band (i.e. away from the shear zone). Above the localized shear band, local plastic deformation was extremely pronounced, illustrated by the collapsed grain structure in Figure 4.13. The thermally affected zone was observed to be more pronounced in this case.

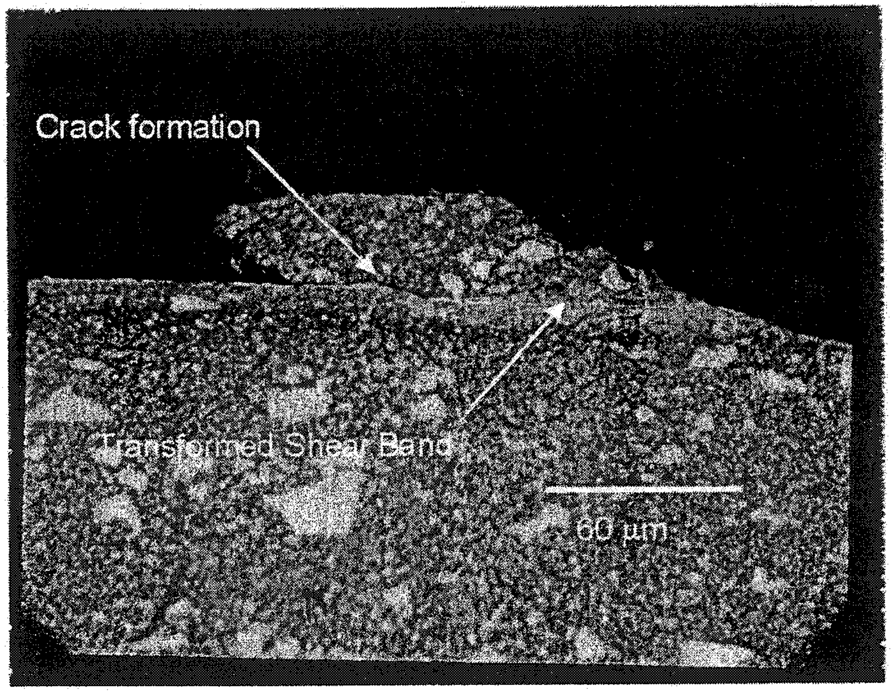

Figure 4.12. Deformed structure at 773 K. Transformed shear band formation is visible along with cracks adjacent to the transformed shear band.

The nominal strain rate for the experiments was computed based on the initial gage length of the specimen (δ in figure 4.2). As gross deformation progresses, local deformation occurs in the defined gage length of the specimen until a critical shear instability occurs. This causes the gage section to collapse into a narrow shear band. The observed deformation bands in figures 4.12 and 4.13 illustrate that the gage length is significantly reduced due to shear localization. Observation of figure 4.12 indicates that the effective gage length is approximately 20 μm for this experimental condition. The reduction of the effective gage length causes the local strain rate to increase, and in this case was in excess of 500000 s^{-1}. This occurred well towards the end of deformation and may be the cause of the instability observed for the high temperature tests. It can be concluded that that local strain rates in the localized shear band may reach almost an order of magnitude greater than the nominal strain rate computed from the initial geometry.

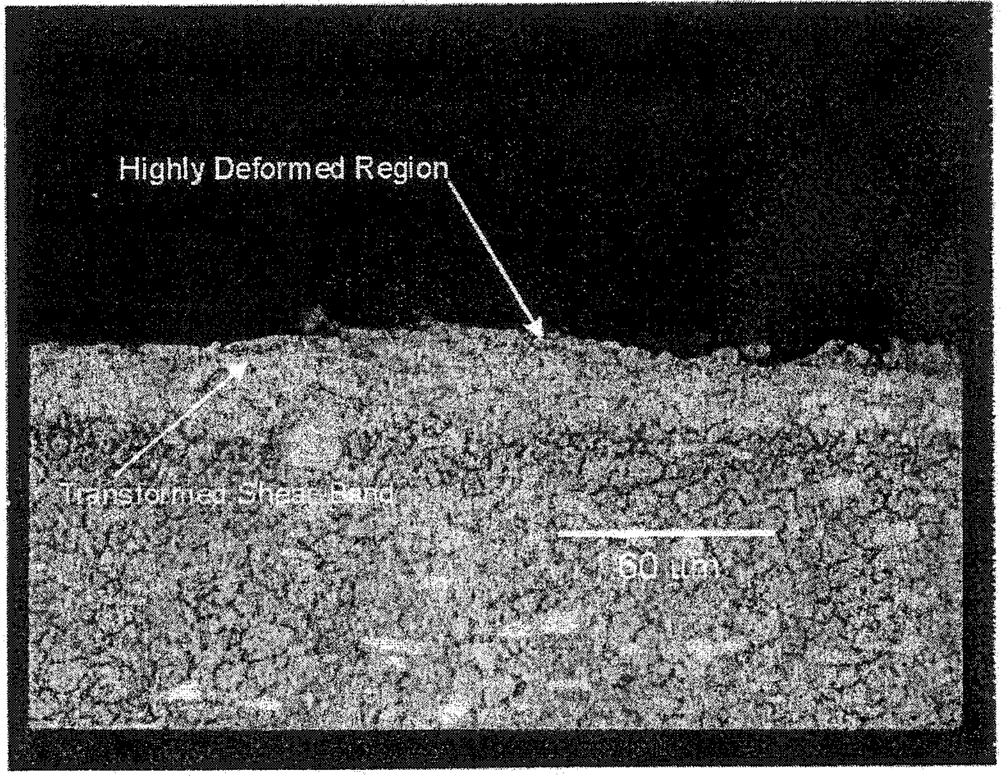

Figure 4.13. 873 K shear microstructure illustrating transformed shear band isolating extreme local plastic deformation.

The sheared specimen interfaces were examined using a scanning electron microscope (figures 4.14 and 4.15). The interfaces at all temperatures exhibit characteristics of gross ductile deformation characterized by a parabolic dimple pattern. No brittle fracture was observed throughout the sheared interfaces. This is interesting because hard materials are considered brittle in nature; they absorb comparatively little energy before gross brittle fracture occurs. However, fractured alloy carbide particles were observed on the interface indicating extremely high local stresses (figure 4.15). The fact that the carbides fractured supplements the reasoning that even at elevated temperatures the carbide particles provide formidable dislocation barriers to increase the strength of the alloy.

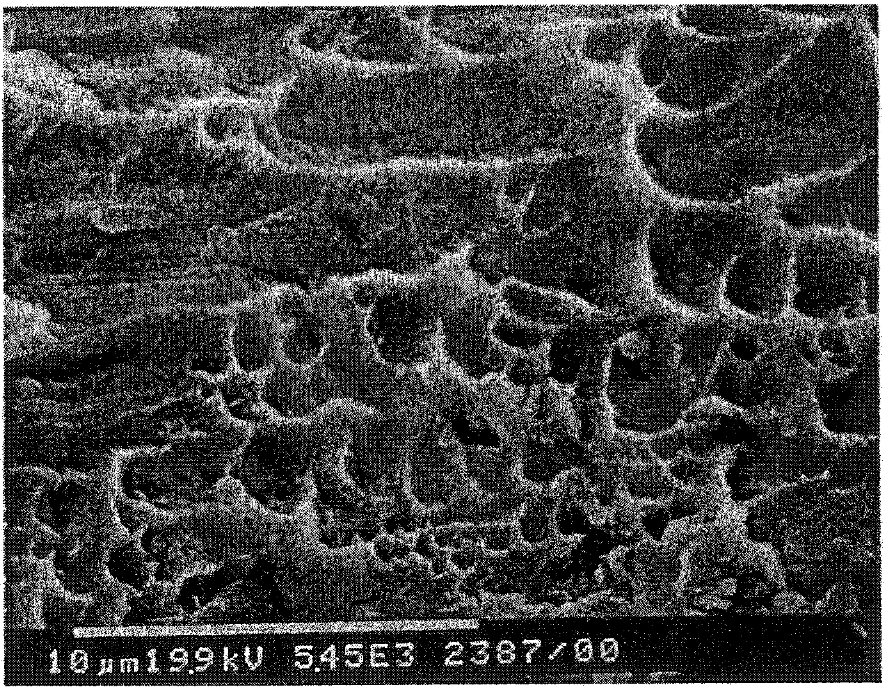

Figure 4.14. SEM micrograph of sheared interface illustrating ductile failure. (Test temperature: 473 K)

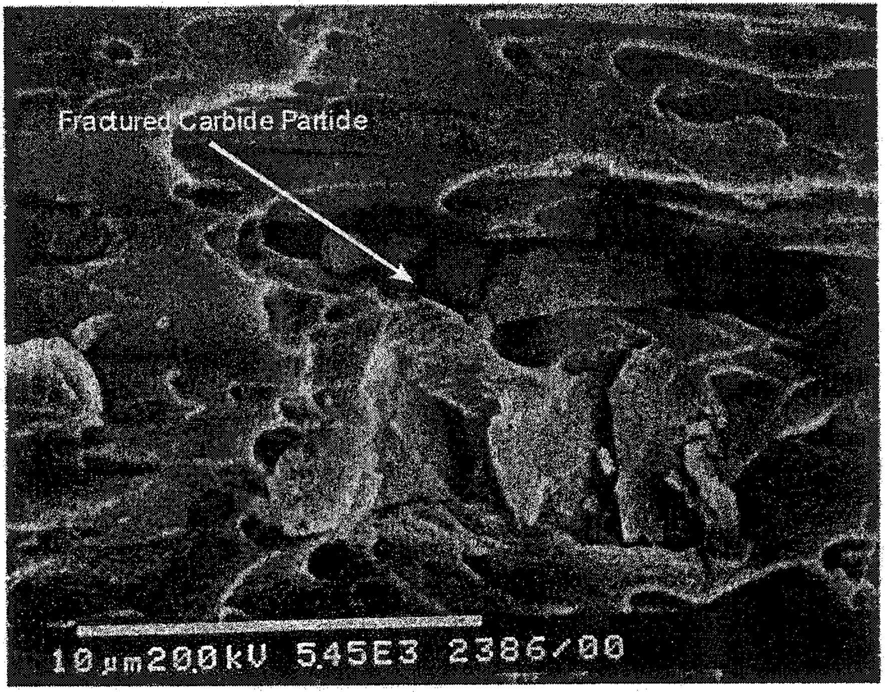

Figure 4.15. SEM micrograph of fractured shear interface showing fractured carbide particle indicating high local stress levels.

Analysis of the fractured surfaces showed the void density increased with increasing temperature. As stated previously, the mobility of the dislocations is strongly dependent on the temperature of the alloy and the strengthening phases. The increase in void density can be attributed to an elevated number of nucleation sites and defects during the shearing process due to increasing dislocation mobility as the local temperature approach one-half of the melting temperature.

4.5 Chapter Summary

The present Chapter explored the high strain rate flow stress behaviour of hardened AISI D2 tool steel. The flow stress was evaluated at strain rates comparable to that of machining processes. The data was used to quantitatively determine the stress-strain behavior at high strain rates and elevated temperatures. It was observed that the material showed minimal temperature sensitivity as a result of the metallurgy of the alloy and its secondary hardening phases. The insensitivity to temperature effects were captured in the constitutive law modeling and the resulting dependence was rationalized based on the material microstructure.

The primary purpose of the investigation was to provide a sound basis for relating the flow stress of the alloy to strain, strain rate and temperature. The flow stress of the alloy was represented using an empirically based constitutive law by a Johnson-Cook formulation. A physically based constitutive law (based on dislocation mechanics) was also used to represent the flow stress in the form of the Zerilli-Armstrong representation. Both constitutive laws provided an accuracy of ±8% providing an accurate description of the stress-strain data presented. It was found that both constitutive law formulations provided very good predictions for the thermal dependence of the flow stress as a function of temperature.

Optical metallography was performed on the microstructure of the sheared specimens characterizing the deformation of the material at elevated strain rates and temperatures. Two localization mechanisms were observed. At temperatures below A3, deformation shear bands were the dominant failure mode. At higher initial temperatures, transformation shear bands occurred since the local temperature rises above the A3 transformation temperature.

Chapter 5

Orthogonal Force Model

5.1 Introduction

This chapter presents the methodology used for the development of a semi-analytic orthogonal force model for segmented chips. The development of the force model is based on three criteria:

1) The constitutive law developed in chapter 4, which provides the high strain rate shear flow stress as a function of strain, strain rate and temperature.

2) The chip morphology, which is used to provide the fundamental kinematic data used in the model.

3) The development of compatible chip formation kinematics, which combined with 1 and 2 form of a time domain simulation.

5.2 Experimental Procedure

The kinematic relations that are necessary for the orthogonal force model were derived from the chip morphology. Great care was taken to ensure that true orthogonal cutting conditions (which produces a 2-dimensional chip formation process) were maintained. The chips were produced by orthogonal tube turning tests to analyse the chip morphology for the cutting speed and feed level used in the ball end milling tests. The largest feed used in this investigation was 0.1016 mm/rev. Shaw has outlined that in order to maintain a plane strain chip formation process the width of cut must be at least 5 times the maximum feed rate (Shaw, 1984). An annealed AISI D2 tool steel cylinder was bored out to form a tube of a wall thickness of 3.175 mm. Clearly, a wall thickness (width of cut) of 0.5 mm would have sufficed. A larger wall thickness was chosen so that a) a wide enough chip was produced for metallurgical mounting and analysis, and b) the tube had the rigidity to be clamped tight in the chuck to prevent chatter due to the large width of cut. The material was heat treated to a hardness of 62 HRc to ensure that the chip formation mechanisms remained the same as in the previous milling tests. The tools used were brazed CBN custom triangular inserts with a sharp cutting edge configuration. High volume fraction CBN was used for the cutting edge material and was identical to the grade used in the milling tests performed in chapter 3. The ball end mill geometry had a -10^o rake angle. The turning tool holder was custom ground to have the same rake (-10^o) with no side rake angle, as no commercial tool was available with this configuration. A side rake angle would create a non-collinear chip flow angle and thus would have created non-orthogonal cutting conditions. A 3-d force dynamometer was used to collect the force data for the turning tests (for verification of the force model). To further reduce the risk of chatter during the cutting tests (because of the large width of cut) an aluminium cylinder was cut to the diameter (plus 0.05 mm to provide a press fit) of the bore and press fit into the tube to the position where the chuck clamped the workpiece. The feeds and cutting speeds were varied according to the cutting conditions outlined in table 5.1. Full factorial testing (4x3 tests) was performed so that the effect of both feed and speed could be quantified with reasonable confidence and correlations could be made.

Parameter varied	Level 1	Level 2	Level 3	Level 4
Cutting Speed (m/min)	55	110	270	380
Feed (mm/rev)	0.0254	0.0508	0.1016	

Table 5.1. Cutting condition parameters varied for orthogonal cutting tests.

The time in cut was kept to a few seconds until the force level stabilized so that tool wear would not affect the chip morphology or chip formation mechanism. The chips produced were collected for analysis. The chips were mounted in a metallurgical cold mount. Extreme care was taken so that the chips were mounted such that the chip cross-section was exactly parallel to the cutting speed vector. Placing the chips in a plasticene base and levelling any chips, which may have moved, with a flat gauge block did this.

Previous experience showed that edge rounding is after polishing occurs when analysing such thin chips. Therefore, a powdered alumina hardening phase was added to the first mm of the cold mount to prevent edge rounding. The chips were then polished and etched to reveal the microstructure.

5.3 Chip Morphology

The morphology of the chips produced was examined with the objective to extract key kinematic data required for the force model. Figure 5.2 shows the features of the chip that were analysed. It can be seen that the orthogonal turning tests produced chips with the saw toothed type morphology. Several points should be made about the chip morphology. Shear bands in the primary and secondary shear zones are clearly observable from the chip micrographs. This is in contrast to the "bulk" portion of the chip where it can be observed that no deformation has occurred. This is indicated by the fact that no distortions of the grains are observed in the microstructure. It is therefore assumed that all deformation occurs in the primary and secondary shear zones. The slip distance (outlined in figure 5.2) also correlates to the cutting conditions and will be shown. The significance of the slip distance in the figure is that it provides the segmentation frequency of the saw toothed type chip when normalized by the cutting speed (Shaw, 1997, 1999).

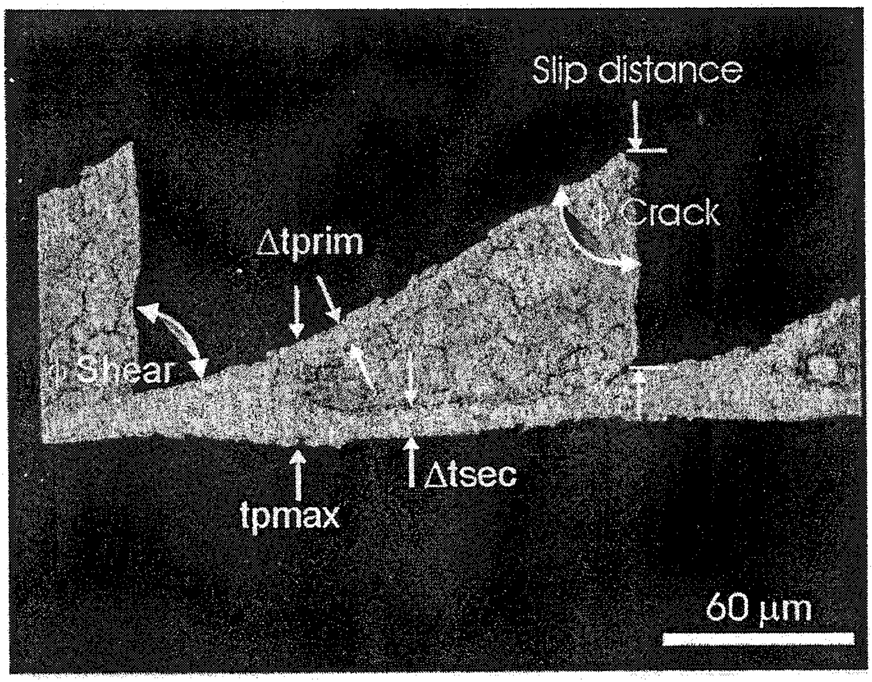

Figure 5.2. Typical chip morphology of chip produced showing key features and nomenclature used for analysis.

A phenomenological comparison of the morphology of the chips produced compared to the cutting conditions was performed. The results showed that the chip formation in hard machining would provide a systematic method way of defining the kinematic features of the cutting process. Figure 5.3, 5.4 and 5.5 show the chips produced where at different feed levels. The cutting speed remained constant at 270 m/min. It can be seen from figure 5.3 to 5.5 that the segmentation frequency increases as for decreasing the feed rate. Recall that the segmentation frequency is defined as the time it takes for the tool to traverses the segmentation distance. Clearly, this produces one chip segment. Normalizing the cutting speed over the segmentation distance provides the characteristic chip formation time in the frequency domain.

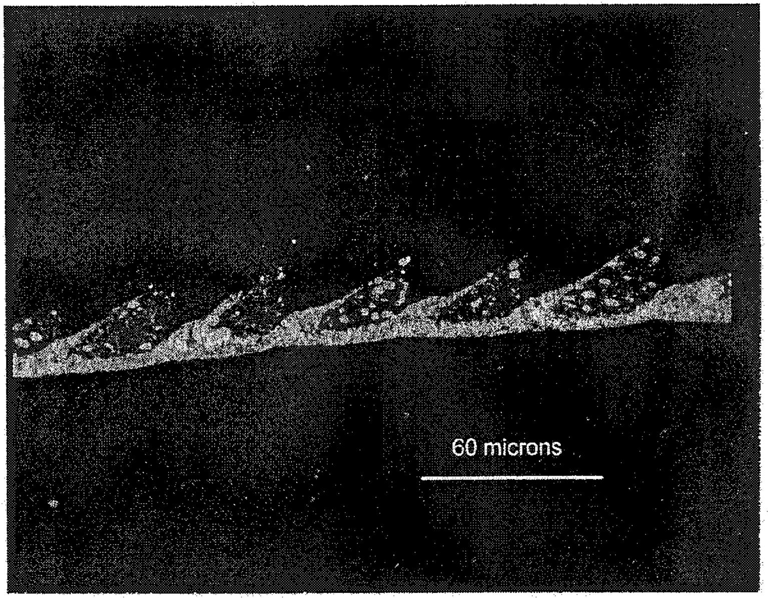

Figure 5.3 Morphology of chip produced at a feed level of 0.0254 mm/rev and a cutting speed of 270 m/min.

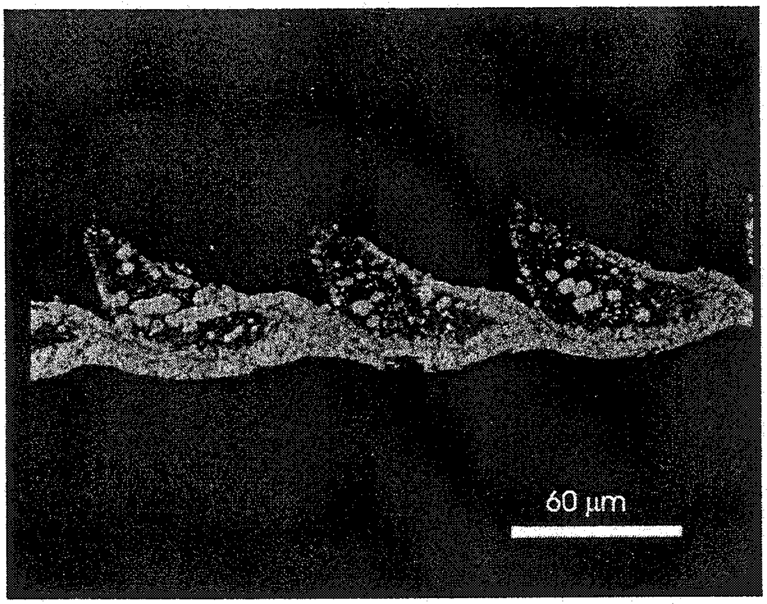

Figure 5.4 Morphology of chip produced at a feed level of 0.0508 mm/rev and a cutting speed of 270 m/min.

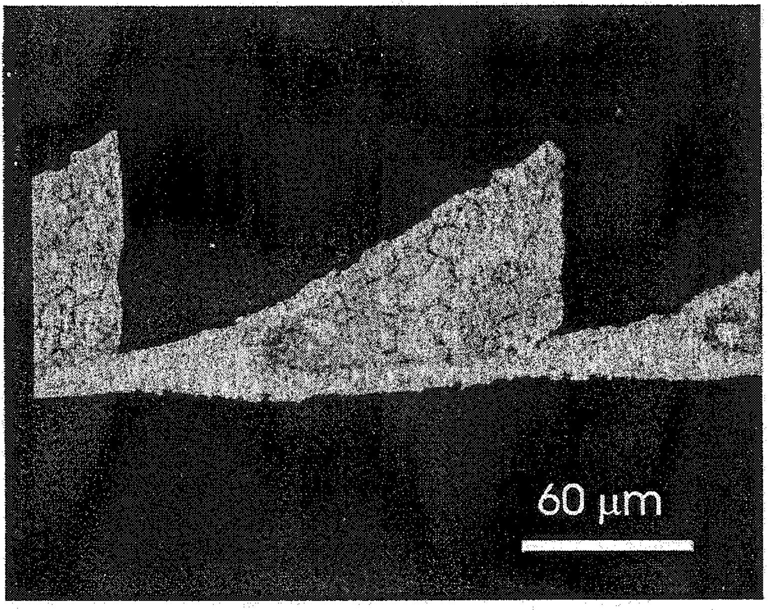

Figure 5.5 Morphology of chip produced at a feed level of 0.1016 mm/rev and a cutting speed of 270 m/min.

The segmentation distance was measured for all cutting conditions and is illustrated in figure 5.6. There appears to be a linear correlation for the feed variation. However, when the data is normalized into the frequency domain, the correlation between segmentation frequency and cutting speed and feed rate becomes very apparent. This is illustrated in figure 5.7. This figure shows that as the feed rate is increased, the chip formation time lengthens causing larger segments to form. These results are consistent with those presented by Kishawy (1998). It is apparent that the deformation increases with increasing feed rate.

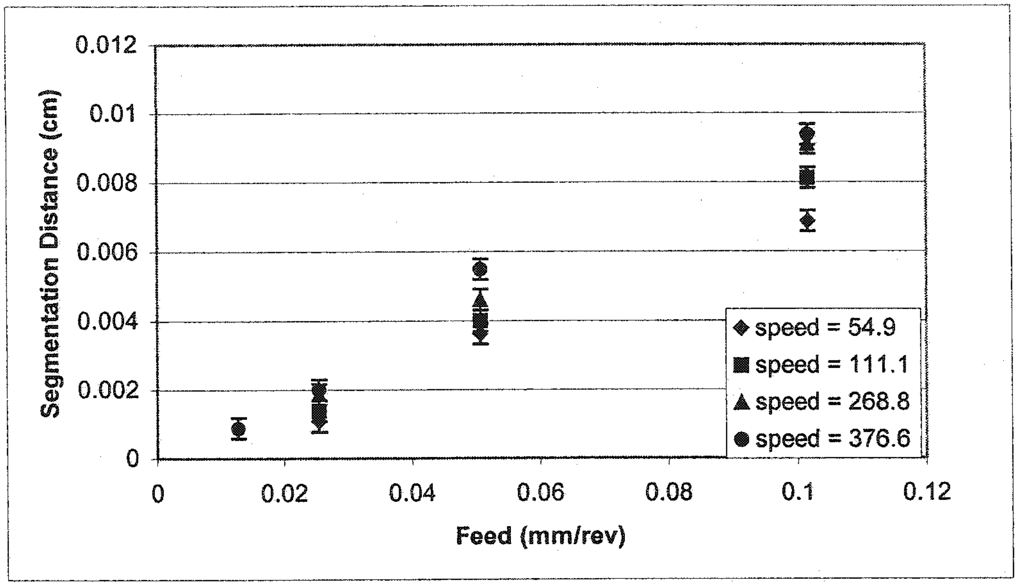

Figure 5.6. Variation of segmentation distance against feed rate for all conditions investigated.

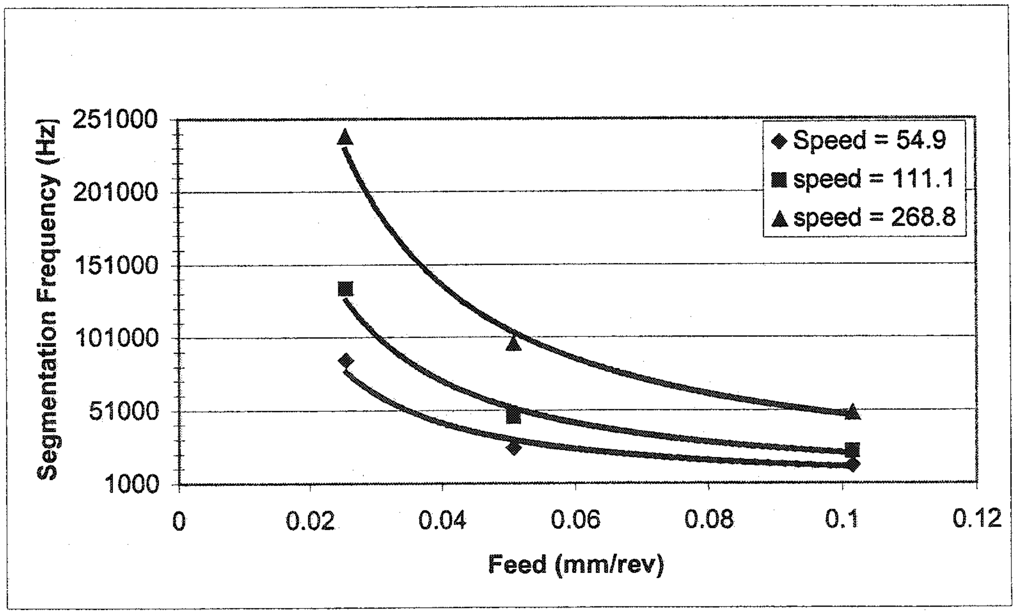

Figure 5.7. Variation of segmentation frequency for all conditions investigated showing the correlation between feed and cutting speed.

To produce a viable definition of strain, the gauge length for shear must be established. The gauge length for the secondary shear zone is defined as the thickness of the deformed shear band. Komanduri et al. (1982) used this definition of strain in segmented chips for analysing the thermal variation of the chips to determine shear instability in the primary shear zone. However, the concept is general and is not specific to the primary shear zone, and can be used for determining the strain in the secondary shear zone as well. Figures 5.5, 5.8 and 5.9 present the chips produced for a variation in cutting speed at a feed rate level of 0.1018 mm/rev. It can be seen that the segmentation distance is not as sensitive to cutting speed as it is to changes in feed level. Another feature that is readily observable from the microstructure is the variation of the secondary shear zone thickness (Δtsec). It can be seen that there appears to be a correlation with the cutting speed and the reduction in thickness of Δtsec. Figure 5.10 illustrates this correlation. The data was obtained by gathering 20 segments at random for each cutting condition and measuring the thickness of the deformed shear band. Figure 5.10 shows that the secondary shear zone increases with both cutting speed and feed.

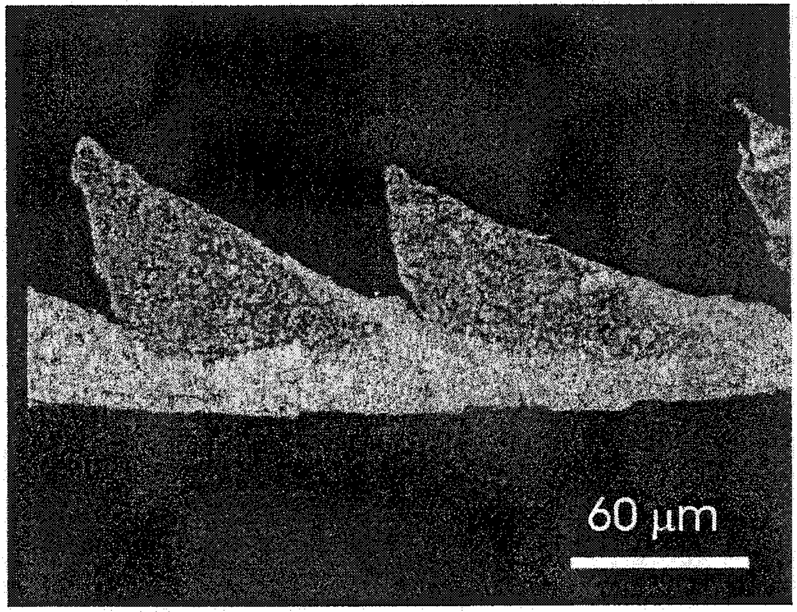

Figure 5.8 Morphology of chip produced at a feed level of 0.1016 mm/rev and a cutting speed of 55 m/min.

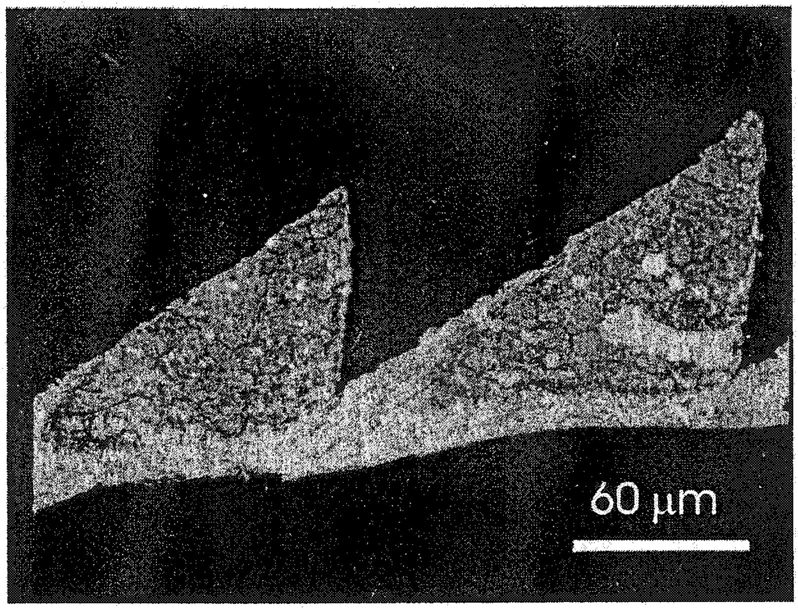

Figure 5.9 Morphology of chip produced at a feed level of 0.1016 mm/rev and a cutting speed of 110 m/min.

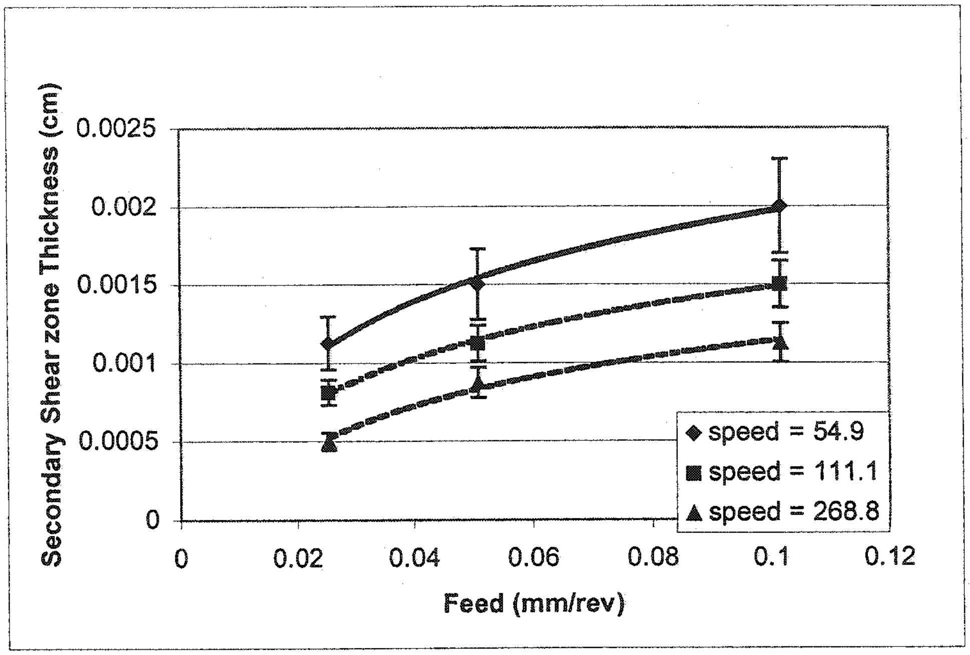

Figure 5.10. Variation of the secondary shear zone for all cutting conditions.

During machining, the cutting speed influences the flow stress of the material due to strain rate and temperature variations. The result is a variation in the strain of deformation as the chip forms. This is shown in figures 5.5, 5.8 and 5.9 where it can be seen that there is a correlation between the primary shear zone thickness and cutting speed. The dependence on feed rate is more pronounced as presented in figure 5.11. Figure 5.11 shows that variation of the primary shear zone thickness (dictated by the shear band thickness adjacent to the root of the chip) decreases with increasing cutting speed, and increases with increasing feed. Phenomenologically, it appears that the shear strain (γ) in the primary shear zone in metal cutting increases with increasing cutting speed as defined by the shear displacement over the gauge length, $\gamma = \Delta d / \Delta tprim$. This conclusion may be easily drawn because of the fact that the segmentation distance is insensitive to cutting speed and remains the same magnitude. It also appears that the strain decreases with increasing feed using the same argument. However, it must be kept in mind that the segmentation distance (slip distance) is very dependant on the feed level. Increasing the feed increases the shear band thickness, however the slip distance increases as well roughly with the same magnitude. This indicates that the strain remains the same magnitude (or relatively constant) for variations in feed. This is consistent with the results obtained by Jaspers (1999). Thus, care must be taken when interpreting the correlations regarding strain variation as a function of cutting conditions. Strain is a very complex phenomenon in metal cutting and requires the development of concise correlations.

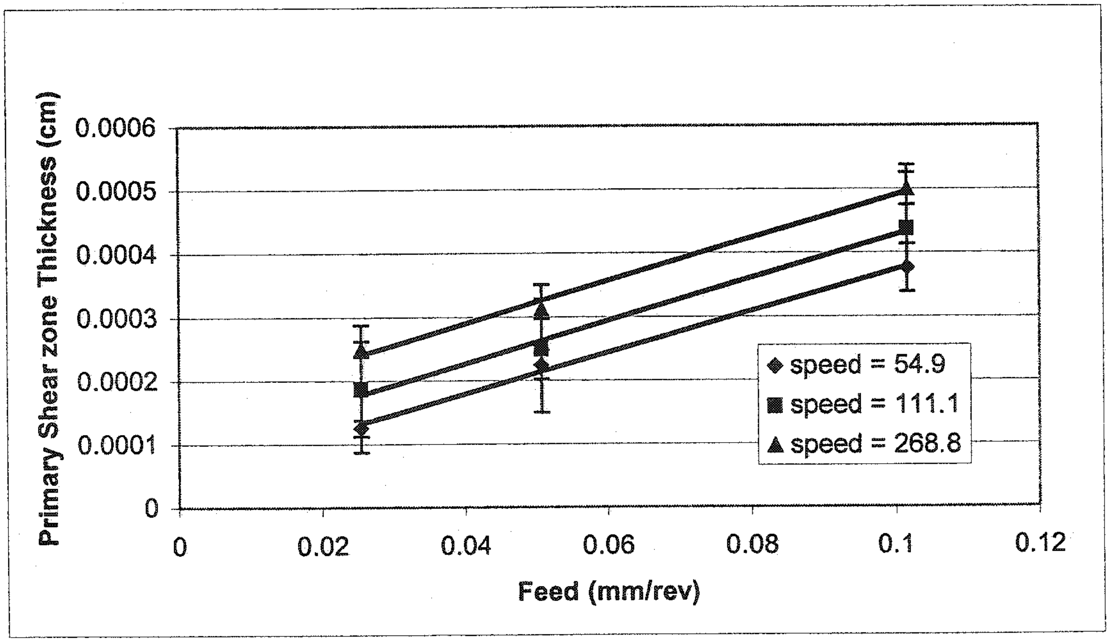

Figure 5.11. Variation of the primary shear zone for all cutting conditions.

The analytic determination of the shear strain on the secondary shear zone requires that the contact length of the chip on the tool rake interface be determined. This was done by directly analysing the contact on the tool rake under the SEM. Figures 5.12 and 5.13 shows a typical tool rake face for the cutting condition that produced the chips of figure 5.5 and 5.8 respectively. It can be seen that there are 2 zones of interest. There is a zone which corresponds to the magnitude of the feed (depth of cut) illustrated by the material adhered to the rake face of the tool. A second zone is present where presumably the chip interfered with the rake face due to momentum, yet does not contribute to cutting. Thus, a reasonable estimate of the contact length of the secondary shear zone is one undeformed chip thickness (i.e. the feed rate).

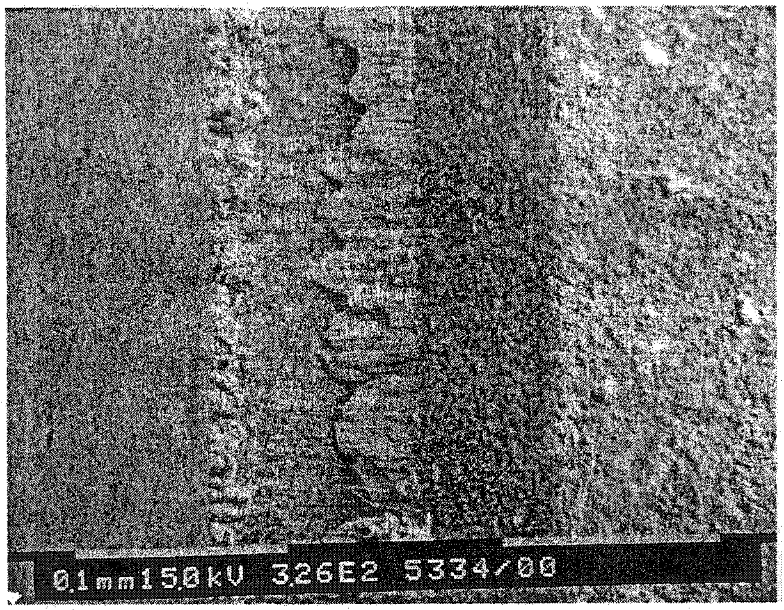

Figure 5.12. SEM image of the rake face of the cutting tool producing the chips in figure 5.5. (V= 270 m/min, f=0.1016 mm/rev).

Figure 5.13. SEM image of the rake face of the cutting tool producing the chips in figure 5.5. (V=55 m/min, f=0.1016 mm/rev).

Forces were measured for the cutting tests for future verification of the orthogonal force model. Figure 5.14 shows the experimental resultant force variation for all of the cutting tests. It is interesting to note that there is a definite minimum in the cutting force where a reduction of 25% for the high feed rate (f=0.1016 mm/rev) is observed. The minimum occurs between 110 and 270 m/min. This result was completely unexpected. It may indicate that there is an optimum cutting speed for cutting AISI D2 tool steel if force minimization is used as a criterion for optimisation. This proved to be a challenge to model the cutting force profile.

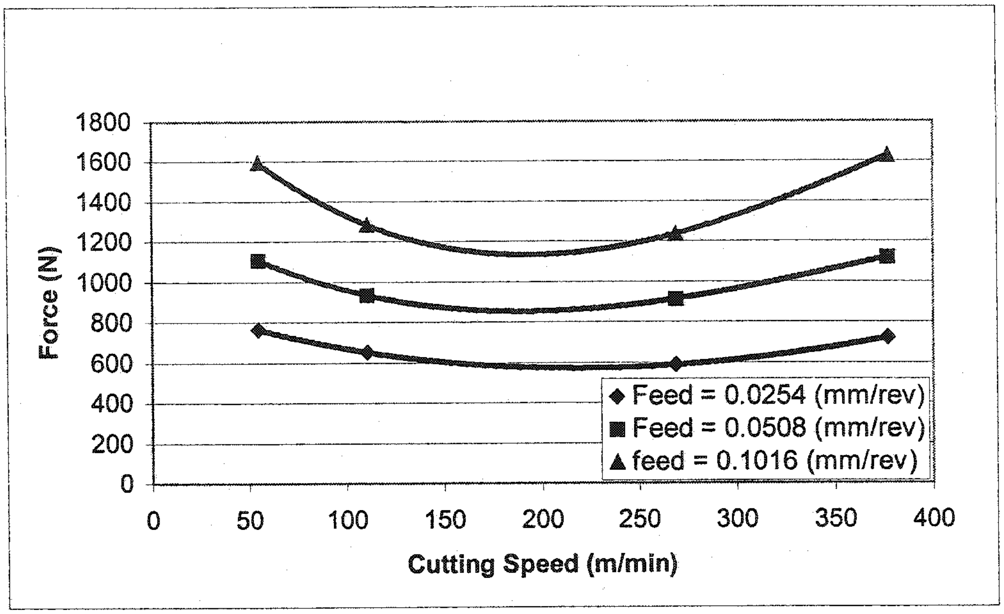

Figure 5.14. Total resultant force as a function of cutting speed for orthogonal turning AISI D2 tool steel at HRc 62. (Note the force minimum for a feed of 0.1016 mm/rev)

5.4 Force Modelling Methodology

The present force model implements a constitutive law based shear stress model that depends on the strain, strain rate and temperature generated during saw toothed chip formation. It is assumed that deformation occurs in two distinct shear zones, shown in Figure 5.15. The present approach models the shear tractions for each consecutive shear zone. The method for computing the force (F) in each shear zone is represented by:

$$F = \tau(\gamma, \dot{\gamma}, T)A(f, V) \qquad (1)$$

where τ is the stress obtained from the governing constitutive equation dependant on the strain, strain rate during chip formation, and consequently the temperature derived from the mechanical work done, and A(f,V) is the area on which the shear traction occurs, expressed as a function of feed (f) and cutting speed (V).

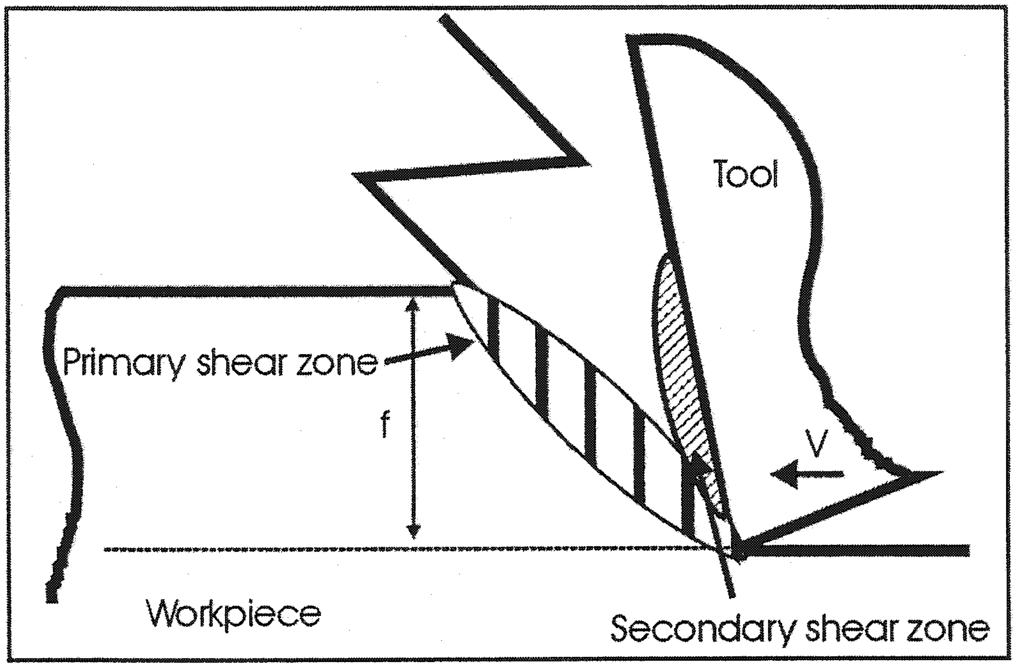

Figure 5.15. Definition of primary and secondary shear zones in orthogonal machining.

5.4.1 Constitutive Law

The Johnson-Cook constitutive law developed for high strain rates and temperatures in the previous chapter was used to represent the shearing tractions:

$$\sigma = (A + B\varepsilon^{n})(1 + c\log(\frac{\dot{\varepsilon}}{\dot{\varepsilon}_{o}}))(1 - \left(\frac{T - 298}{T_{M} - 298}\right)^{m}) \qquad (2)$$

where A,B,C,n,m are material constants, ε is the effective strain, $\varepsilon^{\bullet}$ is the effective strain rate, T and T_M are the absolute temperature during deformation and melting temperature of the alloy respectively. The constitutive law coefficients are outlined in table 5.2.

Coefficient	D2 (Becze et.al, 2000)	4340 (Lee and Yeh, 1997)	IN718 (Jaspers, 1999)
A (MPa)	1766	950	1029
B (MPa)	904	725	1477
C	0.012	.015	0.0
n	0.312	0.375	0.326
m	3.38	0.625	1.9
Tm (K)	1733	1733	1677

Table 5.2. Constitutive law coefficients used for the present investigation.

Conversion of the constitutive law from effective stress, strain and strain rate to shear stress, strain and strain rate was performed using the Von Mises relation:

$$\tau = \frac{\sigma_{eff}}{\sqrt{3}}, \varepsilon_{eff} = \frac{\gamma}{\sqrt{3}}, \dot{\varepsilon}_{eff} = \frac{\dot{\gamma}}{\sqrt{3}} \qquad (3)$$

5.4.2 Determination of Strains and Strain Rates from Chip Formation

The deformation of solid bodies generally depends on three measurable parameters; the amount a material deforms (strain), the rate at which the load is applied (the strain rate) and the temperature of deformation. When a material is subjected to these conditions, it responds with a unique flow stress. Determination of the flow stress in terms of strain, strain rate and temperature space was the fundamental objective of determining the constitutive representation of the flow stress in chapter 4. The governing constitutive law uses strain, strain rate and temperature as independent variables to model the flow stress during chip formation. Common parameters in metal cutting do not provide the user directly with strain, strain rates and temperatures in machining. Parameters such as cutting speed, feed rate, and depth of cut are used to control or represent the cutting process. Fundamental parameters such as strains and strain rates in metal cutting are derived properties. They depend on the cutting conditions, the mechanical properties of the material, the tool geometry, any tool wear, the tool material used, as well as chip morphology to name a few. These properties are highly coupled, and as a result are very difficult to incorporate into an all-encompassing model that includes every effect. Since the flow stress of the material is directly dependant on the strain and strain rate, the strains and strain rates were expressed as functions of the process parameters, namely tool geometry, feed and speed.

The shear strain in the primary shear zone can be represented using the geometrical relations governed during chip formation. Using the definition of shear strain in metal cutting theory (figure 5.16) (Shaw, 1984), the shear strain is can simply be represented as the mean slip deformation in the direction of shear (ΔS in figure 5.16) over the gauge length (Δy in the figure). For segmented chips, Komanduri and co-workers (1981) used a similar definition of shear strain for shear localized chip analysis. Thus for the present work, the shear strain in the primary shear zone for segmented saw toothed type chips may be defined as:

$$\gamma_{\text{prim}} = \frac{\Delta d_{\text{prim}}}{\Delta t_{\text{prim}}} \tag{4}$$

where Δd_{prim} is the slip distance, and Δt_{prim} is the gauge length of the primary shear band (obtained from chip micrographs). The previous section showed that the slip distance could be represented by the segmentation frequency. However, tool geometry, namely the rake angle (α) also needs to be considered to orient the slip vector onto the shear plane.

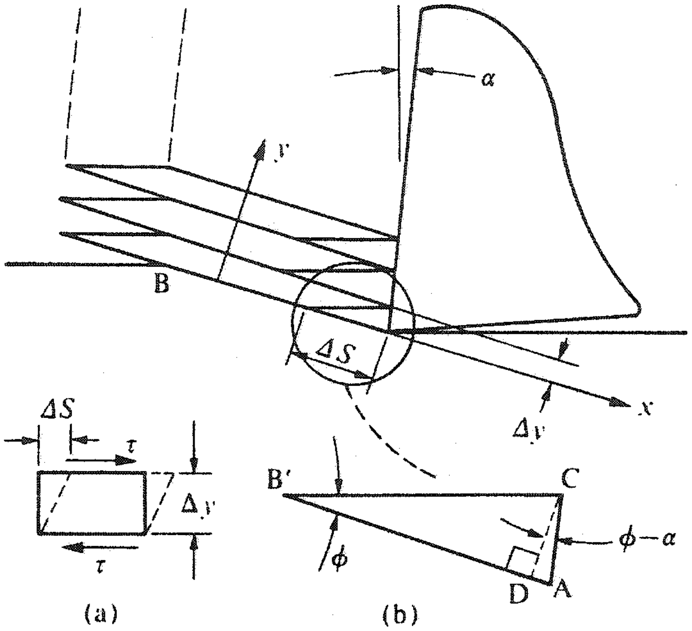

Figure 5.16. Definition of shear strain in primary shear zone. a) general definition, b) in metal cutting. (After M.C. Shaw, Metal cutting Principles, Oxford Scientific Publications, 1984. pg. 27)

The strain rate in metal cutting is of primary importance as it offsets the effects of temperature at very high strain rates (MacGregor, 1944). In metal cutting, the strain rate is determined by two fundamental parameters, namely the shear velocity, and the gauge distance over which shearing has occurred. The shear velocity is very simply determined by a geometric transformation of the cutting speed vector onto the shear plane (provided the shear angle is known). The gauge length must be determined through examination of the chip microstructure. Since a thin shear zone model is assumed, the gauge length is simply Δt_{prim}. Thus the strain rate in the primary shear zone is defined as:

$$\dot{\gamma} = \frac{V_S}{\Delta t_{prim}} = \frac{\cos\alpha}{\cos(\phi-\alpha)}\frac{V}{\Delta t_{prim}} \tag{5}$$

where V_s is the shear velocity, ϕ is the shear angle, and α is the rake angle.

Through similar arguments as presented above, the strain in the secondary shear zone is dependant on the deformed band thickness (Δt_{sec}) as well as the contact length, C_L, measured on the tool-chip interface, and is defined as:

$$\gamma_{sec} = \frac{C_L}{\Delta t_{sec}} \tag{6}$$

The strain rate on the secondary shear zone is dependant on the relative velocity of the chip (Vc) sliding against the rake face of the cutting tool. The relative velocity of the chip against the rake face may be determined from a geometric transformation similar to that of the chip velocity. Knowing the cutting speed, the rake angle and the shear angle, the chip velocity can be determined. Thus, the strain rate in the secondary shear zone can be obtained from the cutting speed (V) and (Δt_{sec}):

$$\dot{\gamma} = \frac{V_C}{\Delta t_{sec}} = \frac{\sin\phi}{\cos(\phi-\alpha)}\frac{V}{\Delta t_{sec}} \tag{7}$$

The kinematic parameters defining the deformation in the primary and secondary shear zones have been defined. It may now become apparent how necessary the chip morphology analysis was. Unfortunately, there is no analytical closed form solution for the parameters collected from the chip morphology. The thickness of the primary and secondary shear zones are uniquely determined by the cutting conditions and the material properties. However, a closed form solution has yet to be proposed which will uniquely solve this problem. The reason is because the entire system (tool/workpiece interaction) is an unconstrained problem. No viable boundary conditions can be determined *a priori* so that a unique solution can be obtained. It was thus concluded that the only alternative was to measure the necessary parameters manually and represent them empirically.

5.4.3 Chip Morphology Analysis

Section 5.3 showed the variation of the chip morphology as a function of cutting conditions. It is evident that all kinematic data required for the model must be obtained from chip microstructure (refer to figure 5.2 for the definitions used in the present context). The segmentation frequency (ν), necessary for computing the primary shear strain, was previously shown to depend on (in fact, derived from) the slip distance. The segmentation frequency was computed using the segmentation distance (D) (measured from micrographs of the chips produced during orthogonal cutting tests) and the cutting speed (V). It may seem confusing that the actual cutting speed (V) is used as opposed to the shear velocity (Vc) according to the concept developed for the primary shear strain. The slip distance vector as defined in figure 5.2 is in the direction of the prescribed cutting speed V, and therefore the actual cutting speed must be used.

An empirical representation of the segmentation frequency is sought which is a function of the input parameters being the cutting speed and feed. A multidimensional, multivariable regression analysis was used to develop an empirical form that parametrically determines ν in terms of f and V:

$$\nu = \left(A_v + B_v \mathrm{Log}(f)\right)\left(C_v + D_v V^{E_v}\right)\left(1 - F_v f^{G_v}\right) \qquad (8)$$

where A_υ, B_υ, C_υ... are the minimised constants. Figure 5.17 illustrates correlation of the experimental data with the empirical for represented by equation 8. Note that the form of equation 8 incorporates both the effect of feed and cutting speed to represent the segmentation frequency. However, there is no physical justification of the general form of equation 8, it arises from trial and error.

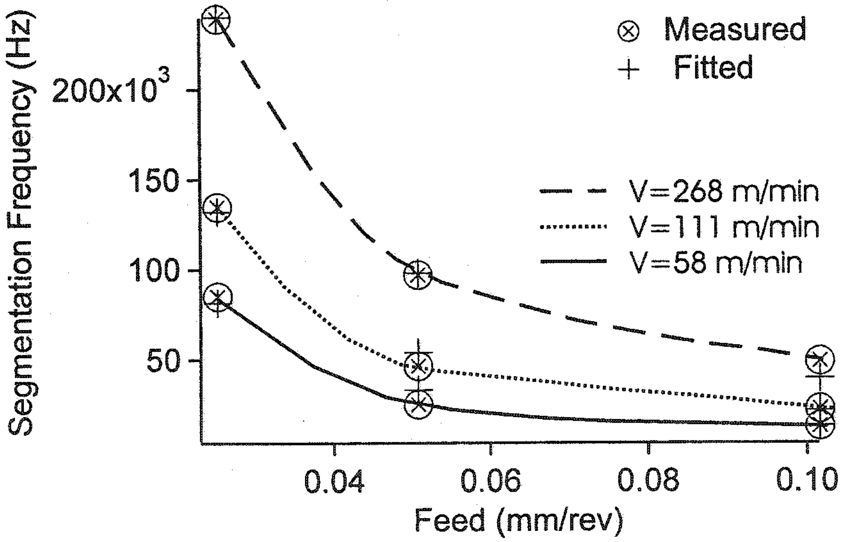

Figure 5.17. Empirical representation of Segmentation frequency as function of feed and speed for AISI D2 Tool Steel.

The strain levels during chip formation are presumed to arise from localised shear band formation. The values of the shear band thickness were obtained by measuring the deformed bands in both the primary and secondary shear zones. It was found using the same regression technique, that an empirical form could represent the behaviour of the deformed shear band thickness in both the primary and secondary shear zones. The empirical form is represented by equation 9 (in terms of f and V):

$$\Delta t_{\text{prim or sec}} = \left(A + B\exp(CV)\right)\left(1 + D\left(\frac{f - fo}{fo}\right)\right) \qquad (9)$$

where A,B,C,D, are the minimized constants, and f_o is an arbitrary minimum feed level. The form of equation 9 merits some explanation. The relatively simple form of equation 9 arose from the trends observed from the data collected using the chip morphology. It was observed from the chip microstructure that the shear band thickness was relatively sensitive to cutting speed. Therefore and exponential dependence was chosen to represent the effect. The linear correlation regarding the feed dependence was chosen such that at a certain feed level (depending on the shear zone) the shear band thickness would diminish and force the value would approach zero. This corresponds to a non-deformed condition. Figures 5.18 and 5.19 show the correlation of the measured shear band thickness to the fitted representation of equation 9. The functional form of equation 9 adequately represents the data. Note that multidimensional form of equation 9 captures the trends in terms of both feed and speed. The benefit of this formulation is that it provides a mathematically continuous parametric representation of the deformation characteristics in cutting speed and feed space. Table 5.3 provides the values of the minimized constants.

Coefficient	Segmentation frequency (eq. 8) (Hz)	Primary shear zone (eq.9) (mm)	Secondary shear zone (eq. 9) (mm)
A	0.7127	-1.713e-5	5.5732e-5
B	0.015381	1.859e-5	1.12e-4
C	19.6996	1.47e-5	0.0124
D	-34.6179	0.442607	0.261025
E	0.662656		
F	2.1742		
G	-1.2936		
fo		0.0254	0.0254

Table 5.3. Minimized coefficients used to define the chip morphology.

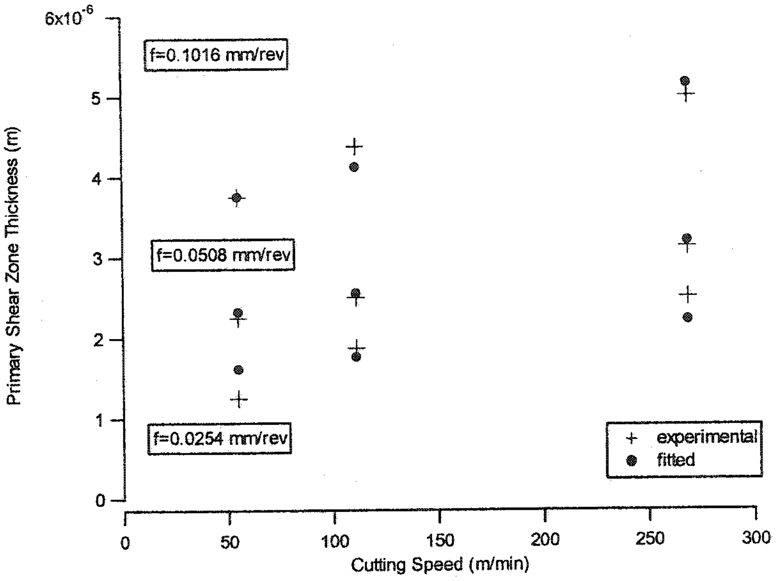

Figure 5.18. Primary shear zone thickness parametric representation from equation 9 with experimental data.

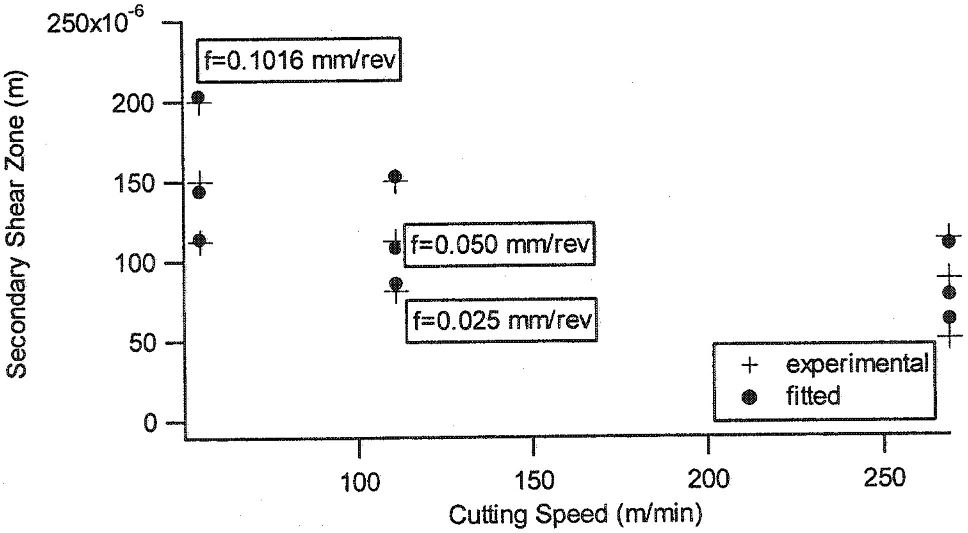

Figure 5.19. Secondary shear zone thickness parametric representation from equation 9 with experimental data.

5.4.4 Time Domain Simulation Development

The equations developed previously for the deformation characterisation of the chips produced during turning are clearly time dependant. Thus, a time domain simulation has been developed based on the analytical representation of the chip formation kinematics, as wells as the empirically represented data collected from the chip microstructure. The simulation ensures that the final strain levels were compatible with the segmentation frequency (i.e. slip distance). The strain rates obtained from equation (5) and (7) allow the computation of the strain path for each shear zone in the time domain until the maximum strain level is obtained. In reality, the strain rate in each shear zone is not constant. Determination of the temporal strain rate distribution as a function of deformation in machining has yet to be proposed. Thus, for the present investigation, the strain rate is assumed to remain constant. This facilitates determination of the strain, and provides a unique strain rate as a function of cutting conditions. Therefore assuming that the strain rate is constant, the strain path taken as a function of time (t) is expressed such that the strain is consistent with the strain rate by maintaining:

$$\gamma(t) = \int_0^t \dot{\gamma}\, dt \qquad (10)$$

This essentially provides a linear scaling of strain throughout the deformation process. However, this provides no upper bound on the strain level (as it merely provides the strain path). Clearly, it is required to place a maximum bound the shear strain so that a compatible chip form will (numerically) result. The maximum shear strain achieved is clearly a function of the cutting conditions. Therefore, the maximum shear strain γ_{max} (f,V) was obtained using equation (4) and (6) implicitly. The use of equation 10 implies that the strain at any time during the chip formation characteristic time (i.e. the segmentation period which is the reciprocal of equation 8) follows a linear path in time. Since equation 8 provides the segmentation frequency, the strain at time t may be expressed as:

$$\gamma(t) = \gamma_{max}\left(\frac{1}{\nu(f,V)} - t\right) \quad 0 \le t \le \frac{1}{\nu(f,V)} \tag{11}$$

Equation 11 ensures that compatibility is maintained for each chip formation cycle.

Equations 4 to 11 provide the strain and strain rate to establish the strain history as functions of feed and speed. It is also necessary to predict the instantaneous temperature to establish the time dependant shear stress. Calculation of the time dependant temperature is accomplished by using the strain history, and by integrating the strain energy during deformation for each strain increment. Thus, at any time increment t_i, the strain energy is used for the update in the flow stress relation. Thus, at any strain increment $\gamma(i)$, the instantaneous temperature rise is computed by:

$$T(\gamma, \dot{\gamma}, t) = T_o + \frac{R}{\rho Cp}\int_0^{\gamma(i)} \tau(\gamma(i), \dot{\gamma}(i), T_{i-1} d\gamma \tag{12.a}$$

$$R = \frac{1}{1 + 1.328\left[\frac{K\gamma}{Vf}\right]^{\frac{1}{2}}} \tag{12.b}$$

where R called the Lowen and Shaw partition coefficient depending on the shear zone (Shaw, 1984), ρ is the density, Cp is the heat capacity, K is the diffusivity of the workpiece ($K=0.13\times10^{-4}\ m^2s^{-1}$) and T_o is the initial temperature. The term $\int_0^{\gamma(i)} \tau(\gamma(i),\dot{\gamma}(i),T_{i-1})d\gamma$ is the work done to the i^{th} time step using the previous temperature T_{i-1} as an initial boundary condition (i.e. the new temperature is added to the previous temperature and the flow stress is updated to the time level of t_i). This dynamically updates the flow stress during the chip formation cycle. The flow stress (τ) is thus represented as a dynamic function of the strain and temperature during chip formation.

The flow stress computed to each maximum strain level was used to convert the shearing traction to a force by applying the traction on the dynamic shear plane area A(t). Since the dynamic shear plane area changes as the chip localises, the shear plane area for each time increment (δt) was computed using:

$$A(t) = b\left(\frac{f}{\sin\phi} - \frac{\cos\alpha}{\cos(\phi-\alpha)} V\cdot\delta t\right) \qquad (13)$$

where b is the width of the shear plane. Note that the first term in equation 13 ($f/\sin\phi$) is the original shear plane length as a function of the original geometry. The second term ($V\cos\alpha/\cos(\phi-\alpha)$) is merely the velocity of the shear plane. If the velocity is multiplied by the time increment, then this provides the amount of slip occurring on the shear plane as a function of time. Note also that it is impossible to have a shear plane area larger than that governed by equation 13 at time t=0 which is determined through geometry. Since the characteristic time of chip formation (provided by the segmentation frequency of equation 8) is determined *a priori*, the maximum time increment provides with the maximum allowable slip of the primary shear zone. This formulation was done to ensure that a compatible strain formulation was achieved and that the resulting tractions can be applied to a realistic area (to resolve into force).

It is evident that the purpose of the of the previous discussion was to model the cutting process in terms of shear stresses occurring as a result of chip formation. The simulation was designed for the time domain, where as all the kinematic data from the chip morphology was obtained from the deformed condition (i.e. post mortem). The key correlation was the segmentation frequency, which allowed the deformation to be transformed from strain space into the time domain. Thus to arrive at the shear force, the shearing stress as a function of time (τ (t)) needed to be applied to the dynamic shear plane area. The Johnson-Cook representation of the flow stress requires strain, strain rate and temperature as parameters to represent the flow stress. The temporal formulation follows from equation 11 to obtain strain as a function of time. The strain rate is assumed to be constant and depend only on the cutting conditions, and therefore may be used without any transformation. The temperature on the other hand, was independently computed from the work done during deformation and as a result is directly transformable into the time domain. The general formulation of the shearing force (irrespective of the shear zone) can be represented as 14.

$$F_{shear} = G(\alpha,\phi,V,f)\iint_A \tau(\varepsilon(t),\dot{\varepsilon},T(\varepsilon,\dot{\varepsilon},t))dA \tag{14}$$

The analytic function $G(\alpha\phi,V,f)$ is a geometric transformation unique to each shear zone and resolves the shear traction back to the global coordinate system, and τ is the instantaneous shear flow stress in time. The representation of the transformation into the shear zone is expressed using the following argument. Let τ_{prim} represent the primary shear zone stress, and τ_{sec} represent the secondary shear zone stress. Then, the transformation to the global coordinate system is:

$$Fx = b(\tau_{prim}\cos(\phi) + \tau_{sec}\sin(\alpha)) \tag{15 a}$$

$$Fy = b(\tau_{prim}\sin(\phi) + \tau_{sec}\cos(\alpha)) \tag{15 b}$$

A flow chart is presented in figure 5.20, which graphically depicts the method in which the time domain simulation operates. The basic inputs for the orthogonal simulation are feed and cutting speed. The width of cut is also entered however, it is only used for determining the cutting force on the shear plane area. There are 3 core modules in the simulation;

1.) The chip formation kinematics module, which computes the fundamental parameters such as strain, strain rate and characteristic time.

2.) The stress module, which computes and updates the shear stress in each shear zone.

3.) The resolving module, which provides the resultant forces for the output.

In the first module, equations 5-11 are used to provide the deformation data. The second purpose is to establish the deformation time, and dynamically discretized it so that the resulting numerical integration schemes (particularly in the energy module) are fine enough so that no erroneous data is produced. It was noted during the preliminary development of the model that the time step (in essence the strain increment) must be fine enough to provide a continuous function for computing the energy of deformation. Essentially, this module determines the initial and boundary conditions for cutting.

Once the initial and boundary conditions are established, the data is passed to the stress module where the material is numerically deformed. This is where the constitutive law provides the cutting condition specific flow stress. The dynamic temperature is computed in this segment. The stress is then further processed to resolve them into the tool coordinate system.

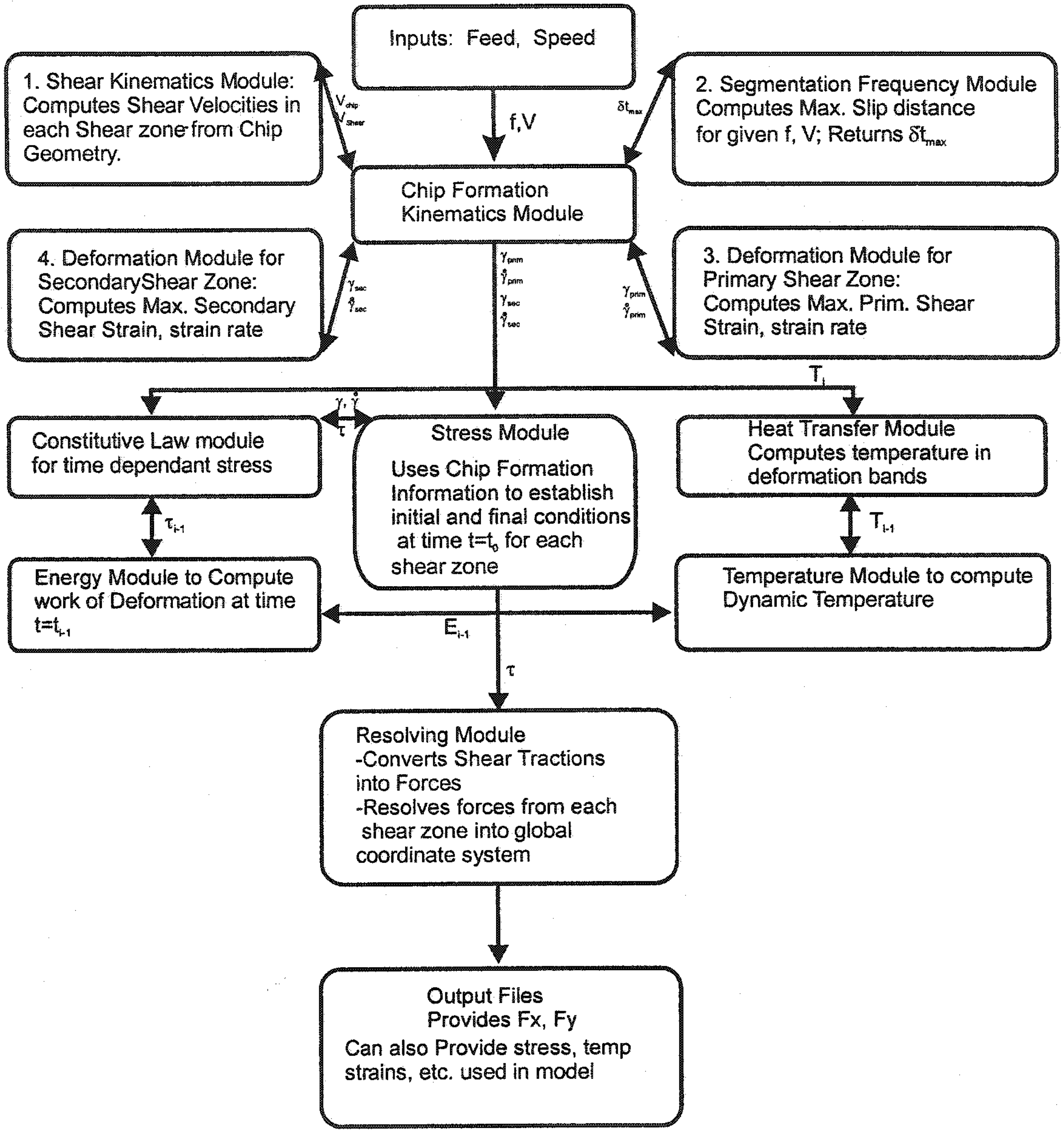

Figure 5.20. Schematic representation of the orthogonal force modelling methodology.

5.5 Verification of Results

Due to the unique formulation of the presented force model, verification proved to be a challenge. The question as to how can a model based on shear stress be verified to be accurate, was imposed. It was concluded that several features of the model needed to be verified. First, the constitutive law must be verified at the presented strains and strain rates during cutting. Finite Element Methods (FEM) have been recently employed to predict and verify models of cutting processes. It was thus concluded that the constitutive law should produce reasonable results FEM. Second, the force model should provide a reasonable representation of the actual cutting force signature. Third, the predicted temperatures associated with the cutting of AISI D2 tool steel should be gauged. It is thus the purpose of the present section to address these issues.

5.5.1 Verification of the Constitutive Law for Machining

Verification of the force model was achieved by comparing the predicted output with the results of finite element analysis (El-Wardany et.al, 2001) as well as the measured experimental forces. To examine the accuracy of the constitutive law developed in (Becze et.al, 2000), an orthogonal cutting process of hardened D2 tool steel material (using polycrystalline cubic boron nitride (PCBN) tools) was simulated using a commercial finite element package. Figure 5 illustrates the geometry and boundary conditions used for the finite element model. The finite element procedure presented to verify the results of this investigation was performed according to (El-Wardany et.al, 2001). The assumptions used in the finite element analysis are as follows:

- 2-D simulation was used with large strain theory
- Updated Lagrangian formulation
- Re-meshing occurs as the tool advances into the workpiece, element distortion, or tool penetration in the workpiece
- Tool advances in the x direction representing the cutting speed in m/sec
- Stick slip friction representation at the tool-chip interface is used.
- Material flow stress is function of strain, strain rate and temperature (Johnson-Cook constitutive equation).

Boundary Conditions:

$T = T_{ambient}$ *On surface S_T*

$-\left(k\frac{\partial T}{\partial n}\right) = h_{ai}(T - T_{ambient})$ *On surface S_I*

$-\left(k\frac{\partial T}{\partial n}\right) = h_c(T - T_{ambient})$ *On surface S_c*

$-\left(k\frac{\partial T}{\partial n}\right) = 0$ *On surface S_a*

A local fine re-meshing module was used. The mesh density was increased in the vicinity of cut, represented by box B1 in figure 5.21. The maximum element size in this area was 0.0127 mm. Increasing the maximum element size in box B2 to 0.0254mm gradually reduced the mesh density. Choosing the maximum element size of the rest of workpiece to be 0.1016 mm further reduced the mesh density. The results of the finite element simulation were verified using the experimental force data.

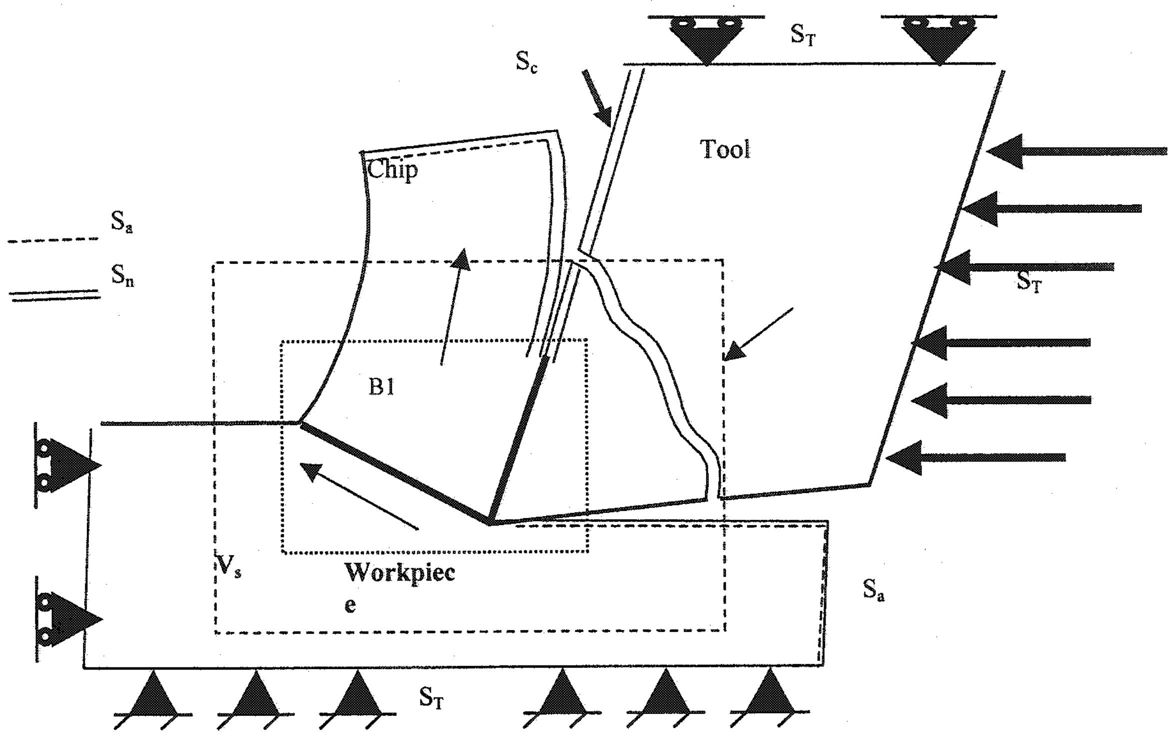

Figure 5.21. Boundary conditions on the tool and workpiece

Figure 5.22 illustrates the results of the finite element simulation performed against the experimental cutting forces. The results presented in by El-Wardany (Becze et.al., 2002) show that simulated cutting force from the FEA analysis correlated well with the experimental force signature using the constitutive relation presented in the present manuscript. The good agreement of the constitutive law from the high strain rate tests presented in chapter 4 combined with the accuracy of the FEA simulation against the experimental forces the proves the accuracy of the constitutive law.

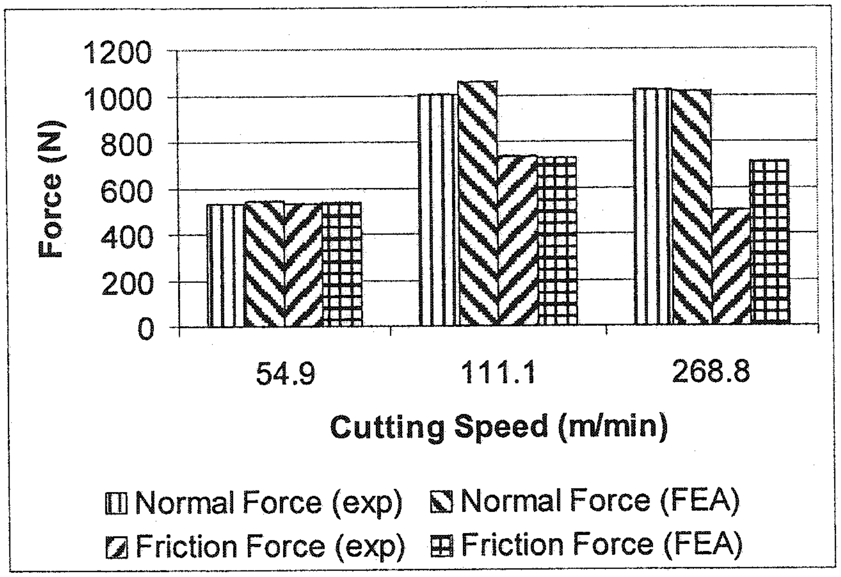

Figure 5.22. The verification of the material constitutive law for AISI D2 tool steel at 62 HRc.

Direct measurement of stress levels are very difficult to obtain from experimentation. The only method available to verify the stress levels produced by the model was to gauge the predicted stress levels against the FEA solution. Since the FEA solution provided an accurate prediction of the cutting force levels, it is assumed that the stress levels are accurate as well. The stress solution obtained from the orthogonal model was gauged against the FEA model to verify the results of the stress levels and is presented in figure 5.23.

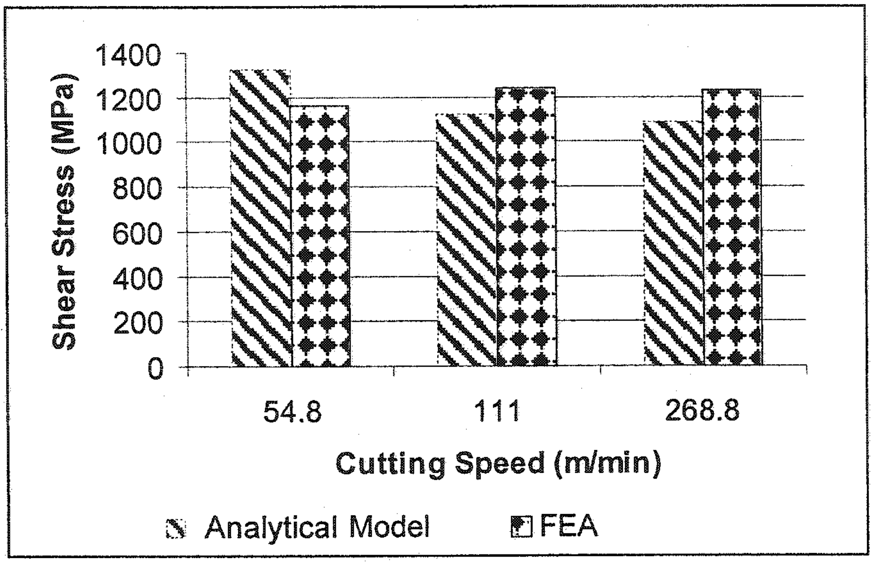

Figure 5.23. Predicted stress levels of orthogonal model against that of the FEA solution as a function of cutting speed and a feed rate of 0.0254 mm/rev.

A final method used for the verification of the orthogonal model was the actual experimental cutting forces. Figure 5.24 shows the predicted resultant force against the experimental values. It can be seen that the difference between the predicted and measured cutting forces was +/- 10%. The good agreement between the predicted and measured forces indicates that the material model accurately represents the flow stress characteristics of D2 tool steel.

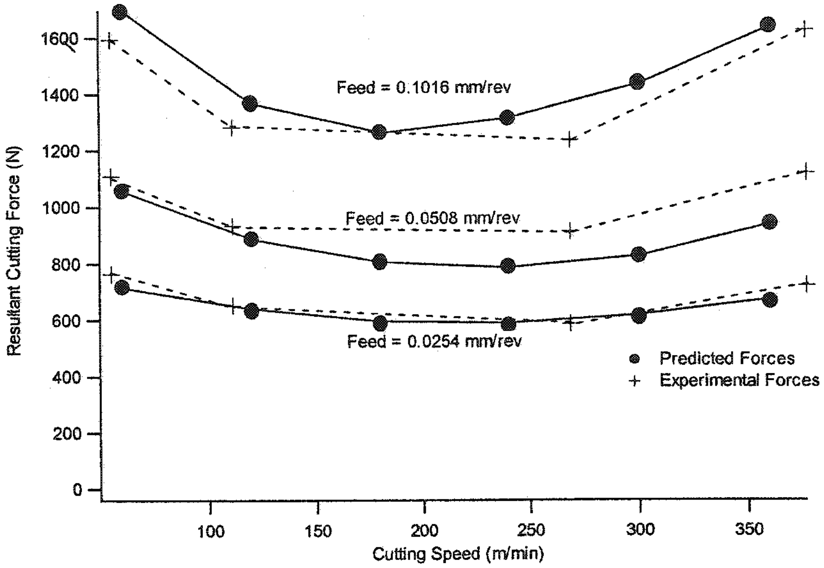

Figure 5.24. Predicted and experimental cutting force signature for machining Hardened AISI D2 tool steel.

A shear angle of 47° was used in this investigation. A high shear angle was necessary to correlate the force values (fx and fy) to the experimental values. Optical microscopy was used to define the parameters illustrated in Figure 5.2. These parameters were used to obtain the constants in equations 8 and 9. The shear angle and contact lengths were directly measured from the chips and tools. The shear angle was obtained by measuring the crack initiation angle and by geometry illustrated by ϕ in figure 5.2. This was done according to the description of the chip formation mechanism given by Shaw (Shaw, 1984) as governed by the evidence from quick stop experiments reported by (Poulachon and Moisan, 2000). The micrographic analysis of the D2 tool steel chips reveals that the shear angle (ϕ) was 47° and relatively independent of cutting conditions and is consistent with those reported in (Vyas and Shaw, 1998). A high shear angle is necessary for the chip length ratio to be greater than 1 reported by Vyas and Shaw when machining hardened steels.

Initially, during the model development, it was found that the cutting forces were very high for high feed rates and high cutting speeds. It was assumed that the contact length was equivalent to the feed rate level because it was convenient to choose a contact length which scaled with the feed rate. It can be deduced from the chip morphology, that a contact length greater than the feed rate cannot occur for large feeds. This would cause the chip to fracture. On the other hand, a contact length less than the feed is possible. Since a shear traction acts on an area to produce a force, it seemed logical to reduce the contact length for high feeds and speeds to reduce the force level. After reducing the contact length to 20% of the assumed value, the force levels on the rake face become more realistic. A cutting test was done (using the same CBN cutting tools from the previous cutting tests except re-sharpened) at a feed level of 0.1016 mm/rev and a cutting speed of 268.8 m/min to allow the tool to marginally wear. Figure 5.25 is an SEM micrograph of the cutting tool.

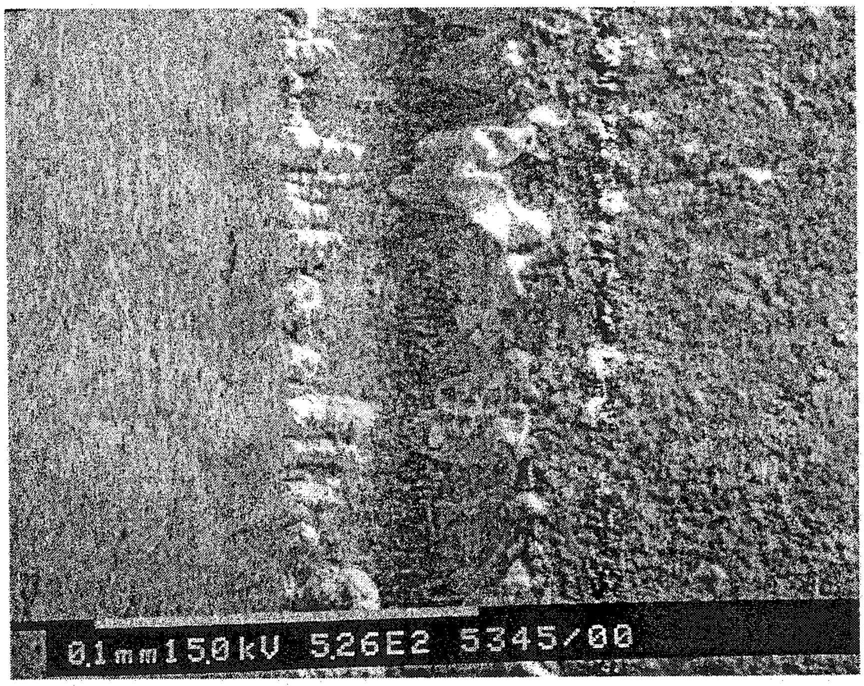

Figure 5.25. SEM image of CBN cutting tool showing wear on the rake face. (V=268.8 m/min, f=0.1016 mm/rev).

Figure 5.25 shows the onset of crater wear on the rake face of the cutter. The crater wear is approximately 30% of the feed level. This indicates that the sliding zone (or a region of high localized stress) is definitely smaller than the prescribed feed. Consider for the moment that wear occurs from the high localized stress on the rake face. The contact length (by definition) *is* this region. Thus, there is a physical basis for using a contact length of 20% the prescribed feed level. It is interesting to note that the necessary contact length for the high cutting speed and large feed simulations correlates very well with the measured value of Tp_{max} from the chip (refer to figure 5.2 for the location of Tpmax). Figure 5.26 illustrates the measured value of Tp_{max} as a function of feed rate. It can be seen that the maximum deformation does not scale linearly with the feed rate. More importantly, notice that the values at the high feed levels approximate the required contact length. Considering the chip formation mechanics, it is not unreasonable to assume that this highly deformed region affects the contact length on the rake face.

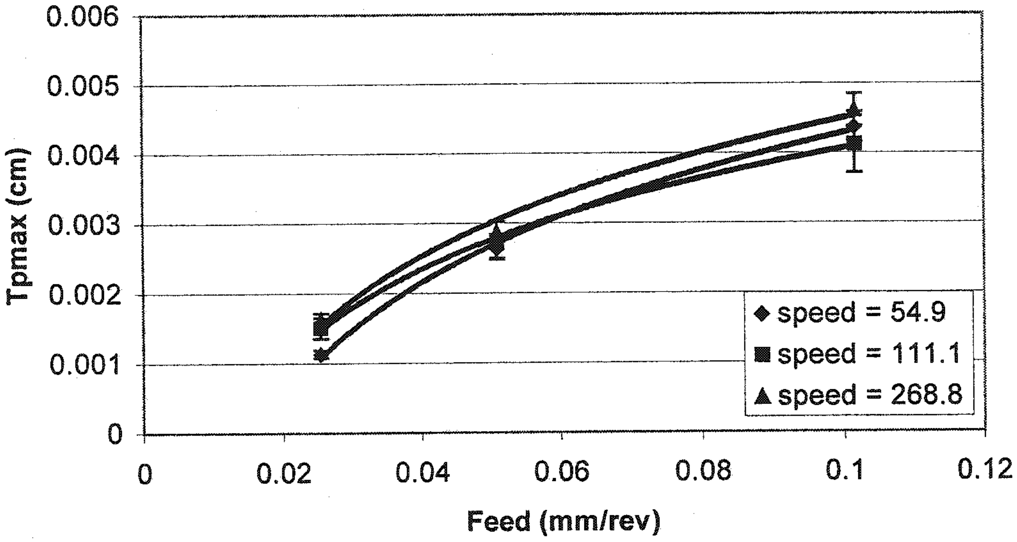

Figure 5.26. Measured value of Tpmax as a function of feed rate from chip microstructure.

The error between the predicted and experimental cutting force is observed to be approximately 10%. The error primarily arose at the higher cutting speeds and is more dominant at the highest feed rates. On the other hand, very good agreement is attained for the lowest feed rate value for all cutting speeds considered. To explain this, it may be instructive to review the strains computed by the force model. Figure 5.27 shows the calculated strains in the primary shear zone as a function of feed for the various cutting speeds.

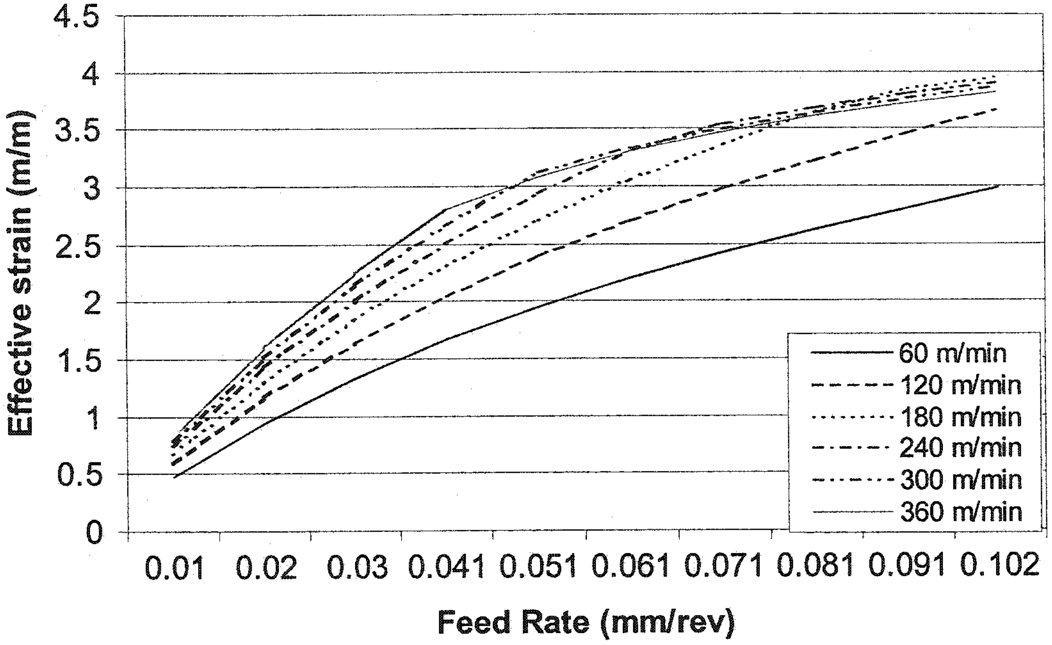

Figure 5.27. Calculated effective strains in the primary shear zone using equation 4.

Figure 5.27 shows that the effective strain in the primary shear zone increases with increasing feed and cutting speed. More important, observe the magnitude of the effective strain. For low prescribed feed values, the effective strain is of the order of 0.5 to 1. Recall that the compressive split Hopkinson bar tests from the previous chapter attained shear strains close to these values. Also, recall from figure 4.6 that the stress levels attained were approximately 1400 MPa in shear. The conditions are very similar in terms of temperature, and effective strain levels. Therefore, it seems reasonable to conclude that the lower feed values will provide a better correlation (as observed from figure 5.24). At higher cutting speeds and feed rates, the strains are approaching very high levels, and therefore small errors in the constitutive law may generate large errors in the simulation. It should seem obvious that the highly coupled nature of the present formulation adds to the complexity of the simulation, and are very difficult to decouple. Recall that at high feed rates and cutting speeds, the contact length was modified. This brought the force level into an acceptable error level. However, this error effect may be numerically coupled with the error introduced by the constitutive law.

The presented formulation requires that the temperature to be dynamically calculated to update the flow stress during the simulation. Figure 5.28 shows the predicted temperature of the model compared to that of the FEA simulation for the primary shear zone temperature. A reasonable correlation is found for this particular cutting condition. The difference in the calculated temperatures in the primary shear zone was 123 °C. The present analytic model predicted 10-15% higher temperatures than the finite element model because the model assumes localised deformation in the primary and secondary shear zone. This assumption appears to be valid due to the fact that little deformation is observed in the grain structure outside the localised shear bands (refer to the micrographs in the previous section). The finite element model however, computed the deformation in the entire chip, which limits the energy of deformation supplied to the shear band, and as a consequence resulted in lower temperatures in the shear zone.

Again, the correlation is good because the calculated shear plane temperatures are similar to those of the high strain rate tests.

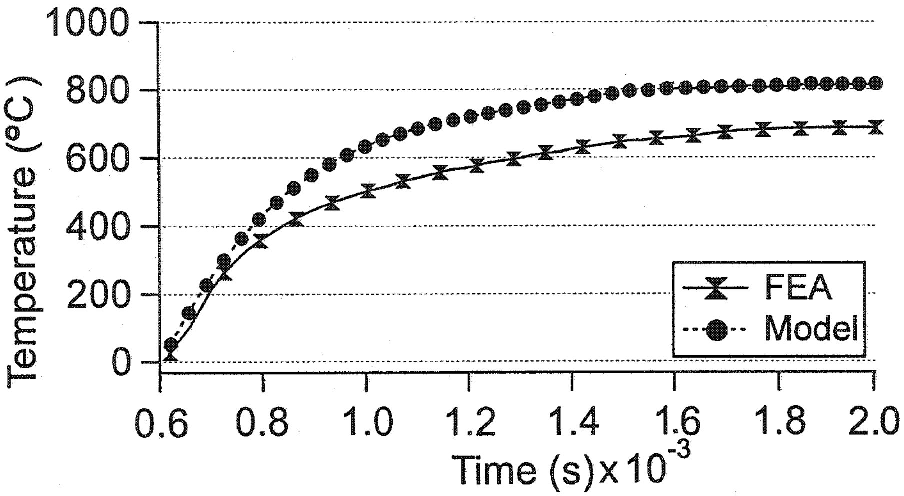

Figure 5.28. Verification of the predicted shear plane temperature for AISI D2 with FEA. (Feed = 0.0254 mm/rev, Speed=58.8 m/min).

Figure 5.29 illustrates the predicted temperature as a function of feed at a cutting speed of 300 m/min. The figure shows the computed trend of the temperature as the feed rate is increased. It is interesting to note that the temperature reaches a maximum level at a feed rate of approximately 0.06 mm/rev. The maximum temperature achieved is slightly over 1000 °C. This appears to be a very high temperature. This value of temperature is reasonable as it was observed that high feed rates (0.0508 mm/rev and above) and fast cutting speeds (268 m/min and above) caused red-hot chips to form during the cutting tests. Although no temperature measurements are available for the shear plane for this material, the chip microstructure shows that high temperatures are attained in the primary and secondary shear zones due to the shearing action by the presence of the transformed shear bands. The chip morphology, shown in figure 5.2, depicts highly localised transformed shear bands. The transformation temperature (A3 temperature) for D2 is approximately 700 °C, and therefore, it can be concluded that the local temperatures in the shear zone reached at least this level. The analytic model predicts temperatures above the A3 temperatures for all cutting conditions that produced fully segmented saw toothed type chips.

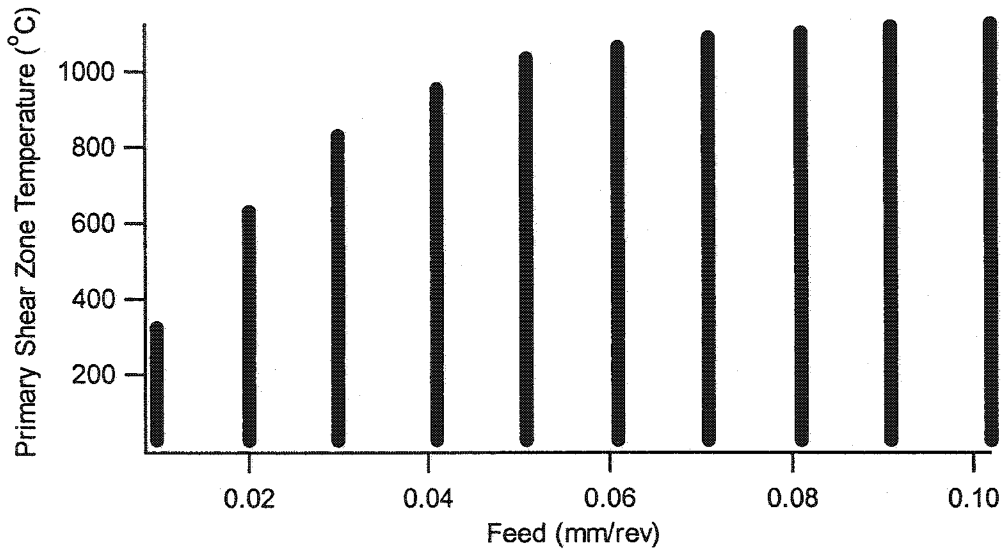

Figure 5.29. Predicted primary shear zone temperature of AISI D2 tool steel.

As a supplement, orthogonal turning tests were performed on SAE 4340 structural steel (HRc 52), and Inconel 718 to verify that the model formulation can be generalized for all materials which produce segmented-saw toothed type chips. The workpiece was a tube of 127 mm outside diameter similar to the set-up for the orthogonal turning tests done on D2. The wall thickness of the tube (width of cut) was 2.54 mm for the SAE 4340. Orthogonal grooving tests were performed on the Inconel 718 specimen with a constant 5.0mm width of cut. The widths of cut were chosen to ensure that plane strain deformation conditions were maintained during chip formation.

The cutting tools used were high volume fraction PCBN for AISI 4340 steel, and SiNw/Al_2O_3 for Inconel 718. All inserts had sharp cutting edge preparation to minimise ploughing forces, -10° rake angle and 0° angle of approach. Forces were measured for each cutting test using a force dynamometer. The chips were collected and mounted, polished and etched to reveal the deformed microstructure for metallurgical investigation.

The same modelling methodology was used to predict the cutting forces for Inconel 718 and SAE 4340. The force model was performed for cutting conditions that produced segmented chips with measurable deformation bands. Figure 5.30 shows that the agreement of the force model with the experimental data was within 15%. The good agreement indicates that the present methodology may be used to predict cutting forces for materials that form saw toothed chips.

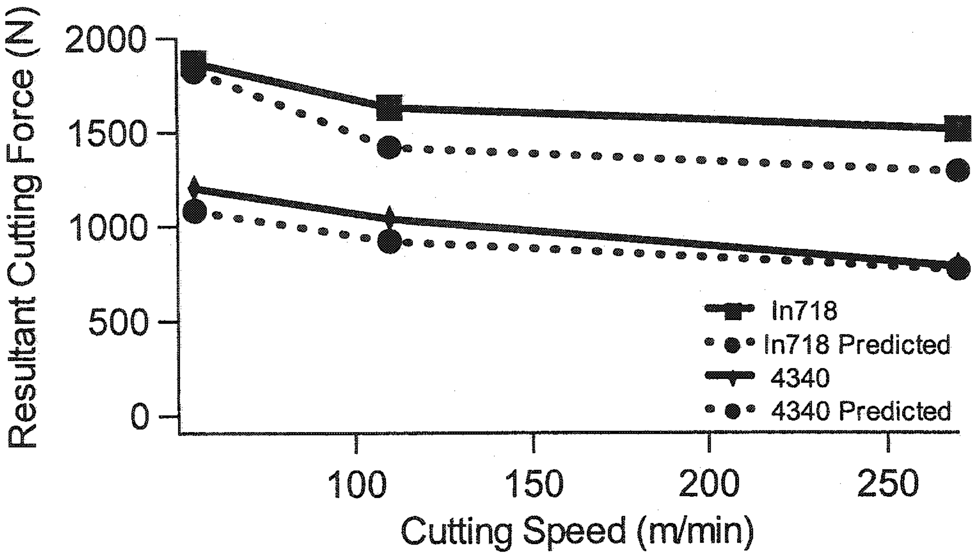

Figure 5.30. Verification of the force model with other 'difficult to cut' materials that produce segmented saw toothed chips.

5.6 Chapter Summary

A constitutive law based cutting force model has been developed for segmented saw toothed type chip formation. The model was used in a time domain simulation to provide cutting forces for feed and speed variations. The chip morphology was used to provide the kinematic data to determine the strains and strain rates used in the model. The model predicts the cutting forces through computation of the average stresses and temperatures encountered during localised chip formation. The model predictions were verified experimentally by showing that the predicted force correlates well with the experimental data as well as using finite element analysis. The finite element analysis was used to verify both the resulting stress levels of the model, as well as the validity of the constitutive law.

The present modelling methodology has been used to predict the cutting forces for several materials that produce segmented saw-toothed chips. The model results were in agreement with the experimental data illustrating that the modelling methodology can be applied in a general manner to materials which form saw toothed chips.

Chapter 6

Oblique Force Model for Ball End Milling

6.1 Introduction

An oblique cutting force model has been developed using the analytic orthogonal force model developed in chapter 3. The force model uses a thermo-visco-plastic material constitutive law to represent the shear stress during deformation of the material. The strains and strain rates used for defining the shear stress were obtained from chip formation and morphology derived from orthogonal cutting tests and have been extended to oblique cutting. A time domain simulation using the in-cut chip geometry to define the chip load area has been developed. The oblique force model was used to verify the orthogonal model by predicting the cutting forces during ball end milling of hardened AISI D2 tool steel. The predicted forces were verified experimentally and showed good correlation.

Generally, mechanistic approaches have been used for force modelling of ball end milling process (Yucesan et.al., 1996, Abrari et.al., 1998, Abrari et.al., 2001, Imani et.al, 1998). These include several mechanistic models focusing on geometric issues (Kline and DeVor, 1983), tool runout (Imani and Elbestawi, 2001), surface errors (Sutherland and DeVor, 1986) etc. However, explicit analytic force modelling based on cutting mechanics has not been addressed. On the other hand, Yang and Park (Yang and Park, 1991) have demonstrated that orthogonal cutting force data may be successfully used in the prediction of the cutting forces of the ball end milling processes. Yucesan (Yucesan et.al., 1996) have provided a semi-mechanistic approach for ball end milling by determining the friction and pressure coefficients along the cutting edge by using the effective cutting force coefficients dependant on the cutter, the flute immersion geometry and the feed rate. These approaches work well in defining the forces yet may deviate from the experimental forces if the cutting conditions change significantly.

The present research provides a method based on the chip formation and morphology obtained from orthogonal cutting tests on hardened AISI D2 tool steel to provide kinematic data of the deformation process. The force model has been validated for materials classified as difficult to cut (i.e. forming saw toothed type chips). The analytic model appears to capture the chip formation mechanism in general, and therefore the concept is not limited to the specific alloy for which the model was derived. The strains and strain rates (derived from the chip morphology) are used with a thermo-visco-plastic constitutive law (Becze et.al., 2000) to define the shear stress associated with the cutting process. The analytic orthogonal model developed in (Becze et.al., 2002) has been extended to an oblique configuration defined by the ball end milling process. The merits of the orthogonal model are based on the fact that the representation of the cutting force is defined in terms of cutting speed and undeformed chip thickness to provide the flow stress of the material during cutting. Variation of the undeformed chip thickness both axially and radially (due to geometric effects associated in milling), as well as cutting speed variations in the axial direction (due to the variation of the effective radius), of the ball end milling process provides a significant challenge for force modelling. The present model accounts for these variations due to the unique formulation defining the cutting process.

The cutting forces are computed using a time domain simulation that computes the instantaneous temperature that actively determines the flow stress (combined with the strain history and the strain rate) of the material in the primary and secondary shear zones. Using this methodology, the cutting process is uniquely defined by the cutting conditions, namely tool geometry, undeformed chip thickness and cutting speed to determine the flow stress during deformation (and hence the cutting force). Extension of the orthogonal force model to an oblique configuration utilized the same kinematic representation of the cutting process except that the chip flow direction has been incorporated as well as the geometric aspects of the ball end milling process. The oblique force model has been experimentally verified for ball end milling of hardened AISI D2 tools steel.

6.2 Force Model Development

An analytic orthogonal cutting force model (Becze et.al., 2002) has been used to develop a force model for ball end milling cutters when machining hardened AISI D2 tool steel. The orthogonal force model is applied to an oblique geometry that represents a ball nose end mill. The basic formulation of the oblique model is to discretize the cutting edge into differentially small areas. The orthogonal shearing traction for each consecutive shear zone is then applied to the differential area segments defining the cutting edge which intersect the workpiece. From this, the cutting forces can be resolved into the tool coordinate system.

6.3 Review of Orthogonal Force Model Concepts.

The analytic force model implements a constitutive law based shear stress model that depends on the strain, strain rate and temperature generated during saw toothed chip formation. It is assumed that deformation occurs in two distinct shear zones (classically the primary and secondary shear zones) as illustrated in Chapter 5, figure 5.15. The present approach models the shear tractions as functions of undeformed chip thickness (f) and cutting speed (V) for each consecutive shear zone. The method for computing the force (F) in each shear zone is represented by:

$$F = \tau(\gamma(f,V), \dot{\gamma}(f,V), T) * dA(f,V)) \qquad (1)$$

where τ is the governing constitutive equation (Johnson-Cook formulation) dependant on strain, strain rate and temperature that defines the flow stress of the material, and now dA(f,V) is the *differential area* on which the shear traction occurs, expressed as a function of feed (f) and cutting speed (V). Recall that the strains and strain rates are defined as functions of undeformed chip thickness (f) and cutting speed (V).

The Johnson-Cook constitutive law (Johnson and Cook, 1983) developed for high strain rates and temperatures is represented by (equation 2):

$$\sigma = (A + B\varepsilon^{n})(1 + C\log(\frac{\dot{\varepsilon}}{\dot{\varepsilon}_{o}}))(1 - \left(\frac{T - 298}{T_{M} - 298}\right)^{m}) \qquad (2)$$

where A,B,C,n,m are material constants, ε is the effective strain, $\varepsilon^{\bullet}$ is the effective strain rate, T and T_M are the absolute temperature during deformation and melting temperature of the alloy respectively.

The governing constitutive law requires strain, strain rate and temperature as independent variables to model the flow stress during chip formation. The strains and strain rates were expressed as functions of process parameters, namely tool geometry, undeformed chip thickness and cutting speed. The following defines the governing strains and strain rates used in the present analysis.

The formulation of the strain is the same as in the previous chapter, however, the geometric transformation into oblique cutting must be made. Using the definition of shear strain in metal cutting theory (Shaw, 1984), the maximum strain in the primary shear zone for segmented saw toothed chips may be defined by equation 4 as:

$$\gamma_{\text{prim}} = \frac{\Delta d_{\text{prim}}}{\Delta t_{\text{prim}}} \tag{4}$$

where Δd_{prim} is the slip distance (a function of shear angle and segmentation frequency), and Δt_{prim} is the gauge length of the primary shear band (obtained from chip micrographs). The strain rate in the primary shear zone can be defined by equation (5) as:

$$\dot{\gamma} = \frac{V_S}{\Delta t_{\text{prim}}} = \frac{\cos\alpha_e}{\cos(\phi - \alpha_e)} \frac{V}{\Delta t_{\text{prim}}} \tag{5}$$

where V_s is the shear velocity between the chip and the workpiece, ϕ is the shear angle (determined experimentally from chip micrographs as 47°), and α_e becomes the *effective* rake angle. The maximum strain in the secondary shear zone is dependant on the deformed band thickness (Δt_{sec}) as well as the contact length (C_L) of the chip, and is defined by equation (6) as:

$$\gamma_{\text{sec}} = \frac{C_L}{\Delta t_{\text{sec}}} \tag{6}$$

The strain rate in the secondary shear zone can be computed from the cutting speed (V) and the secondary shear band thickness (Δt_{sec}) using equation (7):

$$\dot{\gamma} = \frac{V_C}{\Delta t_{sec}} = \frac{\sin\phi}{\cos(\phi - \alpha_e)} \frac{V}{\Delta t_{sec}} \tag{7}$$

It should be observed that the formulation of the kinematic definitions is the same as the previous chapter only with minor differences in geometry.

6.4 Time Domain Simulation for Ball End Milling

A time domain simulation similar to the one developed in the previous chapter is presented. The oblique simulation as with the orthogonal simulation ensures that the final strain levels are compatible with the segmentation frequency (i.e. slip distance). The strain rates obtained from equation (5) and (7) allow for the computation of the strain path history in time, $\gamma(t)$, for each shear zone in the time domain until the maximum strain state governed by equations (4) and (6) is reached. A constant strain rate is assumed (computed from equation (5) and (7)) for each shear band, and thus, a linear strain path is taken as a function of time. For the present purpose, the differential increment in strain $d\gamma$ is obtained using the discretized time step dt and is obtained from equation 10a:

$$d\gamma = \dot{\gamma} dt \tag{10a}$$

To ensure compatibility, the strain level at any time increment dt must follow the strain path in time governed by equation 10a. For the present simulation purposes, the time increment was kept constant throughout the entire solution for the strain along the cutting edge. This was done so that the strain compatibility was maintained over the entire cutting edge length between each differential area. The maximum shear strain γ_{max} (f,V) must be bounded by the chip microstructure, and therefore must be compatible with the observed chip morphology for various cutting conditions. This was done using by verifying that equation 10b is followed:

$$\gamma(t) = \gamma_{max}\left(\frac{1}{\nu(f,V)} - \sum_{i=0}^{i} dt_i\right)_{dA_i} \quad \text{where } 0 \le t \le \frac{1}{\nu(f,V)} \qquad (10b)$$

Again, equation 10b ensures that compatibility is maintained for each chip formation cycle and is consistent over each differential area dA_i. This is accomplished by noting that $1/\nu$ is defined as the period of segmentation and hence one saw toothed chip cycle to a time of t in increments of dt. Equation 10b) thus places a limit to the maximum strain achieved per saw-tooth cycle.

The formulation of the time dependant temperature is the same as previously outlined in chapter 5. Thus, the method of calculating the shear tractions is based on the same recursive energy method as in chapter 5 using the temperature as a necessary input parameter derived from the work of deformation.

The constitutive representation of the flow stress computed to the maximum strain level was used to convert the shearing traction to a force by applying the traction on the differential dynamic shear plane area dA(t) and the contact area of the tool/chip interface. Since the dynamic shear plane area changes as the chip localises, the shear plane area for each time increment (dt) was computed using equation 12:

$$dA_{\text{primary}}(t) = db\left(\frac{f}{\sin\phi} - \frac{\cos\alpha_e}{\cos(\phi-\alpha_e)}V \cdot dt\right) \qquad (12)$$

where db is the width of the discretized in-cut segment along the tool edge. The secondary shear zone traction was converted to a force by using the contact length (C_L) and the width of cut db by using equation 13:

$$dA_{\text{secondary}}(t) = db * C_L . \qquad (13)$$

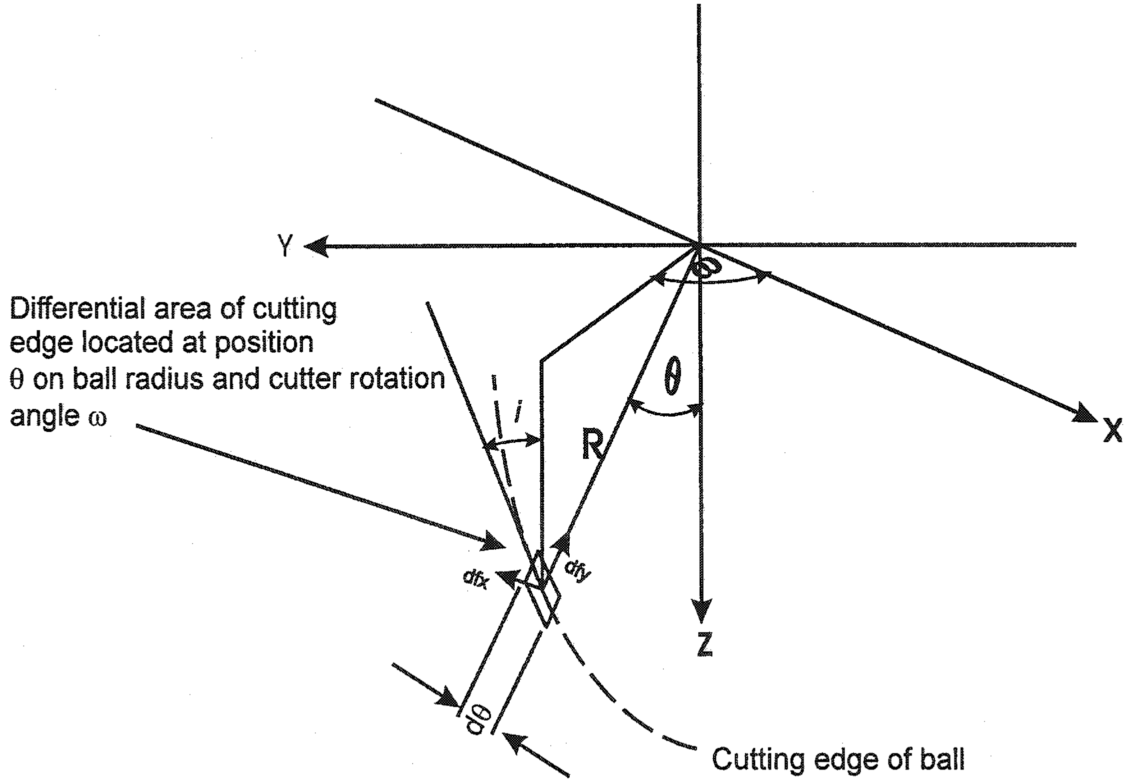

Figure 6.1. Schematic representation of the geometric orientations in modelling the ball end mill geometry

For the present investigation, the oblique differential area defined by the radial width of cut and axial immersion was determined from the tool geometry. The tool was discretized according to figure 6.1. The axial division was performed from the tool tip with respect to the centre of the ball end mill cutter and the positive Z-axis by constant increments. Recall that the arc length S can be represented as $r\theta$ if θ is in radian measure. Therefore an incremental angle $d\theta$ (in radian measure) will produce a differential width of cut (db) in terms of the ball end mill radius R and is expressed by equation 14:

$$db = Rd\theta \qquad (14)$$

Thus, for a fixed cutter radius, the differential area will remain constant for each axial position θ, along the cutting edge. The inclination angle (i) of the ball end mill (in the present case, a constant lead angle of 10^{o}) will cause the rake angle to change. It was previously stated that orthogonal cutting is a two dimensional process. Oblique cutting occurs when the cutting tool is oriented to a non-zero angle of approach, which causes the chip flow angle to change. Figure 6.2 shows and oblique cutting process compared to an orthogonal process and its effects. A change in the approach angle (i) in metal cutting causes the chip flow angle (η_c) to change. Stabler has shown that a relation exists between the effective rake angle (α_e) and the inclination angle (i), the chip flow angle (η_c) and the actual rake angle (α). This is represented by equation 15 a). As a first approximation, Stabler showed that the chip flow angle (η_c) is approximately equal to the inclination angle (i) and therefore equation 15 b) follows:

$$\sin(\alpha_e) = \sin(\eta_C)\sin(i) + \cos(\eta_c)\cos(i)\sin(\alpha) \qquad (15a)$$

$$\sin(\alpha_e) = \sin^2(i) + \cos^2(i)\sin(\alpha). \tag{15b}$$

Direct measurements of the chip flow angle are unavailable. Therefore, it is assumed that the chip flow angle (η_c) coincides with the direction defined by the effective rake angle for the present investigation.

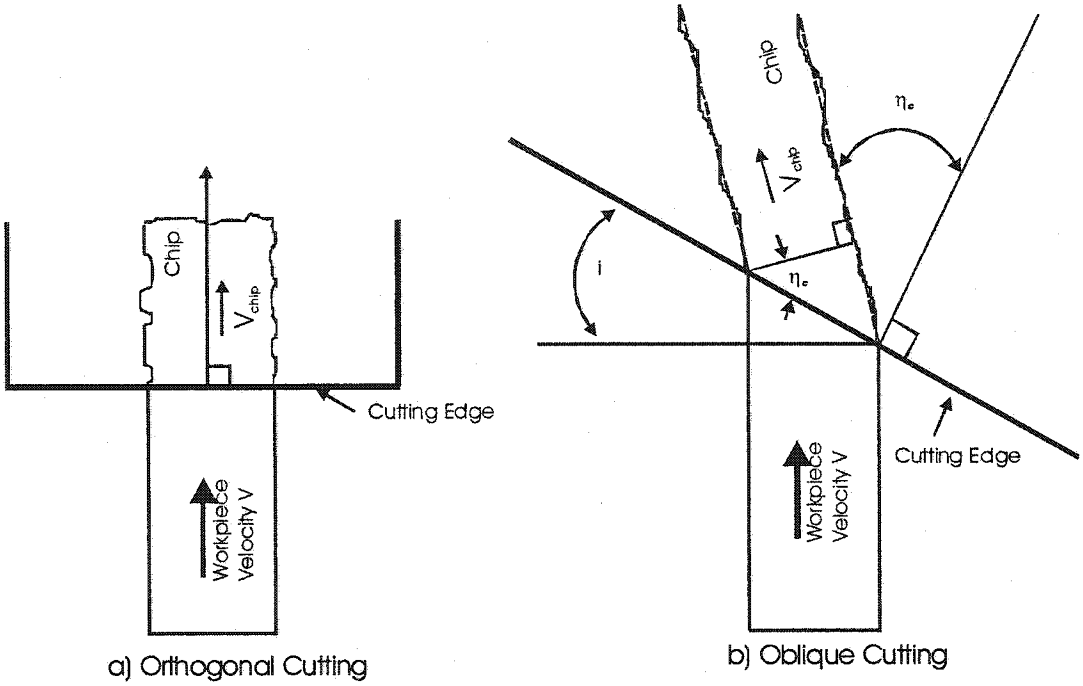

a) Orthogonal Cutting

b) Oblique Cutting

Figure 6.2. Plan view comparison of an a) orthogonal cutting configuration and b) oblique cutting showing the effect of changing the approach angle of the cutting edge.

The shear tractions (notably stresses) obtained from each shear zone is used to compute the force by applying the resulting traction acting on the differential areas of equations 12 and 13. Thus df_{prim} and df_{sec} are represented by equations 16 a) and 16 b):

$$\mathrm{df_{prim}} = \tau_{\mathrm{prim}} \mathrm{dA_{primary}}(t) = \tau_{\mathrm{prim}} \mathrm{db}\left(\frac{f}{\sin\phi} - \frac{\cos\alpha_e}{\cos(\phi-\alpha_e)} V \cdot dt \right) \tag{16a}$$

$$\mathrm{df_{sec}} = \tau_{\mathrm{sec}} \mathrm{dA_{secondary}}(t) = \tau_{\mathrm{sec}} \mathrm{db} * f \tag{16b}$$

Recall that for small feeds, it is reasonable to assume that the contact length is equal to the undeformed chip thickness. This substitution was made in equation 16 b) for the contact length.

The resulting differential forces ($\mathrm{df_{prim}}$, and $\mathrm{df_{sec}}$) calculated from each shear zone are then resolved into the tool co-ordinate system (dfx and dfy) for each differential area by using equations 17 a) and 17 b):

$$\mathrm{dfx} = \mathrm{df_{prim}} \cos(\alpha_e) + \mathrm{df_{sec}} \sin(\alpha_e) \tag{17a}$$

$$\mathrm{dfy} = \mathrm{df_{prim}} \sin(\alpha_e) + \mathrm{df_{sec}} \cos(\alpha_e) \tag{17b}$$

where $\mathrm{df_{prim}}$ is the primary shear zone force, and $\mathrm{df_{sec}}$ is the secondary shear zone force. The conversion to 3-D forces as a function of axial position (θ) of the differential area and tool position measured from the positive X-axis in the workpiece coordinate system (ω) was computed from the following equations (18 a-c):

$$\mathrm{dFx} = -\mathrm{dfx}\sin(\omega) + \mathrm{dfy}\cos(\omega)\sin(\theta) \tag{18a}$$

$$\mathrm{dFy} = \mathrm{dfx}\cos(\omega) + \mathrm{dfy}\sin(\omega)\sin(\theta) \tag{18b}$$

$$\mathrm{dFz} = \mathrm{dFy}\cos(\theta) \tag{18c}$$

The differential forces (dFx, dFy, dFz) are then summed axially from the minimum point of engagement h_{min} to the maximum point of engagement h_{max} ($d\theta = 1$ degree) for each tool position ω.

In ball end milling, the chip geometry depends on the axial and radial position of the cutting tool. This is because the chip thickness varies both axially and radially due to the circular configuration of the swept cutting volume. From figure 6.3 it can be seen that the chip thins out in both directions. Thus, it is of critical importance to know several features when milling. 4 or 5-axis machining is required when milling hardened tool steels to prevent the nose from coming in contact with the workpiece. In order to do this, the workpiece must be tilted off the planar axis of the tool by the tilt angle λ. By imposing a tilt angle, the minimum point of engagement (h_{min}) moves up the cutting edge away from the nose. The maximum point of engagement (h_{max}) is a function of the axial depth of cut (ADC). Clearly, the chip starts at zero effective thickness (for small λ) located at h_{min} and continues to increase until it reaches the position of h_{max}. In the radial plane, the uncut chip thickness is a function of the radial position (ω) of the cutting edge (or tooth edge). The maximum chip thickness is a function of the radial width of cut where the cutter intersects the workpiece. Thus, in order to model the ball end milling process, these positions must be analytically determined.

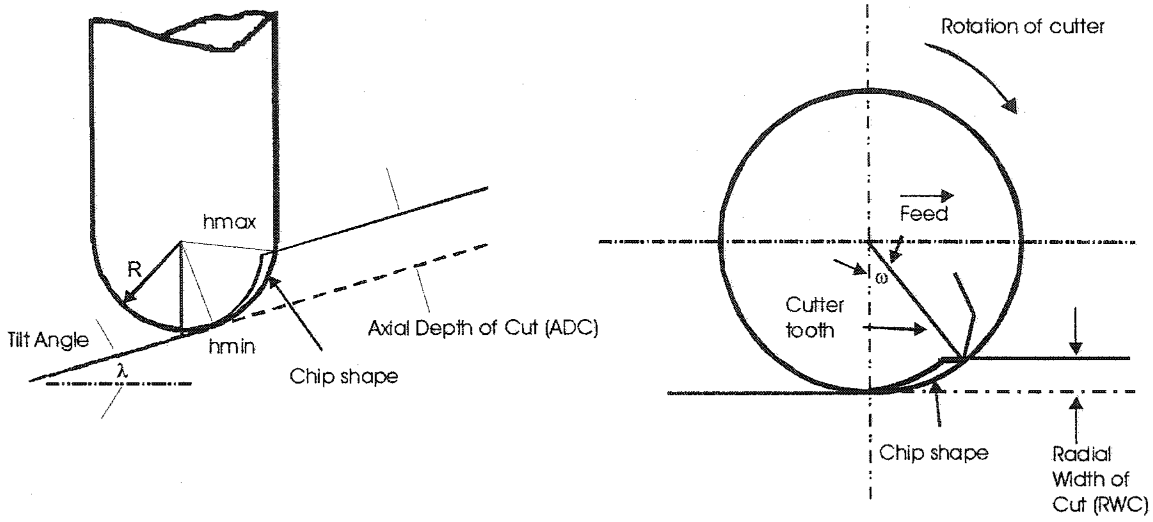

a) axial view in feed direction

b) Radial view in radial plane

Figure 6.3. The chip geometry for ball end milling showing a) the axial chip thickness variation and b) the radial thickness variation.

The in-cut heights h_{min} and h_{max} were determined by modelling the tool-workpiece intersection using a commercial CAD software package. The tool was modelled according to the tool geometry used in the experiments. The workpiece was modelled by removing a cylindrical volume to simulate an entire tool pass. To model the in-cut segment, a cylinder with a spherical end was removed offset by one radial width of cut. The tool was positioned one feed unit ahead of the previous cut. The tool was then rotated by one-degree increments about the axial axis vector and the tool-workpiece intersection was computed in terms of in-cut height as a function of the tool rotation. Thus, for each radial tool angle ω, the minimum and maximum in-cut heights bounds were computed. Figure 6.4 illustrates the measured tool immersion into the workpiece.

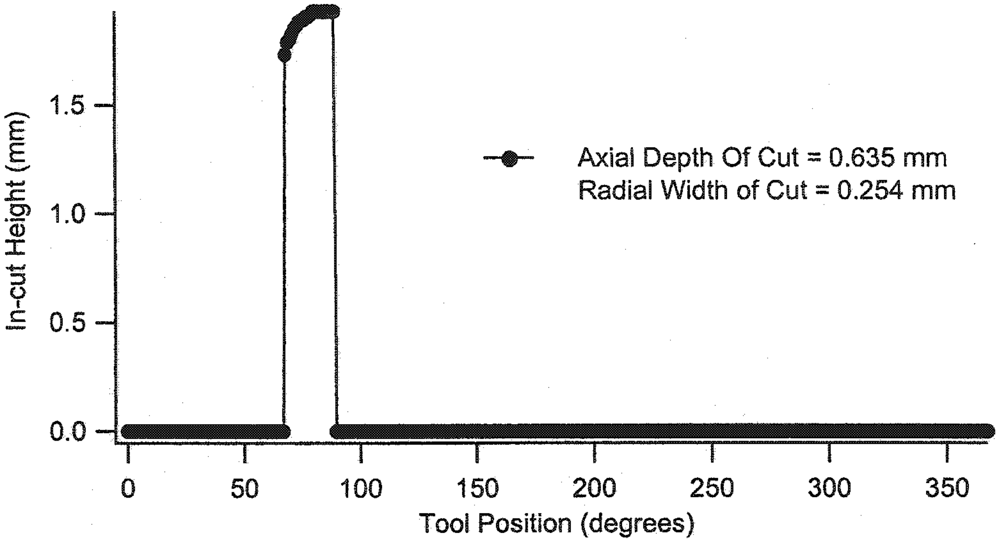

Figure 6.4. The position of the tool-workpiece intersection and the maximum in-cut height for the cutting conditions outlined. The tilt angle was 10 degrees for a 12.7 mm diameter ball nose end mill.

The number of discrete steps n (for $d\theta=1$) was determined from the angular displacement that was subtended by h_{min} and h_{max} in the axial plane. Figure 6.4 provides the maximum point of engagement (h_{max}). The minimum height of the tool intersection is a function of the tilt angle (λ) of the workpiece. Thus for a ball end milling cutter of radius R and a workpiece tilt angle λ, the minimum in-cut height is obtained from equation 19:

$$h_{min} = R(1-\cos(\lambda)) . \qquad (19)$$

By definition, h_{max} is a relative displacement along the cutting edge. The angular position needs to be computed so that the simulation is provided with an angular upper bound (θ_{max}). The maximum in-cut angle, θ_{max} (recall θ_{max} is in the axial direction), for each radial tool position ω was determined using equation 20:

$$\theta_{max} = \cos^{-1}\left(\frac{R}{R - h_{max} - h_{min}}\right) \tag{20}$$

where R is the radius of the cutter. Clearly, $\theta_{min} = \lambda$ and thus, the number of increments, n_{max}, for each tool position is computed by using equation 21:

$$n_{max} = \frac{\theta_{max} - \lambda}{d\theta}. \tag{21}$$

The summation of the forces follows from equation 21 for each differential area. The total force in the workpiece coordinate system (Fx, Fy, Fz) is computed as the sum of the differential forces evaluated at each position θ_n (equations 22 a-c):

$$Fx = \sum_{n=1}^{n=n_{max}} dFx\Big|_{\theta_n} \tag{22a}$$

$$Fy = \sum_{n=1}^{n=n_{max}} dFy\Big|_{\theta_n} \tag{22b}$$

$$Fz = \sum_{n=1}^{n=n_{max}} dFz\Big|_{\theta_n} \tag{22c}$$

It should be noted here that the kinematic properties used in equations 4-7 for computing the forces require the undeformed chip thickness (f) as well as the cutting speed (V). In ball end milling, neither of these quantities remains constant. Figure 6.5 shows the variation of the uncut chip thickness for a feed level of 0.1016 mm/tooth in the axial direction only. The chip thickness behaviour in the radial direction is similar to the axial direction and therefore, is geometrically coupled. Figure 6.6 shows the cutting speed variation along the cutting edge of the ball. The undeformed chip thickness varies in both the axial and radial directions. Thus, for kinematic equations from chip formation to be valid for ball end milling, expressions relating the cutting speed and instantaneous chip load must be obtained. The expression (equation 23) used for determining the undeformed chip thickness f as a function of the radial tool position ω, the axial position θ, and the prescribed feed per tooth level f_o as:

$$f = f_o \cos(\omega) \sin(\theta) \tag{23}$$

The effective cutting speed (V_{eff}) is dependant on the effective working radius, which in this case is a function of axial position. Thus, the location of the differential area positioned on the cutting edge of the ball end mill defines the effective radius. For any axial tool position θ_n $\{1 \leq n \leq n_{max}\}$ the effective cutting speed is computed by equation 24 (the correlation is graphically represented in figure 6.6):

$$V_{eff} = 2\pi NR \sin(\theta_n) \tag{24}$$

where N is the rotational speed of the cutter.

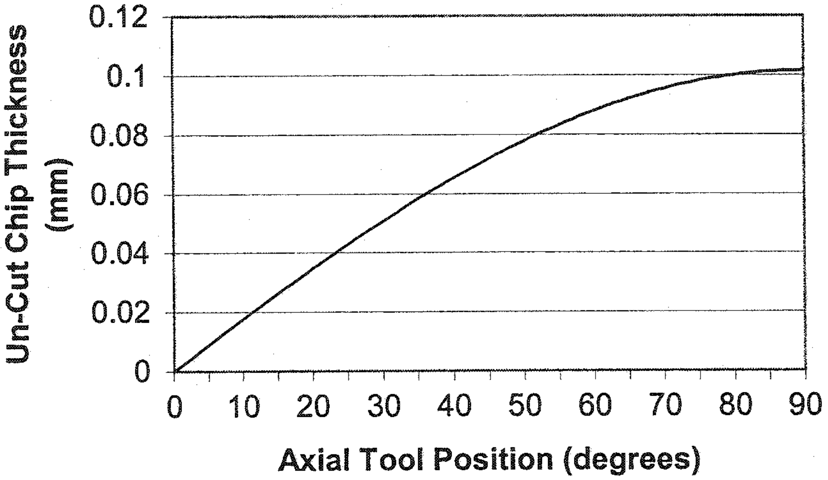

Figure 6.5. Variation of uncut chip thickness for a commanded feed level of 0.1016 mm/tooth.

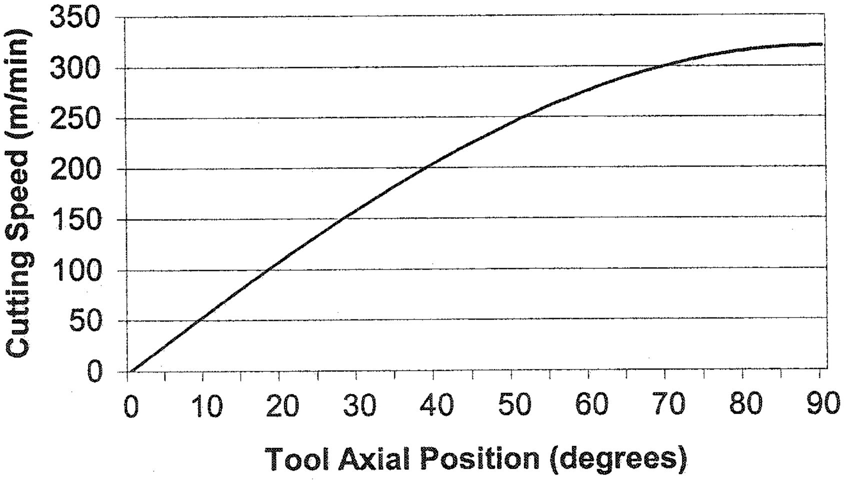

Figure 6.6. Variation of effective cutting speed for a maximum cutting speed of 320 m/min.

6.5 Results for Ball End Milling

Ball end milling imposes variations in both uncut chip thickness as well as cutting speed. Thus, the ball end milling process provides a challenging platform to test the validity of the orthogonal force model. The justification of formulating the orthogonal force model as a function of feed and speed as primary inputs, analysing the chip formation and representing the key kinematic parameters also as a function of feed and speed should now seem apparent. The end result was a unique modelling strategy for ball end milling.

The results of the analytic oblique force model for various conditions are illustrated in figures 6.7 and 6.8. The predicted results show good correlation with the experimental forces suggesting that the resulting stress level predictions are reasonable for the strain and strain rate conditions modelled in the milling simulation. It must be stressed here that the kinematic data used in the simulation was obtained from chips collected during **orthogonal** cutting tests. The significance here is that the undeformed chip thickness in milling is substantially less than the constant chip thickness of the orthogonal turning tests (while the cutting speeds were well within the limits tested in (Becze et.al.,2000)). At small undeformed chip thickness levels, the chip formation mechanism (due to variation in the resulting strain and strain rate levels) could very well influence the flow stress of the material. From this fact, extrapolation of the turning data was in question. However, the good correlation between the predicted and experimental cutting force, shows that for the given conditions the chip formation process remains the same. Further, the similarity between the chip formation mechanism between the orthogonal chips and the chips produced from ball end milling cutting tests is also a good indication that modelling formulation can be extrapolated to milling.

The resolution of the cutting force (in terms of magnitude in the X, Y, Z global coordinate system) closely resembles the experimental force signature. This was accomplished with ***no explicit force calibration derived*** from actual cutting tests. The results were obtained based on the chip formation and chip morphology from orthogonal cutting conditions. Figure 6.9 illustrates the resultant cutting force for the above cutting conditions. The force model shows good correlation with variations in cutting conditions. For instance, the difference in cutting conditions illustrated in figures 6.7 and 6.8 is that the feed rate (i.e. the feed per tooth) is halved. The predicted force does not scale linearly with feed rate. This is because the analytic representation of the shearing traction is dependant on the strain level, which is dictated by chip formation. A typical chip is shown in figure 6.10 from ball end milling tests on D2 tool steel. Note the segmented morphology. The orthogonal turning tests showed similar scaling with feed (Becze et.al, 2002). However, since the shear angle remains constant in the analysis, the force variation would be expected to scale in a linear fashion as well. The fact that it does not indicates that the stress distribution is affected by more fundamental parameters; namely strain, strain rate and temperature. Thus, the accuracy of the force model can be partly attributed to the unique methodology of obtaining the strains and strain rates during chip formation as functions of cutting speed and undeformed chip thickness from the chip morphology.

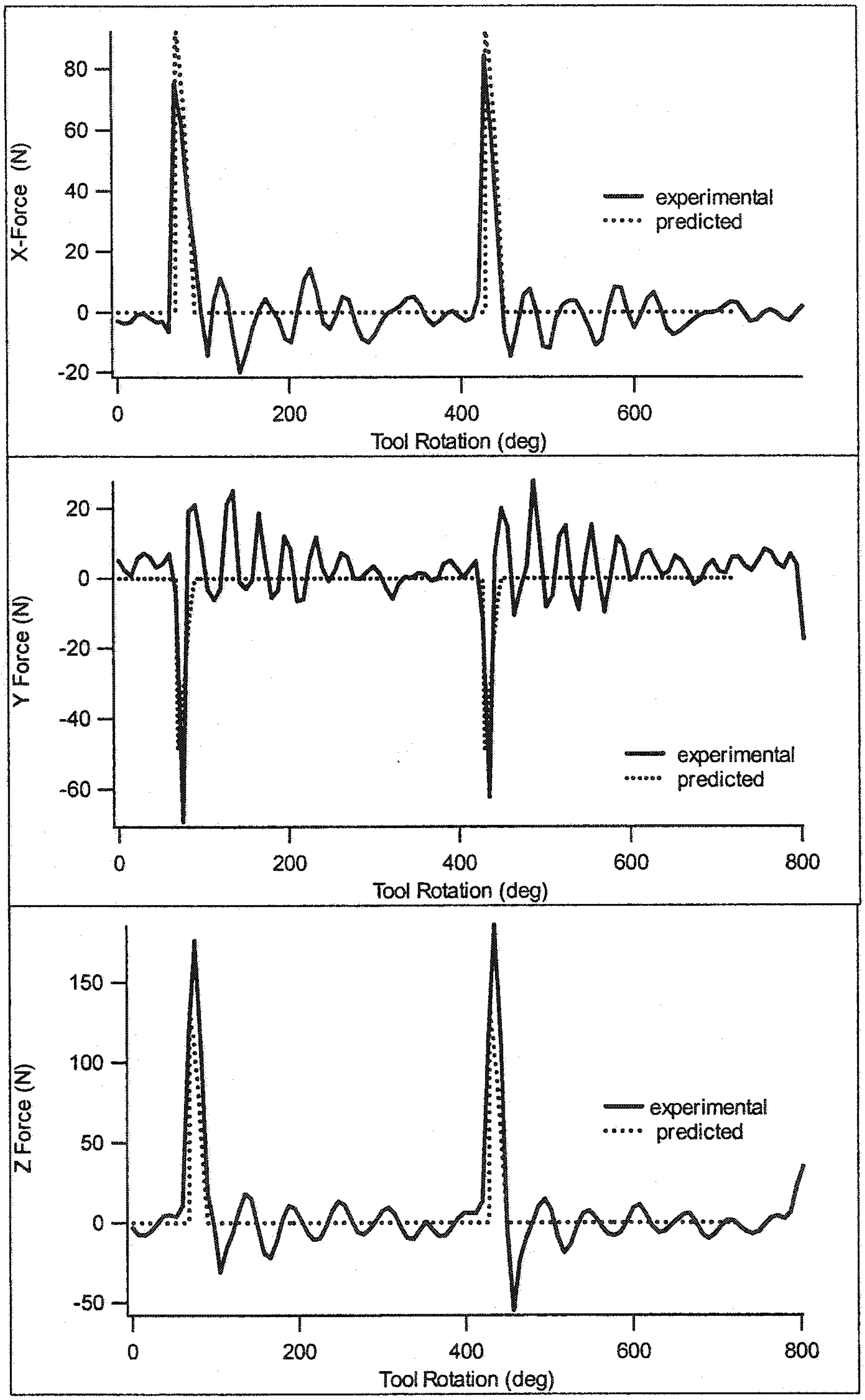

Figure 6.7. Predicted force compared with experimental force data for a feed rate of 0.0508 mm/tooth (N=10000 RPM, ADOC = 0.635 mm, RWOC = 0.25 mm).

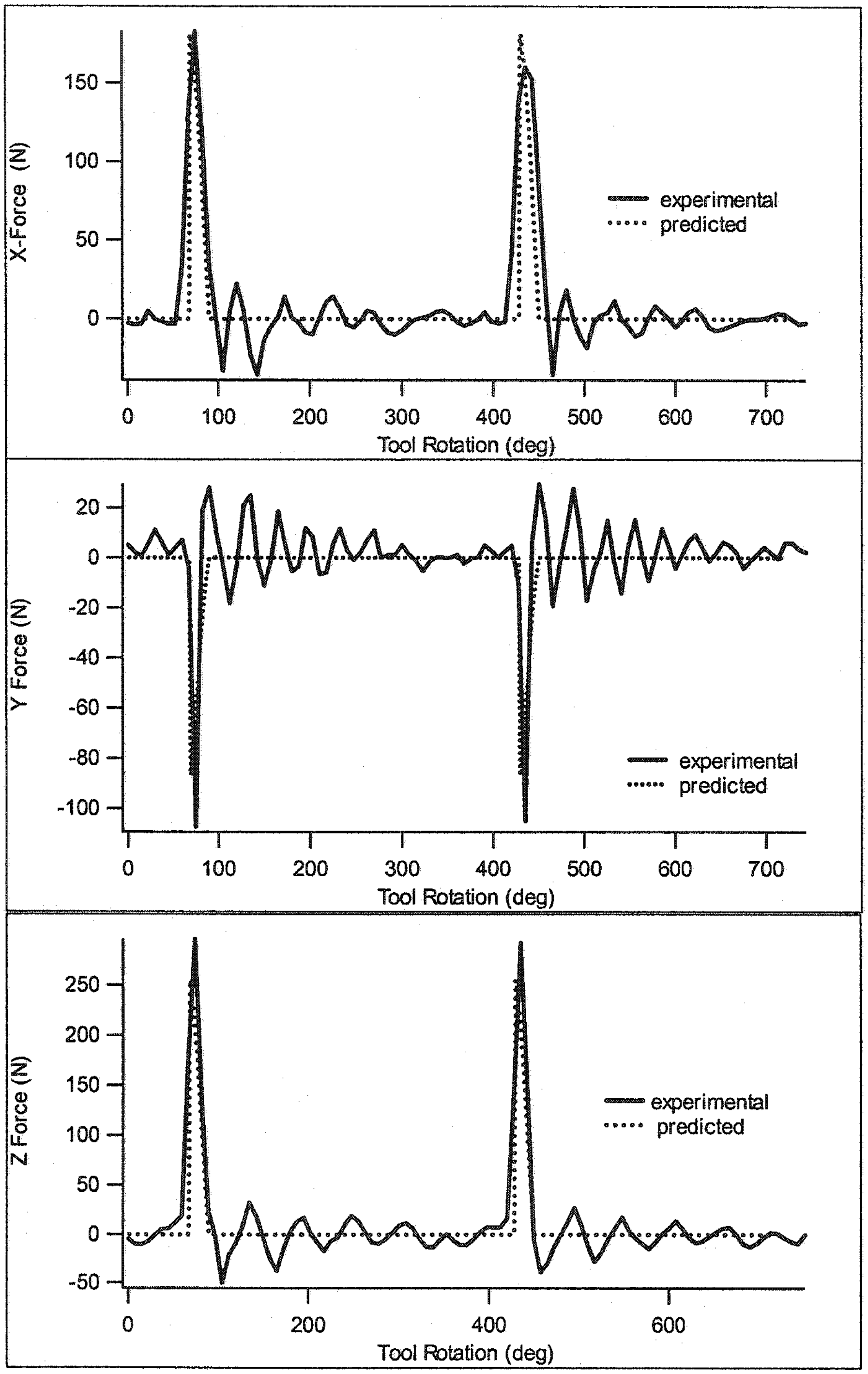

Figure 6.8. Predicted and experimental force for feed of 0.1016 mm/ tooth. (N=10000 RPM, ADOC = .0625 mm, RWOC = 0.25 mm).

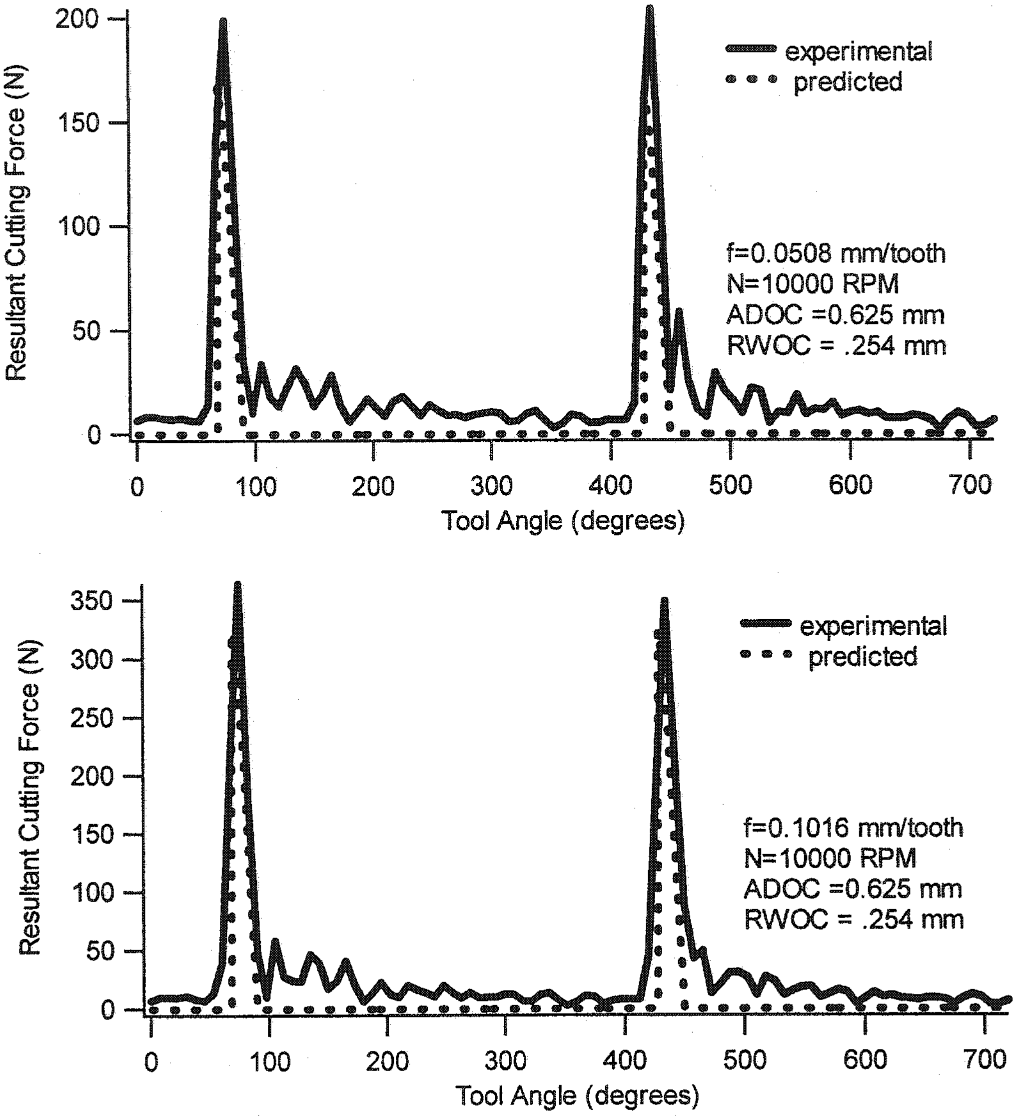

Figure 6.9. Predicted and experimental resultant cutting force for the conditions outlined in figures 6.7 and 6.8.

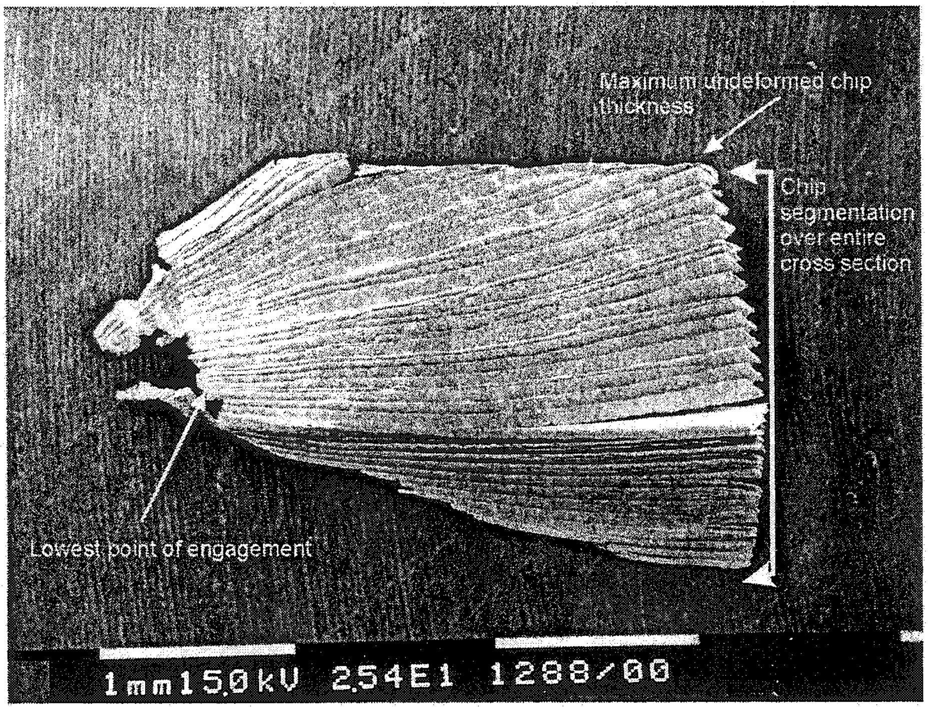

Figure 6.10. Typical chip collected from milling tests showing segmentation across entire chip width.

It can be seen that the Z component of the predicted cutting force in figure 6.7 and 6.8 under estimates the experimental cutting force by 25% (for low feed) and 16 % (for higher feeds) respectively (however the resultant force shows good correlation). This is directly due to the ploughing action of the cutting process. Recall that the chip thickness varies along the cut and the small undeformed chip thickness near the nose of the ball (i.e. $\theta < 25^o$) cause very high ploughing forces. Also recall that the z component of the cutting force arises from the Y-component of the calculated force on the rake face (implying Fy and Fz are coupled). The reasonable correlation between Fx and Fy with the experimental observation suggests that the model captures the effect of the cutting process. An unexpected result arose from the interpretation of the data; having good correlation between Fx and Fy (trend over variations feed rate) allows for decoupling the ploughing component of the force from the cutting process by noting that the underestimation of Fz is directly related to the ploughing action. If Fy was modified to match the z component, then the calculated values of Fy are too high (as a direct result of the coupling between Fy and Fz). Thus, if the cutting conditions such as edge preparation, rake angle, and tool material remain constant, any deviation from the cutting force due to chip formation may be interpreted as an added effect caused by non-linearities such as ploughing, tool wear etc. Further, the chip formation kinematic equations were determined from orthogonal cutting tests where the effective undeformed chip thickness is much greater (as a matter of fact the command feed is the undeformed chip thickness). The deviations arising from a commanded feed rate of 0.0508 mm/tooth in milling is of no surprise since the effective feed levels in both the axial and radial direction is significantly smaller. Therefore, predictions involving smaller feed rates than 0.0508 mm/tooth may deviate significantly from reality. For the present purpose, it may be concluded that the force prediction of the orthogonal model are in good correlation with the experimental values.

Another factor that affects the accuracy of the force model arises from the implementation (and validity) of the material model. The material model must be selected properly in order to provide realistic flow stress predictions. The material model developed in (Becze et.al., 2002) was used to define the flow stress of the material during the machining process. It should be emphasized here that the flow characteristics of materials, in general, varies greatly as hardness increases. The Johnson-Cook constitutive law was used in the analytical model that is developed for high hardness D2 tool steel. Therefore, it is expected that the stress, strain, strain rate, and temperature relationship would apply to the machining conditions presented in this investigation. Further, the Compressive Split Hopkinson Bar (CSHB) test data to determine the shear flow stress of the material utilized the "simple" or "punching" shear configuration. Since the metal cutting process is basically a simple shear stress state (with applied compressive reactionary stresses) the configuration outlined in (Becze et.al., 2002) models the stress state more accurately than that of uniaxial compression/tension tests. This is due to failure mechanisms that are inherent in high strain rate shear tests, which may become more evident in pure shear modes (such adiabatic shear localization). Further, It was observed that localized deformation obtained from the CSHB tests closely resembled that of the localized shear bands in the primary shear zone observed from the chip morphology produced during machining. Figures 6.11 a) and b) illustrate the similarities of the two deformation modes.

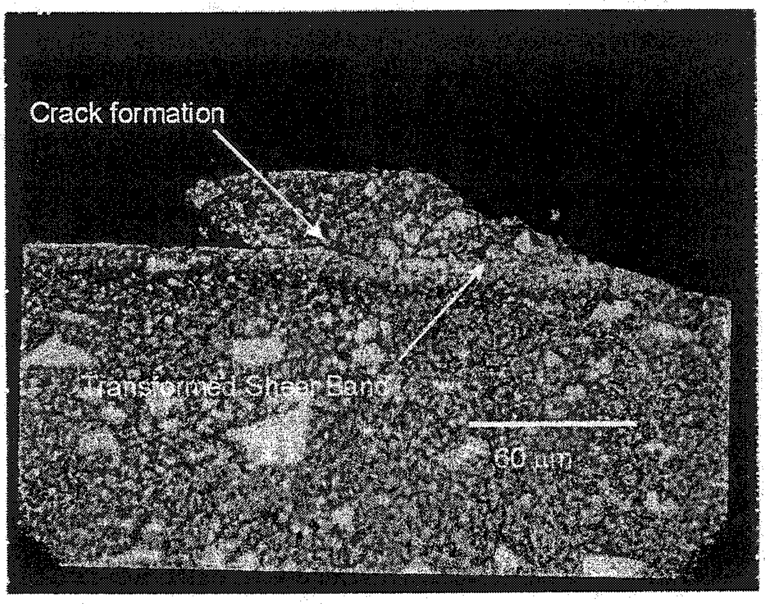

Figure 6.11 a) High strain rate shear test deformed microstructure.

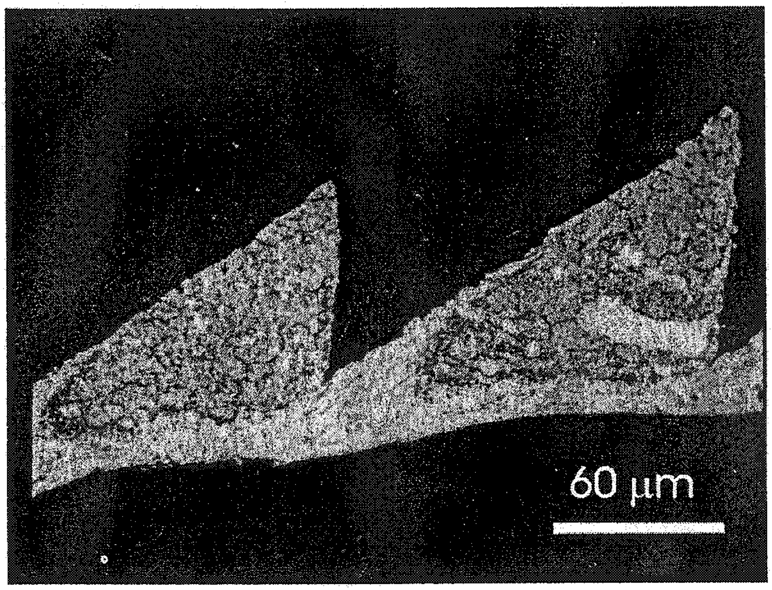

Figure 6.11 b) Deformed chip microstructure.

Figures 6.11 a) and b) illustrate significant similarities. The fact that both contain transformed shear bands indicates that the resulting temperatures of deformation are similar. Further, note the apparent thickness of the shear band in both figures. From figure 6.11 a) the estimated local strain rate is approximately $500000 s^{-1}$ (Becze et al, 2001). The calculated strain rate for the chip in figure 6.11 b) in the primary shear zone is $526\ 123\ s^{-1}$. This is truly remarkable in the fact that the strain rates are very similar and that the resulting microstructure from completely separate testing methods show such great similarities. The estimate was given in (Becze et.al., 2001) by an estimation of the shear band thickness and the resulting stress wave velocity. Whereas, the calculated strain rate was done using the formulation prescribed by equation 7.

The ball end milling process in general requires that the force model represent the cutting force as a function of undeformed chip thickness and effective cutting speed. This is because the undeformed chip thickness varies both axially along the cutting edge engagement position, as well as the radial position of the tool. Further, the effective cutting speed is a function of the working diameter of the cutter engaged with the workpiece and is dependant on the axial position of the element along the cutting edge. Hence the cutting speed itself varies in proportion to the effective working radius. The proposed model addresses these issues. The unique kinematic representation of the chip formation process used in this investigation provides accurate descriptions of the maximum strain and strain rates encountered in machining.

The presented force model provides unique insight into the material mechanical behaviour during cutting induced deformation. The model utilizes shear stresses to compute the cutting force (summed from each shear zone). Thus, determination of the stress levels experienced by the material can be easily obtained. Figure 6.12 illustrates the average shear stress distribution along the primary shear plane for an arbitrary tool position (ω=75°). It can be seen that the primary shear stress distribution is higher at the vicinity of the nose of the ball where the cutting speed is significantly less. This is primarily due to the reduction of strain level because of the small undeformed chip thickness. The reduced cutting speed at the nose of the cutter produces lower temperatures, which reduces the softening potential of the alloy. Figure 6.13 shows the computed differential force on the rake face of the cutter.

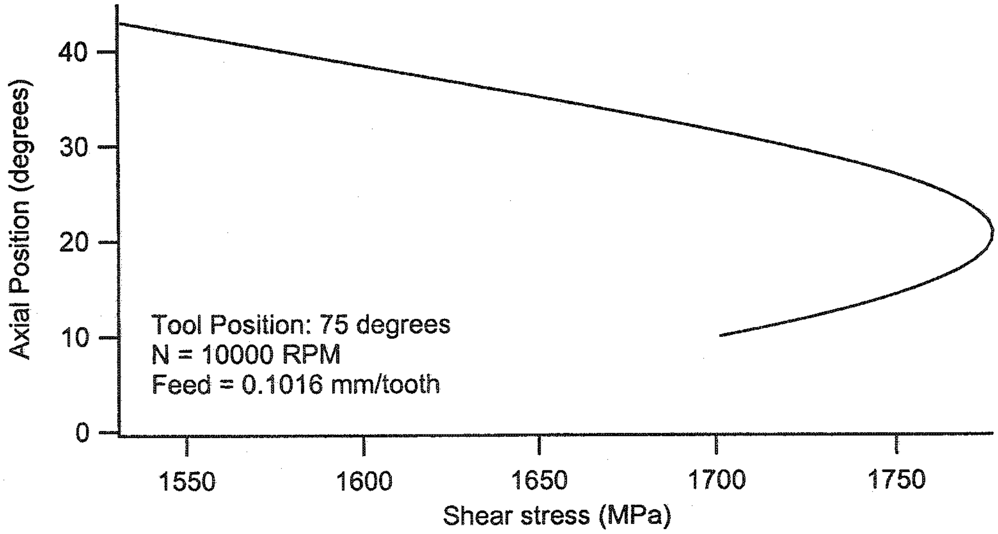

Figure 6.12. Average computed primary shear zone stress along axial position of the cutting edge (ADOC = 0.625 mm, RWOC=0.254 mm, θ=75°).

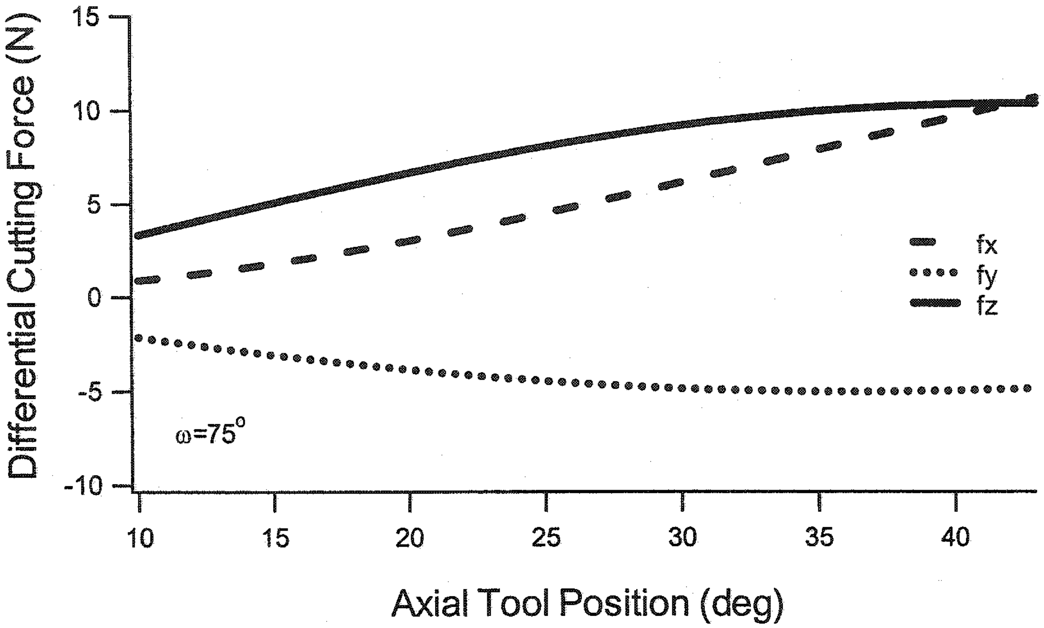

Figure 6.13. Resolved force distribution for the tool position calculated in figure 6.12 (N=10000rpm, f=0.1016 mm/tooth, ADOC = 0.625 mm, RWOC=0.254 mm, ω=75°).

The calculated effective strain level envelope between the minimum and maximum chip height in the primary shear zone is presented in figure 6.14. The figure shows that the strain increases along the axial position of the cutter. This is due to the fact that the chip thickness is increasing along the cutting edge (corresponding to a higher axial position - recall the axial chip thinning phenomenon). Figure 6.15 illustrates the effective strain envelope as a function of tool radial position. This figure shows that the effective strain in chip formation gradually decreases as the tool rotates toward 90° which again, corresponds to radial chip thinning. Although these two figures appear different, they are the same data merely plotted against different axes. The important item to note is the difference in the shape of the envelope. In figure 6.14, the calculated strain level rises in an abrupt fashion. This is because the effect of cutting speed is introduced. In the axial direction, the cutting speed as well as the undeformed chip thickness increases. It was shown in chapter 5 that both feed and speed tend to increase the strain in the primary shear zone. In figure 6.15 the cutting speed is constant at the top of the envelope and therefore the effect of pure feed reduction is observed.

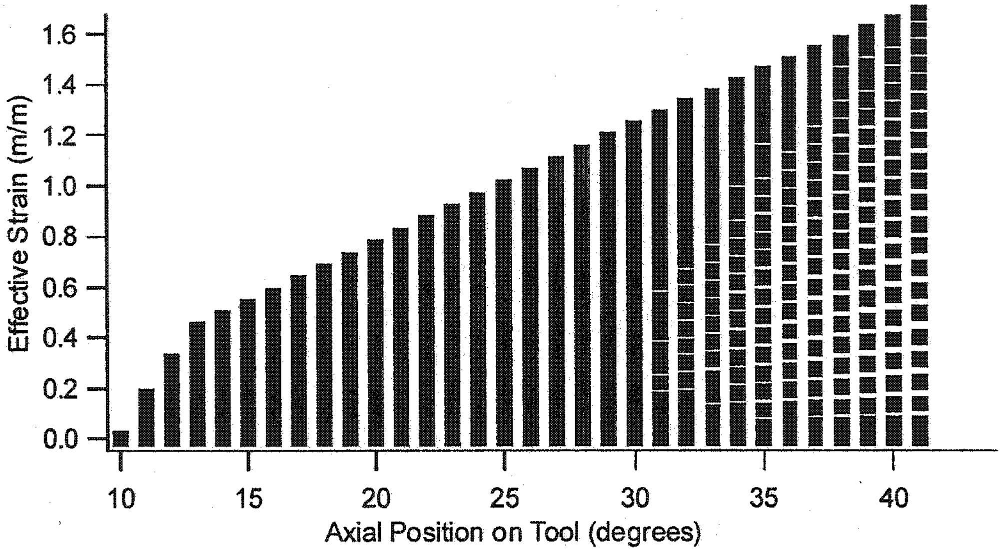

Figure 6.14. The effect of increasing feed and cutting speed as a function of axial position along the ball end mill cutting edge. (N=10000rpm, f=0.056 mm/tooth, ADOC = 0.625 mm, RWOC=0.254 mm)

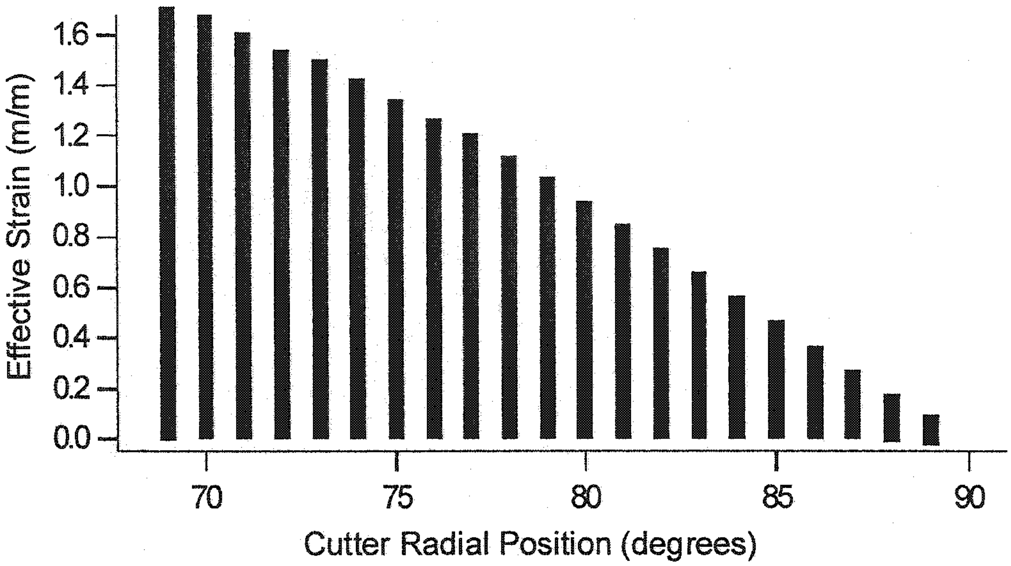

Figure 6.15. The effect of increasing feed as a function of radial position. (N=10000rpm, f=0.056 mm/tooth, ADOC = 0.625 mm, RWOC=0.254 mm)

The chip morphology in milling produces segmented chips (at larger effective feed levels). However, variations in the segmentation can be readily observed from viewing the free surface of the chip. Figure 6.16 shows an SEM image of the free surface of a typical chip collected during milling of hardened D2 tool steel. Recall the time domain simulation result for the primary shear zone stress in figure 6.12. During cutting, the reactionary stress in the primary shear zone, to a large extent, governs the morphology of the chip (Kishawy, 1998). The variation of the shear stress in the primary shear zone implies that a complex stress state occurs between adjacent differential areas (more precisely volumes) over the cutting length in the axial direction. However, it should also be noted that variations in morphology in the radial direction occur because of the reduction in undeformed chip thickness, and is observed by an increasing segmentation frequency. According to figure 6.12, variations in stress should force variations of strain in the chip. The primary shear zone stress acts (or reacts) in the radial direction towards the geometric centre of the tool. Variations in shear stress along the axial direction will cause adjacent material volumes in the chip to react to the variation in stress levels. Although the model does not *predict* the strain per say, the variation in stress is predicted, and correlates well with the microstructure observed in the axial direction. Note the discontinuity in the chip indicated by a break in the saw tooth morphology in the axial direction outlined in figure 6.16. Clearly, the stress-based approach provides an explanation of the structure of the chip morphology in milling. Mechanistic formulations provide no such insight to the cutting process. These results must be obtained strictly from an understanding of the stress levels of deformation during cutting.

Mechanistic force models are used to provide force predictions in very complex cutting processes. Although force predictions provide insight into the cutting process and provide valuable information regarding chatter, cutter and workpiece deflections etc., they are limited in explaining tool wear mechanisms. Interpreting force data should go beyond merely force values. In essence, forces should be interpreted in terms of pressures. If this is done, the present formulation provides insight into why the tool life during the milling tests on D2 tool steel in chapter 3 were so poor. Consider figure 6.13, which shows the differential force distribution along the cutting edge as a function of axial tool position. Figure 6.17 is the corresponding approximation of the area on which the differential force is applied. The area increases a function of axial tool position because of the increase in chip thickness. The rate of increase is a sine wave dictated by equation 23. Figure 6.13 shows that the force gradually increases as a function of axial position (the radial tool position ($\omega=75^{\circ}$) is constant). Therefore, if one considers only the cutting force profile and eliminates all other factors contributing to tool failure, it would seem reasonable to conclude that if the tool chips (assuming of course, that the failure mode is chipping and it is solely a result of forces), then the location of chipping should occur where the force is at the maximum level, which in this case is at the maximum point of engagement. However, this was not the case when milling hardened D2 tool steel. Recall that the main mode of tool failure was chipping at the lowest point of engagement (corresponding to the nose of the cutter). This failure mechanism prevented the tool from wearing to the maximum specified flank wear. (As a matter of fact, no CBN tool wore to maximum specified flank wear for any tests. The end of tool life was strictly governed by tool chipping in the linear cutting tests.) If the force of figure 6.13 is applied to the area prescribe by figure 6.17, the result is the effective pressure on the cutting edge of the tool and is illustrated in figure 6.18.

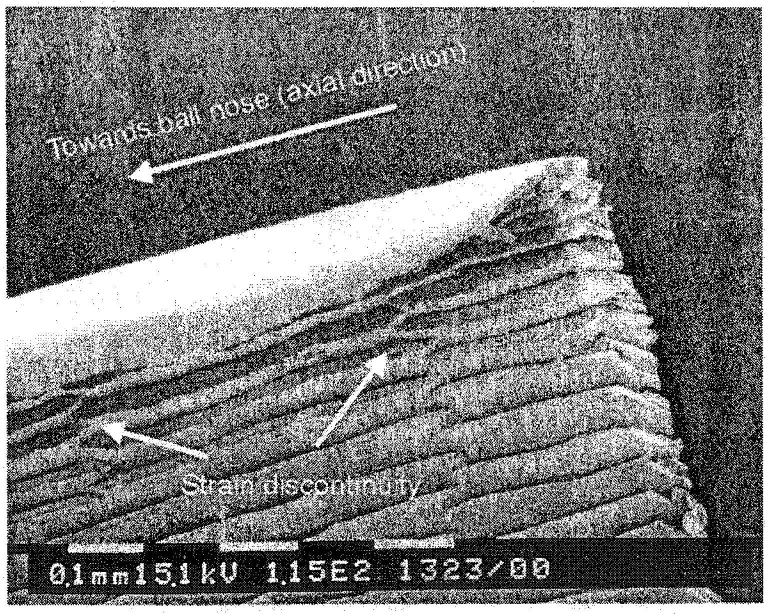

Figure 6.16. SEM image of typical chip formed when milling hardened D2 tool steel showing the strain discontinuity in the axial direction.

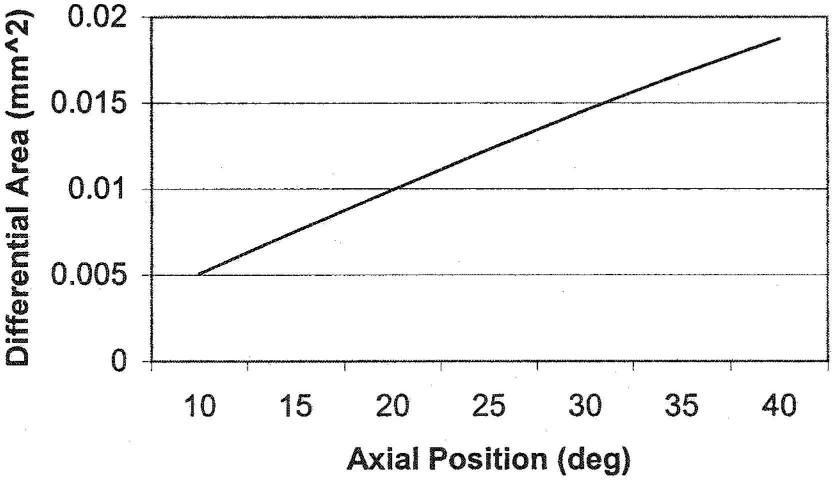

Figure 6.17. The differential area variation as a function of tool axial position at a tool radial position of ω = 75°.

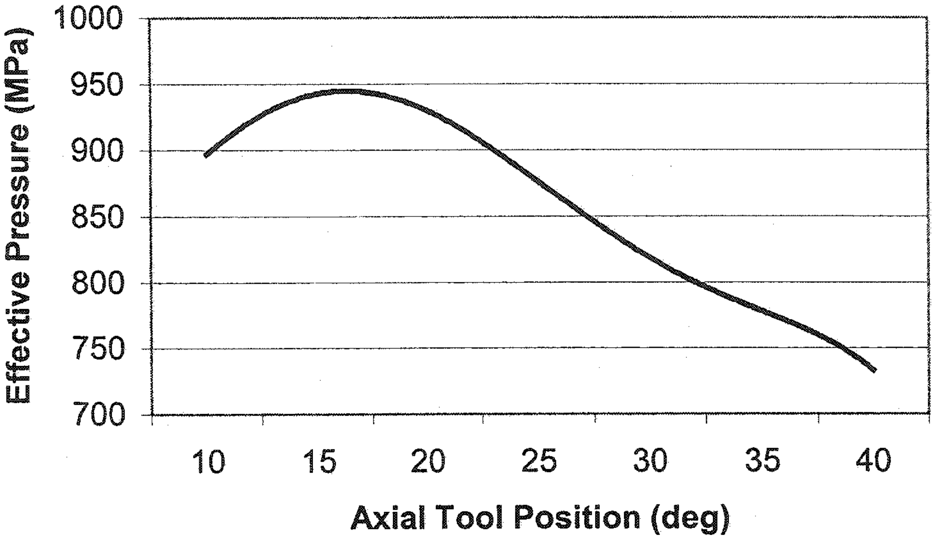

Figure 6.18. The effective pressure along the cutting edge computed from figure 6.13 and 6.17.

It can be seen from figure 6.18 that the pressure is a maximum at the nose of the cutter corresponding to the minimum point of engagement. Also note the relative magnitude of the pressure difference (approximately 30%) and the axial position of the maximum (~15°). This corresponds to the position where the main mode of tool failure occurred. Although the force profile in figure 6.13 clearly shows that the force increases towards that maximum point of engagement, figure 6.18 shows that the pressure is larger at the lower axial positions. This is because the chip is thinner at the lower axial position and therefore the force acting on this area, although lower in magnitude than the maximum force, causes a higher pressure. This happens because the rate of decrease in the area is greater than the reduction in differential force. In reality, the machine tool dynamics cannot be decoupled from the pressure effects. Machine tool vibrations are a significant factor in shortening tool life (Becze et al, 1999). As a matter of fact, vibrations are a primary cause of cutting edge failure by chipping. However, the present analysis shows that the pressure distribution may also provide a mechanism which, when combined with the dynamics of the cutting process, will explain the tool failure mode observed in chapter 3.

The form of the pressure profile of figure 6.18 could be obtained (although in a much more difficult manner) from the results of figure 6.12. Recall that figure 6.12 is the computed shear stress on the primary shear zone. The formulation uses this shear traction to compute part of the cutting force. Since the stress levels are shown to vary in the primary shear zone, the pressure along the cutting edge could also have been deduced from this figure. This would require the instantaneous rake face orientation with respect to the machine tool coordinate system, the chip flow angle, the effective rake angle, the lead angle position (which orients the rake face), and the effective stress in the primary and secondary shear zones. Resolving these onto the rake face, and converting to an effective pressure over the chip thickness would result in the pressure distribution. Nevertheless, the form of the predicted shear zone stress (although the calculation is much more cumbersome) is similar to the less rigorous formulation of the previous method.

If the results of the D2 milling tests could have been rationalized in this way at the onset of the research, then countless hours spent attempting to find alternative cutting conditions to maximize tool life could have been avoided. Recall that it was attempted to reduce the chipping of the cutting edges by increasing the tilt angle (from 10° to 25°) to increase the minimum cutting speed. The logic behind the decision was to provide a mechanism to thermally soften the material to provide lower flow stresses. This increase in tilt angle not only created extra vibrations in the machine tool (due to the larger radial load on the cutter) but also places the cutting edge at a high cutting pressure location, and thus may reduce the tool life. Hence, approaching the problem by understanding the pressure as opposed to examining the cutting force profile could have prevented these tests from being performed.

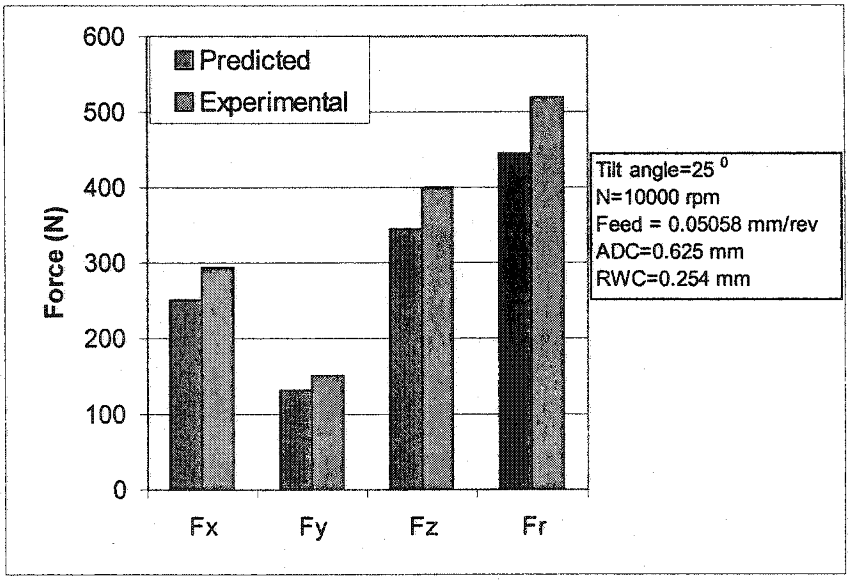

Figure 6.19. The effect of tilt angle variation in predicted and experimental cutting force values.

The simulation was performed for a tilt angle of 25°. Figure 6.19 illustrates the effect of changing the tilt angle of the workpiece on the cutting forces. It can be seen that all forces correlate well with the experimental results (within 15% in the resultant). Note that for large tilt angles, there is a better correlation between the predicted and experimental values of Fz (~20% error as opposed to 25% for this feed level). This corresponds to a reduction of the ploughing effect on the nose of the cutter since the minimum point of engagement begins at 25°. Ploughing is reduced for larger tilt angles because the effective chip load becomes larger and therefore a much more efficient shearing process can be expected (Kishawy, 1998). This effect allows an important point to be made. There is a range of conditions, which the model can simulate very well. This corresponds to larger undeformed chip thickness levels, which incidentally correspond reasonable strain levels. Thus, the primary limitation of the orthogonal formulation is mainly feed effects. The former arguments imply that variations in cutting speed can be simulated with reasonable accuracy (as the previous results showed). The feed variations on the other hand show that the model tends to deviate with reducing the chip thickness levels where the limiting value for feed was found to be 0.0508 mm/rev. This occurs as a result of the chip-formation based formulation for the strain levels. The empirically represented strain levels below this feed in milling are outside the bounds of the formulation for the governing equations regarding the chip morphology. It is however remarkable that the trends in milling can be simulated with reasonable accuracy in a region of chip thicknesses much smaller than those of turning simulations.

Altintas and Budak (1996) have shown that mechanistic formulations of orthogonal turning data can be extended to oblique configurations. The logic being the cutting mechanics are general in nature, and therefore can be applied with reasonable confidence to any cutting process. The results of this chapter show that this is indeed the case provided that the chip loads are maintained at reasonable levels. Effects such as ploughing on the other hand, cause severe non-linearities that must be accounted for by other means. The stress-based formulation allows for the decoupling of the non-linearities because the simulation models the cutting process directly.

6.6 Chapter Summary

A force model for oblique cutting has been developed that was based on the analytic orthogonal model developed in chapter 5. The use of chip formation and chip morphology of segmented saw toothed chips to define the strains and strain rates associated with the machining process prove to be a viable way to model the cutting process. The approach taken provides a unique description of the machining process by providing the shear tractions to compute cutting forces.

The model was applied to a ball end milling process for machining hardened AISI D2 tool steel to test the validity of the orthogonal model. The in-cut chip geometry obtained from measurements of the tool-workpiece contact was used to define the chip load for various cutting conditions. The force model provided good agreement with the experimental force data for the cutting conditions used in this investigation. However, it was found that below a feed level of 0.0508 mm/rev in milling, non-linearities such as ploughing affect the accuracy of the results. For higher feed rates or conditions that minimize the effect of ploughing, the orthogonal model can be used to model oblique cutting conditions.

Good correlation of the predicted cutting force with the experimental force was observed and indicates that the chip formation mechanisms and hence the cutting mechanics in orthogonal turning tests do not change for milling when the undeformed chip thickness is substantially less. This allows extrapolation of orthogonal turning data to model the cutting process for any oblique configuration within the limits the model has been verified.

Chapter 7

Conclusions and Recommendations

7.1 Introduction

The objective of the manuscript was to outline the focussed approach used for the modelling and the analysis of machining hardened tool steels. The main focus of the research lies in the modelling methodology employed to describe the machining process. Ultimately, the major goal was to develop a unique analytical modelling methodology that may be used to represent the complex phenomenon of metal removal by geometrically defined cutting edges. This chapter will present and outline the major conclusions and contributions obtained from the research conducted in this investigation.

7.2 Summary of the Research

The present research represents a journey that was endured to finally arrive at a novel modelling approach that may be employed to the analysis of machining of hardened tool steels. Chapter 3 illustrated the experimental results of research conducted on ball nose end milling of hardened tool steels. The research began in 1996 when high speed hard milling was in its relative infancy, where critical issues such as optimal cutting conditions, and factors affecting tool life etc. was not well understood. The purpose of chapter 3 was to define a database of cutting conditions that provided a long tool life to enable the technology of high speed milling of dies and molds. The research began on AISI H13, a hot forge mold steel. The hardness of the material was varied to understand the relationship between hardness and machinability in relation to process parameters and tool life from a fundamental perspective. It should be evident that special focus was given to the morphology of the chips produced during the milling process. This provided a unique correlation between the cutting conditions and the response of the alloy. It was concluded that the machining high hardness steels is a viable technology provided that the spindle speeds are high, the proper edge geometry is selected and the stiffness of the machine tool is adequate to compensate for the higher dynamic cutting forces in relation to the small chip loads. The general conclusion was that small chip loads combined with sharp cutting edges and very high spindle speeds under dry cutting conditions provided the longest tool life.

As the research progressed, a second material was investigated - AISI D2 tool steel hardened to 60 + HRc. This material provided a significant challenge to machine (to say the least). The metallurgy of the alloy (the presence of large abrasive alloy carbides), combined with the extreme hardness of the alloy yielded depressingly short tool lives. The sensitivity of the alloy to cutting conditions was extremely pronounced. It was possible to machine hardened D2 tool steel, but at great expense. The tool life during the machining of D2 at 62 HRc (linear cutting) was typically an order of magnitude less than that of H13 at 55 HRc, whereas in multi-axis milling the tool life is increased marginally due to the reduction of the chip load when cornering. However, primarily the main mode of tool failure, in contrast to H13 was consistently chipping of the cutting edge with PCBN cutting tools. It was felt that understanding the machining process from a fundamental perspective would be relevant in explaining the short tool life when machining hardened D2 tool steel. This was achieved by developing an analytic force model that was based on the rate dependant mechanical properties of the alloy.

Early on in the research, it became evident that force modelling could follow two distinct methodologies; empirical or mechanistic modelling using calibrated coefficients combined with the geometric relations defining the cutting process, or analytic methods requiring a much more comprehensive understanding of the deformation process. Analytic methods necessarily require knowledge of the flow stress of the material as a function of cutting (or deformation) conditions. Empirical methods may be elegant in the strategies, however, provide very little insight to the actual cutting process. It was concluded that an attempt to model the machining process from a thermo-visco-plastic approach would provide significant insight to the understanding of the shearing process when machining hardened D2 tool steel.

It was evident that an understanding of the material at high strain rates and large strains was necessary in understanding the deformation behaviour of the material. Since no information was available for the high strain rate response of D2 tool steel in the hardened state, research was implemented to investigate this behaviour. Chapter 4 outlined the results of the high strain rate characterization of hardened AISI D2 tool steel. The main conclusion of the chapter was more of a constitutive relation that governed the flow properties of hardened D2. The configuration of the testing strategy was unique in the sense that a simple shear load path was chosen to analyse the stress-strain response of the material. This provided an accurate representation of the response of the material under high strain rate machining conditions. The tests were conducted at strain rates in excess of 50000 s^{-1}, and strains approaching unity. Under these loading conditions, the metal removal process was more easily modelled with the flow rules obtained from the research. Thus the motivation for chapter 4 was strictly to provide a robust correlation between kinematic parameters such as strain, strain rate and temperature to the flow response of the alloy.

The representation of the flow stress was obtained from two distinct constitutive laws; an empirically based formulation known commonly as the Johnson-Cook law, and the so called physically based formulation provided by Zerilli and Armstrong. Both formulations provided accurate and robust representations of the flow stress, however, the convenient form of the Johnson-Cook law was chosen based on its simplicity of use, and the limitation given by its temperature dependence.

Having a robust correlation of the flow stress with the governing kinematic parameters such as strain, strain rate and temperature, attempts at modelling the forces during machining were then addressed. The main problem encountered was the determination of the strains, and strain rates as a function of machining parameters. Chapter 5 outlines the methodology employed for determining these parameters. Ultimately, two major inputs were desired; namely feed rate and cutting speed. The logic behind this requirement becomes apparent when one considers the ball milling process where precisely these parameters are varied as a function of ball geometry. Chapter 5 provided several methods to rigorously test the validity of the orthogonal model with experimentation, and well established finite element principles (provided by Dr. El-Wardany). The unique formulation of the orthogonal force model relied heavily on formulations based on observed chip morphology. Chapter 3 illustrated that saw toothed chips consistently form when machining hardened steels. The model was derived from the consistent morphology of the chips produced during machining. The consistency of the saw toothed chip formation provided robust methods of determining the formulations for the strain, and strain rates during the machining process. This was integral to the model's success. The unique approach provided consistent and compatible solutions for the primary inputs obtained from orthogonal machining experiments. The model was also extended to several other materials that are known to form segmented saw toothed type chips. A unique benefit from the modelling formulation was the ability to dynamically calculate the adiabatic temperature during the shearing process. This was found not to be another exercise in modelling, but a necessity in determining the dynamic time dependant flow stress of the material. The modelling formulation was designed to be used as a time domain simulation.

The success of the orthogonal force model outlined in chapter 5 led to the extension of the time domain simulation into an oblique configuration of chapter 6. This was a natural extension, as it provided a solution for two key concerns: the validity of the model was extended to small chip loads and cutting speeds, and it inadvertently provided a rationalization of the experimental data obtained in chapter 3. The primary difficulty for extrapolation of the orthogonal force model was the geometry associated with the cutting conditions. It was shown that the force modelling methodology provided reasonable predictions for cutting conditions down to a certain chip load. This was rationalized by determining that the cutting mechanism changes, where after a certain limit, the ploughing component becomes much more significant. In general, the orthogonal to oblique methodology has been shown to be successful, however, limitations exist and must be accounted for. Due to the unique nature of the modelling strategy, insight was provided (from the simulation data) which at least in part explains the very short tool life and tool failure mode when milling hardened tool steels.

7.3 Major Contributions

The major contributions of this dissertation may be broken down and represented by the contributions of each chapter.

Chapter 3 illustrated the experimental investigation for high speed ball end milling of hardened tool steel. The contributions are:

- The technology of high speed ball end milling of hardened die materials using PCBN cutting tools is a viable technology. For AISI H13 (HRc 55) the tool life is reasonable with the primary mode of tool failure being maximum wear land length.
- Contrary to the manufacturer's recommendation, which was based on hard turning technology, a sharp cutting edge with no coolant is required for long tool life.
- High speed ball milling of hard AISI D2 tool steel (HRc 62) is feasible but at high cost. Tool life is very short, typically 10% of that of H13, and the primary mode of failure is chipping of the cutting edge at the minimum point of engagement. Multi axis milling extends tool life by a factor of 1.5.

Chapter 4 illustrated the experimental investigation on the high strain rate flow stress behaviour of hardened AISI D2 tools steel. The major contributions are:

- The modified Vecchio configuration for punching shear tests provides high strain rates and strains when performed on hardened materials.

- The simple shear configuration represents the metal shearing process of machining adequately.
- Two constitutive formulations were fitted to provide data that correlated the large strain, large strain rate, and high temperature behaviour of hardened AISI D2 tool steel. These being the Johnson-Cook and Zerrilli-Armstrong formulation. The data provided accurate and robust representations of the flow stress.
- The data was modelled (and fitted) using the dynamic adiabatic temperature rise during deformation. This provided accurate correlations of the flow stress and the temperature behaviour of the material.
- Metallurgical data was presented which illustrated the failure mode of the material under high strain rates.

Chapter 5 presented the derivation and formulation of the orthogonal force model. The contributions are as follows:

- The chip formation based formulation provided herein uniquely represents the deformation conditions as a function of the cutting conditions. This provided a unique representation of the kinematic properties, which maintained observed compatibility with the chip morphology. The strains and strain rates represented by the presented formulations provided reasonable values.
- The formulation is valid for saw-toothed segmented chip morphologies.
- The simple shear constitutive formulation was successfully used to model the dynamic flow stress of the material in terms of feed and cutting speed.

- The very nature of the model required that temperature be used as an input for the time domain simulation.
- The model in its entirety is completely unique.
- The fundamental inputs are relatively simple, namely cutting speed and feed rate. This enabled the extension to ball milling.

Chapter 6 presented the oblique extension of the orthogonal force model to an oblique configuration defining the ball milling process. The contributions are as follows:

- The orthogonal to oblique transformation of the thermo-visco-plastic approach has been performed.
- The orthogonal model has been extended to small chip loads and very low cutting speeds beyond the range that was investigated in chapter 5. The success was due to the unique formulation based on chip morphology.
- The formulation provided reasonable predictions of the cutting forces during ball milling.
- A novel approach was adopted based on the model predictions to explain the extremely short tool life observed in chapter 3.

In general, the approach to modelling in this investigation is unique and has yet to be paralleled. The approach brings an avenue of modelling slightly closer to reality. Although the method may seem elegant, it is cumbersome, very experimentally intensive, very time consuming in terms of analysis, and requires a profound and very fundamental understanding of the physics of the deformation process. However, aside from these limitations, the method provides a unique formulation to model machining processes, which may be a reasonable alternative to mechanistic modelling strategies.

7.4 Recommendations for Future Work

A sense of closure to the preceding research may be provided by some future work. If the reader recalls, the formulation for the orthogonal force model relied heavily on tedious analysis of the chip morphology produced for various cutting conditions. This was done as it was the only method presently available to systematically represent the deformation kinematics in a reliable, predictable fashion. Since the trends observed are relatively repeatable, and by virtue of the modelling formulation's accuracy, it is recommended that precise analytical representations for the deformed chip morphology be attempted. This is in contrast to the empirical representations given in the preceding manuscript. Attempts at this would require a profound understanding of the response of the material under the given cutting conditions. Further, the understanding of the metal cutting process would benefit from this as the empirical nature of the process may in part be removed.

Unfortunately, there are several factors that limited the thoroughness of the investigation. Precise temperature measurements along the shear plane at realistic conditions should be sought to verify exactly how much temperature is generated during the cutting process. This would provide a convenient closed form expression of the strain to failure as well as determining how much “energy traps” are available to reduce the actual temperature. Extension of this recommendation may provide a unique basis for determination of residual stress predictions. This of course could be attempted when the sensing technology evolves to a state where it permits accurate measurements to be obtained during the machining process.

The constitutive formulation in chapter 4 was used for predicting the flow stress of the material. However, the formulation was not rigorously tested and therefore it is recommended that the constitutive law be tested in other configurations not including shear. It was hypothesized that the failure mechanisms change according to the loading conditions. It would be of fundamental importance to understand this behaviour. As a result, the material should be tested in tensile configurations to reveal the nature of the deformation mechanics and possibly relate this to the segmented chip morphology.

To provide a sense of closure to the viability of the machining of hardened AISI D2 tool steel, it is recommended that systematic tests be conducted for determining tool life on a machine tool that is rigid enough (i.e. high stiffness) to reduce the incessant vibrations associated with the machining of hardened materials. The author believes that machining hardened tool steels with PCBN end mills can be a viable and cost effective technology if the detrimental effects of machine tool dynamics can be eliminated.

References:

Abrari, F. and Elbestawi, M. A., 1997,"Closed Form Formulation of Cutting Forces For Ball and Flat End Mills", Int. J. Mach. Tools Manufact. Vol.37, No. 1, pp. 17-27.

Abrari, F., Elbestawi, M.A. and Spence, A.D., 1998, "On the Dynamics of Ball End Milling: Modelling of Cutting Forces and Stability Analysis", Int. J. of Machine Tools & Manufact., Vol. 38, No. 3, pp. 215-237.

Abrari, F., Elbestawi, M.A., and Spence, A.D., 2001, "On Machining Dynamics of Flexible Parts", Accepted for Publication, I Mech E J. of Multi-Body Dynamics.

Altan, T., Lilly B. W., Kruth, J. P., Konig, W., Tonshoff, H. K., Van Luttervelt, C. A. and Khairy, A. B., 1993, "Advanced Techniques for Die and Mold Manufacturing", Annals of CIRP, Vol. 42/4, pp 707.

Andrade, U., Meyers, M.A., Vecchio, K.S., Chokshi, A.H., (1994), "Dynamic Recrystallization in High-Strain, High-Strain Rate Plastic Deformation of Copper", Acta Metall. Mater., 29, pp. 3183-3195.

Armarego, E.J. 1983, "Practical Implications of Classical Thin Shear Zone Cutting Analysis", UNESCO/CIRP Seminar on Manufacturing Technology, pp. 167-182, Singapore.

Armarego, E.J.A., Brown, R.H., 1969, "The Machining of Metals", Prentice Hall.

Armarego, E.J., Deshpande, N.P., 1993, "Force Prediction Models and CAD/CAM Software for Helical Tooth Milling Processes, Part I Basic Approach and Cutting Analysis", Vol. 31, No. 8, pp. 1991-2009.

Armarego, E.J., Deshpande, N.P., 1993, " Part II – Peripheral Milling Operations", Vol. 31, No. 10, pp. 2319-2336.

Armarego, E.J., Smith, A.J.R., Gong, Z.J., 1990, "Four Plane Facet Point Drills – Basic Design and Cutting Model Predictions", Annals of the CIRP, Vol. 39/1, pp. 41-45.

Armarego E.J., Uthaichaya, M., 1977, "A Mechanics of Cutting Approach for Force Prediction in Turning Operations", J. Eng. Prod., Vol. 1, No.1, pp. 1-18.

Armerego, E.J., Whitfield, R.C., 1985, "Computer Based Modelling of Popular Machining Operations for Force and Power Predictions", Annals of the CIRP, Vol. 34, pp.65-69.

Bai, Y., Dodd, B., (1992), "*Adiabatic Shear Localization Occurrence, Theories and Applications*", Pergamon Press, Oxford U.K..

Bailey, T., Elbestawi, M .A., El-Wardany, T. and Fitzpatrick, P., "Generic Simulation Approach for Multi-Axis Machining - Part I Modelling Methodology", ASME IMECE 2000, Orlando, pp.997-1008.

Balaji, AK, G. Sreeram, I.S. Jawahir and E. Lenz, 1999, "The Effects of Cutting Tool Thermal Conductivity on Tool-Chip Contact length and Cyclic Chip Formation in Machining with Grooved Tools", Annals of the CIRP, Vol. 48(1), pp. 33-38.

Becze, E., Clayton, P., Chen, L., El-Wardany, T.I. and Elbestawi, M.A., (2000), "High Speed 5-Axis Milling of Hardened Tool Steel", Int. J. of Machine Tools & Manufact., Vol. 40, pp. 869-885.

Becze, C.E., Worswick, M.J., Elbestawi, M.A., 2001, High Strain Rate Shear Evaluation and Characterization of AISI D2 Tool Steel in its Hardened State, Accepted for Publication, Machining Sciences and Technology.

Becze,C.E., Elbestawi, M.A., 2001, "Analytical Oblique Force Modelling of Ball Milling Processes Producing Saw Toothed Chips", Accepted for Publication in MTDR.

Boehner, J., Dumitrescu, M., Elbestawi, M.A., El-Wardany, T.I. and Chen, L., (1999), "Influence of Material Microstructure on Tool Performance in High Speed Machining", Trans. NAMRI-SME, Vol. XXVII, Berkeley, CA, pp. 129-134.

Boehner, J., Dumitrescu, M., Elbestawi, M.A., El-Wardany, T.I. and Chen, L., (1999), "Effect of Carbide Tool Grades and Cutting Edge Geometry on Tool Life during High Speed Machining of Hardened Tool Steel", 2nd Int. German and French Conf., Darmstadt, pp. 37-46.

Budak, E., Altintas, Y., Armarego, E.J., 1996, "Prediction of Cutting Force Coefficients from Orthogonal Cutting Data", Trans. ASME, J. Manuf. Sci. Eng., Vol 118, pp. 216-224.

Childs, T.H.C., (1998), "Material Property Needs in Modeling Metal Machining", CIRP International Workshop on Modeling of Machining Operations, pp. 2B/2-1 – 2B/2-10.

Chou, Y. S., Barash, M. M., 1995, "Review on Hard Turning and CBN Cutting Tools", 1st International Machining and Grinding Conference, Sept. Dearborn, Michigan, MR95-21, pp 951-962.

Clayton, P., Elbestawi, M.A., El-Wardany, T. and Viens, D., "A Mechanistic Force Model of the 5-Axis Milling Process", ASME IMECE 2000, Orlando, 2000, pp. 979-988.

Cook, N. H., Finnie, I., Shaw, M. C., Mass, C., 1954, "Discontinuous Chip Formation," Transactions of the ASME, Vol. 76, pp. 153-162.

Davies, M. A., Chou, Y., and Evans, C. J., 1996, "On Chip Morphology, Tool Wear and Cutting Mechanics in Finish Hard Turning," Annals of the CIRP, Vol 45, pp. 77- 82

Dautzenburg, J.H., Veenstra, P.C., Van der Wolf, 1981, "The Minimum Energy Principle for the Cutting Process in Theory and Experiment", Annals of the CIPR, Vol 30/1, pp. 1-4.

Boehner, J., Dumitrescu, M., Elbestawi, M.A., El-Wardany, T.I. and Chen, L., "Influence of Material Microstructure on Tool Performance in High Speed Machining", Trans. NAMRI-SME, Vol. XXVII, Berkeley, CA, 1999, pp. 129-134.

Elbestawi, M.A., Srivastava, A.K. and El-Wardany, T.I., 1996 "A Model for Chip Formation during Machining of Hardened Steel", Annals of the CIRP, Vol. 45/1, pp. 71-76.

Elbestawi, M.A., Chen, L., Becze, C.E., El-Wardany, T.I., 1997, High Speed Milling of Dies and Molds in Their Hardened State, Annals of the CIRP, 46/1:57-62.

El-Wardany, T.I., Kishawy, H.A., and Elbestawi, M.A, (2000), "Surface Integrity of Die Material in High Speed Hard Machining: Part 1: Micrographical Analysis", Accepted for Publication, ASME J. of Manufact. Sci. and Eng, Part 1.

El-Wardany, T.I., Kishawy, H.A., and Elbestawi, M.A., (2000), "Surface Integrity of Die Material in High Speed Hard Machining: Part 2: Microhardness Variations and Residual Stresses", Accepted for Publication, ASME J. of Manufact. Sci. and Eng. Part 2.

El-Wardany, T.I., Viens, D., Huang, G.C., Dierberger, J., 2001, "Finite Element Simulation of Machining Process With Mesh Adaptation and Fracture Criteria", 7th International Conference on Numerical Methods in Industrial Forming Processes, Toyohashi, Japan, June 18-21, 2001, NUMIFORM 2001.

El-Wardany, T.I., Boelhouwer, A.M., Elbestawi, M.A., 1995, "High Speed Machining of Nickel-Based Super Alloys with Silicon Carbide Whisker Reinforce Ceramics", 1st International Machining and Grinding Conference, SME, pp 1-26.

Fang, N., I.S. Jawahir and P.L.B. Oxley, 2001, "A Universal Slip-line Field Model with Non-unique Solutions for Machining with Curled Chip Formation and a Restricted Contact Tool", Int. J. Mechanical Sciences, Vol. 43, pp. 557-580.

Fang, N. and I.S. Jawahir, 2001, "A New Methodology for Determining the Stress State of the Plastic Region in Machining with Restricted Contact Tools",Int. J. Mechanical Sciences, Vol. 43, pp. 1747-1770.

Field, M. and Merchant, M. E., 1949, "Mechanics of Formation of The Discontinuous Chip in Metal Cutting," Transactions of the ASME, Vol. 71, pp. 421-430.

Gekonde, H.O., 1998, "*Influence of Dynamic Behaviour of Materials on Machinablity*", Ph.D. Thesis, McMaster University, Hamilton, Ontario, Canada.

Ikeda, T., Takahashi, I., Matsuoka, T. and Nakagawa, T., 1992, "Ultra High Speed Milling of Die Steel with Ball-nose End mill", Proc. Of the 2nd Int. Conf. On Die and Mold Technology, Singapore, Sept., pp 48-56.

Imani, B.. And Elbestawi, M.A., 2001 "Comprehensive Geometric Simulation of Ball End Milling Operations", Accepted for Publication, ASME J. of Manufact. Sci. and Eng.

Imani, B.M., Sadeghi, M.H. and Elbestawi, M.A., 1998, "An Improved Process Simulation System for Ball End Milling of Sculptured Surfaces", Int. J. of Machine Tools and Manuf., Vol. 38, No. 44, pp. 1089-1167.

Jaspers, S. (1999), "*Metal Cutting Mechanics and Material Behaviour*" Ph.D. Thesis, Delft, Netherlands.

Jawahir,I.S. and Zhang, J.P., 1995, "An Analysis of Chip Curl Development, Chip Deformation and Chip Breaking in Orthogonal Machining", Trans. NAMRI, Vol. 23, pp. 109-114.

Jawahir, I.S., O.W. Dillon, AK Balaji, M. Redetzky and N. Fang, 1998, "Predictive Modeling of Machining Performance in Turning Operations", Proc. CIRP Int. Workshop on Modeling of Machining Operations, Atlanta, GA, May, pp. 161-176.

Jawahir, I.S. And AK Balaji, August 2000,"Predictive Modeling and Optimization of Turning Operations with Complex Grooved Tools for Curled Chip Formation and Chip Breaking", Proc. 3rd CIRP International Workshop on Modeling of Machining Operations, Sydney, Australia, pp. 41-59.

Jawahir, I.S. And AK Balaji, 2000, "Predictive Modeling and Optimization of Turning Operations with Complex Grooved Tools for Curled Chip Formation and Chip Breaking", J. Machining Science & Technology, Vol. 4(3), pp. 399-443.

Johnson, G.R., Hoegfeldt, J.M., Lindholm, U.S., Nagy, A., 1983(b) "Response of Various Metals to Large Torsional Strains over a Large Range of Strain Rates- Part 2: Less Ductile Metals", J. Engng. Matl. Tech., 105, pp. 42-47.

Johnson, G.R., and Cook, W.H., (1983), In Proc. 7th Int. Symp. On Ballistics, The Hague, pp. 541-547.

Kruth, J. P. and Klewais, P., 1994, "Optimization and Dynamic Adaptation of Cutter Inclination During Five-Axis Milling of Sculptured Surfaces", Annals of CIRP, Vol. 43/1, pp 443-448.

Kelly, A., MacMillan, N.H., (1986), "*Strong Solids*" 3rd ed., Clarendon Press, Oxford.

Kishawy, H.A., 1998, "Chip Formation and Surface Integrity in High Speed Machining", Ph.D. Thesis, McMaster University, Hamilton, Ontario, Canada.

Kline, W.A., DeVor, R.E., 1983, " The Effect of Runout on Cutting Geometry and Forces in End Milling", Int. J. Mach. Tool Des. Res., V. 23, No. 2/3, pp. 123-140.

Komanduri, R. and Brown, R. H., 1981, "On the Mechanics of Chip Formation in Machining," Transaction of the ASME, Journal of Engineering for Industry, Vol 103, pp. 33-51.

Komanduri, R., Schroeder, T., Hazra, J., Von Turkovich, B. F., and Flom D. G., 1982, "On the Catastrophic Shear Instability in High-Speed Machining of an AISI 4340 Steel, " Transaction of the ASME, Journal of Engineering for Industry, Vol. 104, pp. 121-131.

König, W., Komanduri, R., Tonshoff, H. K., and Ackershott, G., 1990, "Machining of Hard Materials," Annals of the CIRP Vol. 39/1, pp. 417-427.

König, W., Berktold, A., and Koch, F. K., 1993, "Turning Versus Grinding- A Comparison of Surface Integrity Aspects and Attainable Accuracies," Annals of the CIRP, Vol. 42, pp. 39-43.

Konig, W., and Wand, Th,. 1987, "Turning Bearing Steel with Amborite and Ceramic" Indust. Diam. Rev., pp 117-120.

Lajczok, M. R., 1980, "A Study of Some Aspects of Metal Machining Using the Finite Element Method," Ph. D. Dissertation, North Carolina State University.

Lee, W-S., Yeh, G-W.,1997, The Plastic Deformation Behaviour of AISI 4340 Alloy Steel Subject to High Temperature and High Strain Rate Loading Conditions, J. Mater. Proc. Tech., 71:224-234.

Lee, E. H., and Shaffer, B. W., 1951, "The Theory of Plasticity Applied to a Problem of Machining," Transactions of the ASME, Journal of Applied Mechanics, Vol. 73, pp. 404-413.

Lei, S., Yung, C.S., and Incropera, F.P., (1997), "Material Constitutive Modeling under High Strain Rates and Temperatures through Orthogonal Machining Tests", ASME-MED Vol 6-2 Manufact. Sci. Techn., 2 pp. 91-98.

Mallock, A., 1882, "The Action of Cutting Tools," Proc. Soc., Vol. 33, p.127

Mason, C.R.; Worswick, M.J.; Gallagher, P.J (1997) "Adiabatic shear in Remco Iron and quenched and tempered 4340 steel", Journal De Physique. IV : Proc. of the 1997 5th Int. Cong. on Mech. and Phys. Behavior of Matls. under Dynamic Loading, v 7 n 3 Aug p 827-832.

Mason, C., and Worswick, M.J., "Adiabatic Shear in Annealed and Shock Hardened Iron and in Quenched and Tempered 4340 Steel", Accepted for Publication in Int. J. Fract. (2000).

Marusich, T. D., Ortiz, M., 1994, Finite Element Simulation of High-Speed Machining, ASME Symposium on Mechanics in Materials Processing and Manufacturing, AMD-Vol. 194, 137-149.

Merchant, M, 1945, "Mechanics of Metal Cutting Process. I. Orthogonal Cutting and a Type 2 Chip," Journal of Applied Physics, Vol. 16, No. 5, pp. 267-275.

Meyers, M. A., 1994, "Dynamic Behavior of Materials," John Wiley and Sons, Inc.

Moufki, A., Molinari, A., Dudzinski, D., 1999, " Modelling of Orthogonal Cutting" 1st French and German Conf. On High Speed Machining, pp. 8-28.

Nakayama, K., 1974, "The Formation of Saw-toothed Chip in Metal Cutting," Proceedings of International Conference on Production Engineering, Tokyo, pp. 572-577.

Nakayama, K., Arai, M. and Kanda, T, 1988, "Machining Characteristic of Hard Materials," Annals of the CIRP, Vol. 37, pp. 89-92.

Nakayama, K., and Arai, M., 1992, "Comprehensive Chip Form Classification Based on the Cutting Mechanism," Annals of the CIRP, Vol. 71, pp. 71-74.

Oxley, P.L.B., Hastings, W.F., 1977, "Predicting the Strain Rate in the Zone of Intense Shear on which the Chip is Formed in Machining from the Dynamic Flow Stress Properties of the Work Material and Cutting Conditions", Proc. of the Royal Soc. London, Vol. A356, pp. 395-410.

Oxley, P.L.B., 1989, *Mechanics of Machining – An Analytical Approach to Assesing Machinability,* Ellis Hoorwod Limited.

Palmer, W. B., and Oxley, P. L. B., 1959, "Mechanics of Orthogonal Machining," Proc. Instn. Mech. Engrs., Vol. 173, No. 24, pp. 623-638.

Palmer, W. B., 1967, "Plastic Deformation When Cutting Into an Inclined Plane," Jornal of Mechanical Engineering Science, Vol. 9, No. 1, pp. 1-9.

Piispanen, V., 1937, Eripanes Teknillisesla Aikakauslehdehsla, Vol. 27, p315.

Poulachon, G., Moisan, A.L., 2000, Hard Turning: Chip Formation Mechanisms and Metallurgical Aspects, Trans. ASME, 122, pp. 406-412.

Poulachon, G., A. Moisan and I.S. Jawahir, 2001, "On Modeling the Influence of Thermo-mechanical Behavior on Chip Formation During Hard Turning of 100Cr6 Bearing Steel", Annals of the CIRP, Vol. 50(1), pp. 31-36.

Rai, G., 1993, "The Metallurgy of CBN and its Wear in High Speed Machining of Ferrous Materials", Machining of Advanced Materials, Proceeding of International Conference on Machining of Advanced Materials, Gaithersburg, MD, July, pp. 501-514.

Recht, R. F., 1964, "Catastrophic Thermoplastic Shear," Journal of Applied Mechanics, Transactions of the ASME, Vol. 86, pp. 189-193.

Ren, H., Altinas, Y., 2000, "Mechanics of Machining with Chamfered Tools", Tans ASME, J. Manuf. Sci. Eng., Vol. 122, pp. 650-659.

Saunders, I., and Nutting, J., (1984), "Deformation of Metals to High Strains Using Combination of Torsion and Compression", Metal Science, V18, n12, pp. 571-575.

Semiatin, S. L., and Rao, S. B., 1983, "Shear Localization During Metal Cutting," Materials Science and Engineering, Vol. 61, pp. 185-192.

Shamoto, E., Altintas, Y., Armarego, E.J., 1999, "Prediction of Shear Angle in Oblique Cutting with Maximum Shear Stress and Minimum Energy Principles", J. Manuf. Sci. Tech., Vol. 121, pp 399-407.

Shaw, M.C. (1984) "*Metal Cutting Principles*" Clarendon Press, Oxford.

Shaw, M. C., and Vyas, A., 1993, "Chip Formation in the Machining of Hardened Steel," Annals of the CIRP, Vol. 42, pp. 29-33.

Shaw, M. C., 1995, "Precision Finishing," Annals of the CIRP, Vol.44, pp. 343-348.

Shaw, M.C., Vyas, A., 1998, The Mechanism of Chip Formation when Hard Turning Steel, Annals of the CIRP, 47/1:77-82.

Schultz, H. and Hock, St., 1995, "High-Speed Milling of Dies and Molds - Cutting Conditions and Technology", Annals of CIRP, Vol. 44/1, pp .

Sowerby, R. And Chandrasekaran, N., 1989, "A Proposal for the Onset of Chip Segmentation in Machining," Materials Science and Engineering, A. , Vol. 119, pp. 219-229.

Spence, A.D., Altintas, Y., 1994, "A Solid Modeller Based Milling Process Simulation and Planning System", ASME J. Eng. Ind., Vol 116, pp.61-69.

Staker, M.R., (1981), "The Relation between adiabatic Shear Instability Strain and Material Properties", Acta Metallurgica, 29, pp. 683-689.

Subramanian, S.V., Gao, J., Gekonde, H.O., 1999, " Metallurgical Aspects of Chip Morhpology Control in Machining of Steel", 41st MWSP Confr. Proc. ISS, Vol, 37, pp.367-374.

Sutherland, J.W., DeVor, R.E., 1986, "An Improved Method for Cutting Force and Surface Error Prediction in Flexible End Milling Systems", Trans. ASME J. Eng. Ind., V. 108, pp. 269-279.

Tlusty, J., MacNeil, p, 1975, "Dynamics of Cutting Forces in End Milling", Annals of the CIRP, Vol. 24, pp. 21-25.

van Luttervelt, C.A., T.H.C. Childs, I.S. Jawahir, F. Klocke and K. Venuvinod Patri, 1998, "Present Situation and Future Trends in Modeling of Machining Operations", Annals of the CIRP, Vol. 47(2), pp. 587-626.

Von Tukovich, B.F., Calvo, S., 1968, "Some Applications of Physical Metallurgy in Metal Cutting", Int. MTDR Proceeding, pp.1051-1071.

Von Turkovich, B.F., 1970, "Shear Stress in Metal Cutting", ASME J. Eng. Ind., Vol Feb., pp151-157.

Vyas, A., Shaw, M.C., 1999, Mechanics of Saw-Tooth Chip Formation in Metal Cutting, ASME Journal of Manufacturing Science and Engineering, 121:163-172.

Wang, J.Y., Liu, C.R., 1999, The Effect of Tool Flank Wear on the Heat Transfer, Thermal Damage and Cutting Mechanics in Finish Hard Turning, Annals of the CIRP, 48/1:53-58.

Wright, P.K., 1982, "Predicting the Shear Plane Angle in Machining from Work Material Strain Hardening Characteristics", Trans ASME, J. Eng. Ind., Vol. 114, pp. 285-292.

Yang, M.Y., Park, H., 1991, "The Prediction of Cutting Force in Ball Milling", Int. J. Mach. Tools Manuf., V.31, pp. 45-54.

Yucesan, G., Altintas, Y., 1994, "Prediction of Ball End Milling Forces", Trans. ASME J. Eng. Ind., V. 118, pp. 95-105.

Zener, C., Hollomon, J.H., 1944, "Effect of Strain Rate upon Plastic Flow of Steel", J. Appl. Phys., Vol 15, pp. 22-32.

Zerilli, F.J., and Armstrong, R.W., (1987), "Dislocation Mechanics Based Constitutive Relations for Material Dynamics Calculations" J. Appl. Phys., 61, pp. 1816-1825.

Zhang, H.T., Liu, P.D., Hu, R.S., 1991, "A Three Zone Model and Solution of Shear Angle in Orthogonal Machining", Wear, Vol. 143, pp.29-43.